PROTECTIVE EFFECTS OF SPHINGOMYELIN AGAINST UV PHOTODAMAGE IN HUMAN KERATINOCYTES

A Thesis

presented to

the Faculty of California Polytechnic State University,

San Luis Obispo

In Partial Fulfillment

of the Requirements for the Degree

Master of Science in Biomedical Engineering

by

Kathleen Yague De Guzman

December 2013

COMMITTEE MEMBERSHIP

TITLE:	Protective Effects of Sphingomyelin against UV Photodamage in Human Keratinocytes
AUTHOR:	Kathleen Yague De Guzman
DATE SUBMITTED:	December 2013
COMMITTEE CHAIR:	Lily Hsu Laiho, Ph.D. Associate Professor of Biomedical Engineering
COMMITTEE MEMBER:	Kristen O'Halloran Cardinal, Ph.D. Associate Professor of Biomedical Engineering
COMMITTEE MEMBER:	Rafael Jimenez-Flores, Ph.D. Professor of Dairy Science

ABSTRACT

Protective Effects of Sphingomyelin against UV Photodamage in Human Keratinocytes

Kathleen Yague De Guzman

Ultraviolet (UV) radiation has been demonstrated in numerous studies to be a major risk factor for non-melanoma skin cancer development. Despite the emergence of current UV-preventative strategies, such as sunscreens and skin-protective clothing, the incidence of non-melanoma skin cancer has continued to rise. This has encouraged investigations on alternative methods for UV prevention. In particular, bovine milk sphingomyelin has been studied for its potential in protecting human skin against UV photodamage. While the previous studies have suggested that sphingomyelin exhibits UV-protective properties in a human skin equivalent model, the exact mechanisms behind sphingomyelin's photoprotective effects are yet unknown.

This thesis aims to further investigate the UV-protective effects of sphingomyelin in normal human epidermal keratinocytes, using nuclear p21 expression as a marker for UV photodamage. Keratinocytes were incubated for 24 hours in a 0.1% sphingomyelin solution and then exposed to 40mJ/cm^2 of 302nm UV radiation. After 24 hours of post-UV incubation, nuclear p21 expression was evaluated using immunofluorescence. Confocal images were analyzed for their mean nuclear p21 fluorescence intensity measured in grayscale (0-255). Keratinocytes treated with sphingomyelin showed approximately a 50% decrease in UV-induced mean nuclear p21 intensity compared to keratinocytes with no sphingomyelin treatment (via Tukey's test; $p<0.05$). Furthermore, sphingomyelin in keratinocytes not treated with UV radiation caused roughly a 60% increase in mean nuclear p21 intensity (via Tukey's test; $p<0.05$). These findings suggest

that 0.1% bovine milk sphingomyelin protects human keratinocytes from UV photodamage in a p21-dependent manner, but also causes potential toxicity involving p21 upregulation.

Keywords: Keratinocytes, p21, UV radiation, sphingomyelin, skin cancer

ACKNOWLEDGMENTS

I wish to express my deepest sense of gratitude to my thesis advisor, Dr. Lily Laiho, whose humble intelligence and keen understanding has always welcomed my academic- and career-related queries. This thesis would not have been possible without your subtle confidence in me, which has motivated me in every step of the process. You truly have been a major inspiration to me throughout my graduate education experience. I would also like to thank Dr. Kristen Cardinal and Dr. Rafael Jimenez-Flores for so willingly being on my thesis committee and providing me with enthusiastic support.

This thesis has greatly benefited from my numerous colleagues who have graciously contributed their time in helping me with my research. I would especially like to thank Carl Dargitz, for teaching me everything I needed to know about cell culturing; Bradley Schab, for writing the valuable and time-saving MATLAB code used for image analysis; and Jeff Palmer, Lan Anh Nguyen, Erin Fong, Kristina Bishart, and Karissa Cardenas, for being such helpful and reliable labmates.

Last but not least, I would like to thank my mom and late dad, for their loving counsel and continuous encouragement all throughout this thesis process. Mom, you have taught me what it truly means to be a hard worker, which has proven to me to be of great importance in dealing with countless hours of research. I am so grateful to have you as my mom. Dad, your funny sense of humor and carefree attitude always rescued my sanity whenever I fell victim to thesis-induced stress. Moreover, you taught me a valuable lesson that I believe has helped me the most in regards to completing this thesis; that is, to fight to the very end and persevere even when your efforts seem fruitless. Thank you.

TABLE OF CONTENTS

LIST OF TABLES

Page

LIST OF FIGURES

Page

Chapter 1: Introduction

Over the past two decades, there has been a dramatic increase in the incidence of non-melanoma skin cancer (NMSC). In the U.S. alone, it was estimated that approximately 1 million cases of NMSC were diagnosed in 1994 (Miller et al. 1994). In 2006, an estimated 3.5 million cases of NMSC were diagnosed, representing over a 300% increase (Rogers et al. 2006). Similarly large increases in NMSC incidence have also been observed throughout the world. For example, in Australia, the total number of NMSC treatments increased by 86%, from 412,493 in 1997 to 767,347 in 2010, and is estimated to increase to 938,991 by 2015 (Fransen et al. 2012). In addition, the worldwide incidence of NMSC per year is expected to continue to increase by about 3-8% in the coming years (Surdu et al. 2013). This may be attributable to lifestyle changes involving more exposure to ultraviolet (UV) radiation (e.g. increased outdoor activity or use of tanning beds) and a compounding history of excessive UV exposure that comes with aging. This increase may also be attributable to immunosuppression caused by a widespread use of cholesterol-lowering statin drugs and old age (Mascitelli et al. 2010).

Available treatments for NMSC include surgically removing the ulcer, or destroying the ulcer by an electric current, freezing temperatures, radiation therapy, or topical medications (American Cancer Society, 2013). These treatment are both highly effective at curing the disease, and more notably, relatively inexpensive. Nevertheless, in the U.S., NMSC treatments accounted for about $2.9 billion in average annual expenditures on cancer conditions among adults from 2005 to 2008 (Machlin et al. 2011). This corresponded with an average of about 3.72 million treatments each year, a significantly larger number than that of treatments for other common cancers such as

breast, prostate, colon, and lung (Machlin et al. 2011). As the annual NMSC prevalence increases worldwide, the annual expenditures on NMSC treatments is also expected to increase. As depicted in Figure 1.1, the number of treatment procedures for NMSC steadily increased from 1999 to 2008; and this increase is expected to continue (Donaldson et al. 2011). Thus, it is generally accepted by researchers that the world is in the midst of a skin cancer crisis.

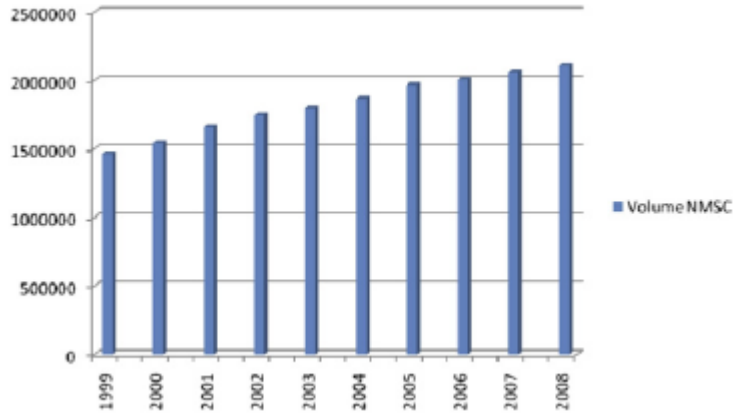

Figure 1.1 Total volume of treatment procedures for NMSC per 5% sample Medicare Data Set (Donaldson, 2011).

To address this issue, more and more studies are being performed to investigate and develop new preventative measures that are more effective than those currently available. Current preventative measures for NMSC protect the skin against UV photodamage through the application of sunscreen, wearing clothes and hats that block the skin from sun exposure, and staying in shady areas and out of direct sunlight. While all of these methods have yet to prove adequate for the reversal of the NMSC epidemic, there has been considerable interest in identifying compounds that will inhibit or reverse the biochemical changes required for skin cancers to develop, either by pharmacologic intervention or by dietary manipulation (Camp et al. 2011). Recent studies show that dietary protection may be provided by omega-3 fatty acids (Black et al. 2006),

resveratrol, and green tea polyphenols (Afaq, 2010). Studies involving the addition of chemopreventative agents to topical sunscreens have also shown promising results, most notably those investigating the topical application of T4N5 liposomal lotion (Giacomoni, 2007). This lotion contains the bacterial DNA repair enzyme, T4 endonuclease V, encapsulated within liposomes for delivery into skin cells, which has been shown to significantly increase repair of DNA damage caused by UV radiation in phase 2 clinical trials (Giacomoni, 2007). Much of the UV exposure over a lifetime occurs when the skin is not protected; thus, the use of dietary factors with sun-protecting properties, as well as topical chemopreventative agents, might have a substantial beneficial effect.

In recent studies performed by the team of Dr. Lily Laiho at California Polytechnic State University, San Luis Obispo, bovine milk sphingomyelin liposomes were investigated for their potential protective effects against UV photodamage in human skin tissue equivalents (Russell et al. 2010). Skin equivalent models featuring the epidermis (epidermal tissue constructs) were used to analyze UV photodamage with and without sphingomyelin treatment, which involved adding exogenous sphingomyelin to the tissue culture medium 24 hours prior to UV irradiation. Different methods for analyzing the protective effects of sphingomyelin in the tissue constructs were used (e.g. histology, Western blot, immunofluorescence, etc.) to detect for markers of UV photodamage, which included DNA fragmentation, changes in tissue morphology, and p21 protein expression. While these studies have suggested that bovine milk sphingomyelin acts upon human epidermal tissue constructs in a UV protective manner, additional studies are necessary to fully understand the cellular mechanisms taking place and to provide sufficient evidence to confirm the previously found results.

Therefore, the main goals of this thesis are to further investigate the protective effects of bovine milk sphingomyelin against UV photodamage in a human skin model system and to provide statistically significant evidence that sphingomyelin protects against UV-induced DNA damage, by quantitatively assessing the expression of nuclear p21 protein using immunofluorescence. The p21 protein will be used to indicate cell cycle arrest and UV-induced DNA damage following UV irradiation of the human skin model system, since p21 is known to be a major cell cycle inhibitor in response to DNA damage (Blundell, 2006). Normal human epidermal keratinocyte culture will be used as the human skin model system in this thesis, since it would provide a simpler and more predictable model system compared to the epidermal tissue constructs used in the previous studies. Epidermal keratinocyte cultures are commonly used in research as living model systems to help define cellular and molecular mechanisms of the skin (Jensen et al. 1991). Additionally, keratinocyte culture offers a means to study cellular responses under more controlled conditions compared to epidermal tissue constructs, as there are less variable components involved. As such, normal human epidermal keratinocytes will be used in this thesis to investigate the effects of sphingomyelin treatment on nuclear p21 expression in UV-irradiated keratinocytes, to give insight on the cellular mechanisms behind sphingomyelin's potential photoprotective effects.

Chapter 2: Background

2.1 Structure and Function of the Epidermis

The integument, or skin, is the largest organ of the human body, accounting for approximately 16% of an average adult's body weight, with a surface area of 1.8m^2 (Bensouilah et al. 2006). It is composed of two distinct layers known as the epidermis and dermis, which provide the body with a physical and chemical barrier against the outside environment. While both of these layers function together in protecting the inside of the body from outside threats, such as microorganisms, mechanical insults, toxic chemicals, and electromagnetic radiation, the epidermis is the layer mainly responsible for the skin's barrier function. In addition to its protective functions, the epidermis is also responsible for the absorption and secretion of water, electrolytes, and other substances (e.g. topical drugs).

The epidermis is a constantly replenished epithelium that forms the outermost layer of skin. It varies in thickness from 0.05mm on the eyelids to 0.8-1.5mm on the soles of the feet and palms of the hand (Bensouilah, 2006). Specialized cells called keratinocytes make up 95% of the total cells in the epidermis (Price et al. 2008). These cells are responsible for the epidermis constantly replenishing itself, as they continuously move from the deepest layer of the epidermis towards the shedding outer surface of dead keratinocyte flakes. The life of a keratinocyte, from birth to its loss from the body as a skin flake, is about one month (Lodish et al. 2013).

The four layers that make up the epidermis (from the deepest layer upwards) are the stratum basale, stratum spinosum, stratum granulosum, and stratum corneum (Bensouilah et al. 2006) (see Figure 2.1). A fifth layer is found in the epidermis of the

soles and palms, called the stratum lucidum, which is a thin layer of translucent cells located between the stratum granulosum and the stratum corneum (Bensouilah et al. 2006).

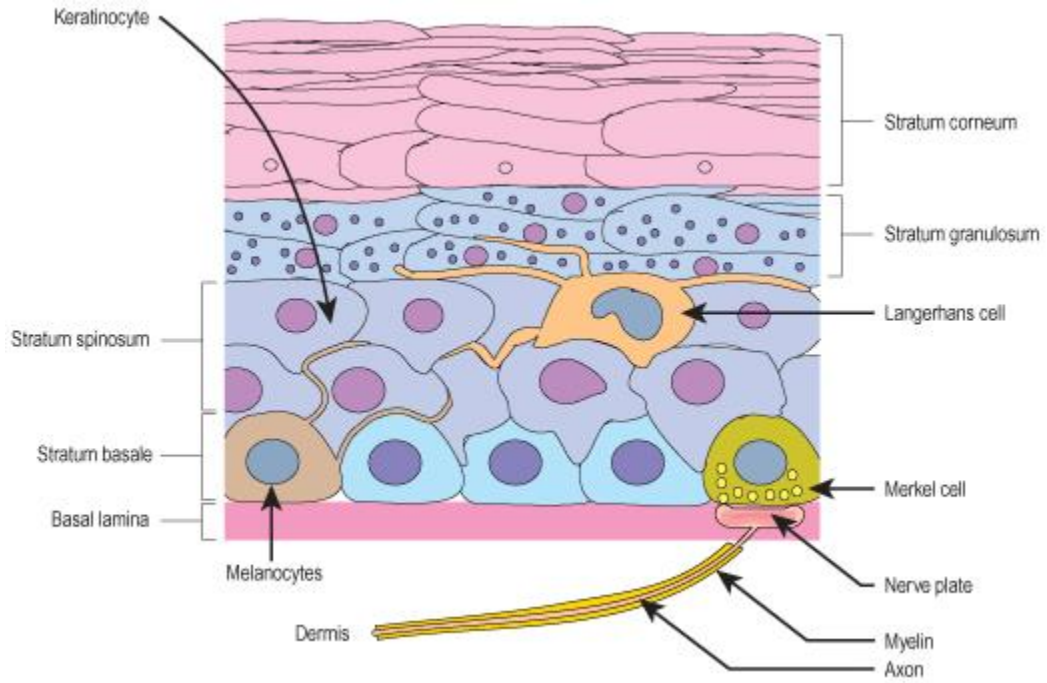

Figure 2.1 Structure of the human epidermis (Standring, 2005).

The stratum basale, which is one cell layer thick, consists of cuboidal epithelial cells attached to the basement membrane, which separates the epidermis from the dermis (Baroni et al. 2012). It is mainly composed of dividing and non-dividing keratinocytes (Baroni et al. 2012). Dividing keratinocytes are only found in the stratum basale, and can either be stem cells or transient amplifying cells (Bianco et al. 2008). Keratinocyte stem cells give rise to transient amplifying cells, or cells that undergo rapid cell division with a limited number of divisions before terminal differentiation (Bianco et al. 2008). Once a transient amplifying keratinocyte becomes committed to terminal differentiation and stops dividing, it begins the maturation process of keratinization, moving upward towards the stratum corneum and sequentially obtaining the phenotypes characteristic of the

different epidermal layers (Baroni et al. 2012). Other cell types present in the stratum basale are Merkel cells, which are involved in touch sensation, melanocytes, which produce the pigment melanin for UV protection, and dendritic Langerhans cells, which aid in the skin's immune response against foreign antigens (Baroni et al. 2012).

Above the stratum basale is the stratum spinosum. This layer is several cell layers thick and is comprised of keratinocytes, melanin granules, and numerous Langerhans cells (Baroni et al 2012). The keratinocytes in this layer are terminally differentiated, meaning they can no longer divide (Baroni et al 2012). Instead, they begin to produce abundant intermediate filament proteins called keratins, a process known as keratinization (Baroni et al 2012). These keratin filaments are located in the cell's interior, specifically the cytoplasm, and provide structural support. Apart from keratinization, the keratinocytes in this layer also begin to produce lamellar bodies (Proksch et al. 2008). Lamellar bodies are secretory vesicles which are enriched in polar lipids, glycosphingolipids, free sterols, phospholipids, and catabolic enzymes as well as other proteins (Proksch et al. 2008). The lipids initially sequestered within lamellar bodies are later secreted into the extracellular space between the stratum granulosum and stratum corneum to provide a barrier function against water loss (Proksch et al. 2008).

In the stratum granulosum, keratinocytes begin to lose their nuclei and organelles, produce keratohyalin granules, and have a moderately flattened shape (Proksch et al. 2008). They also continue to accumulate keratin and lamellar bodies within their cytoplasm. As the nuclei and organelles gradually deteriorate and the cells die, the keratohyalin granules increase in size and number (Costin et al. 2007). The keratohyalin granules consist mainly of the epidermal protein profilaggrin (Costin et al. 2007).

Both the keratohyalin granules and the lamellar bodies of the stratum granulosum contribute to the densely-packed, protective barrier of the stratum corneum (Baroni et al. 2012). In this layer, profilaggrin is used in a process that condenses the keratinocyte cytoskeleton to form flattened cells, called a corneocytes (Sandilands et al. 2009). Corneocytes are held together by the lipid secretions of lamellar bodies (Baroni et al. 2012). Eventually, however, clusters of corneocytes are shed as flakes from the skin's surface through the degradation of protein anchoring junctions and the lipid matrix holding corneocytes together (Baroni et al. 2012).

2.2 Non-Melanoma Skin Cancer (NMSC)

2.2.1 Types and Diagnoses

There are two main types of NMSC: basal cell carcinoma (BCC) and squamous cell carcinoma (SCC). Like any form of cancer, these diseases begin when normal cells begin to grow and proliferate uncontrollably, forming a tumor that is capable of spreading to other parts of the body. In BCC, the keratinocytes in the basal layer of the epidermis become cancerous. While BCC accounts for 75% of NMSC cases, it is a slow-growing, highly treatable tumor with a metastatic rate of <0.1% (Samarasinghe et al. 2012). In SCC, the keratinocytes that make up most of the epidermis (squamous cells) become cancerous. Although SCC is less common, accounting for approximately 20% of NMSC cases, it is more likely to metastasize than BCC, having a metastatic rate of 0.3-3.7% (Samarasinghe, 2012).

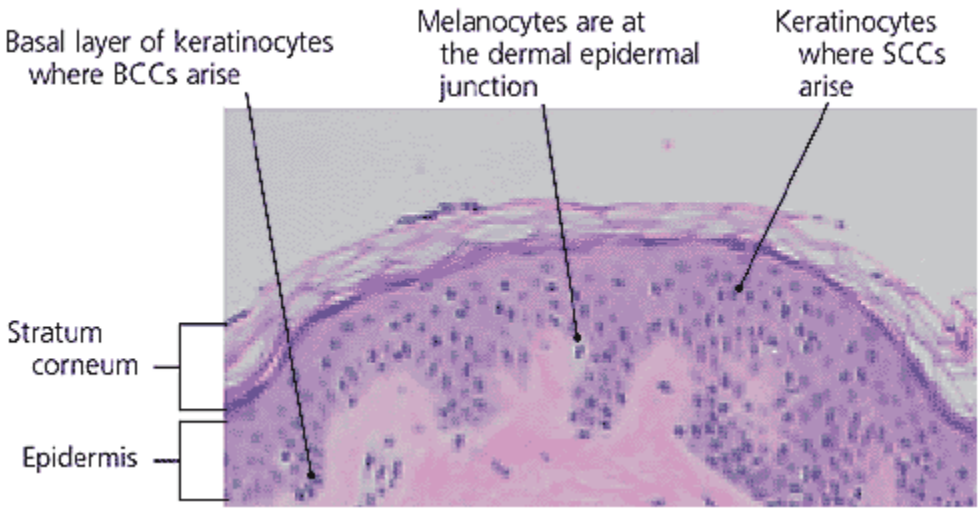

Figure 2.2 Micrograph of the epidermis in which BCCs and SCCs originate (Stulberg et al. 2004).

NMSC usually appears as a growth on the outer surface of the skin that changes in color and morphology (Stulberg, 2004). These growths mainly occur in sun-exposed areas, such as the head, neck, and arms (Stulberg, 2004). During clinical evaluation, a physician may diagnose the type of NMSC based on known distinguishing characteristics (see Figure 2.3). BCC presents itself as a waxy, pearly bump, often with a shallow depression at its center surround by a raised pale border; while SCC takes the form of a crusty, wart-like growth, often with an open sore at its center (Stulberg, 2004). If there are any doubts as to the malignancy and cell type of a skin growth, a physician will often take a biopsy to send to a lab for a more accurate diagnosis.

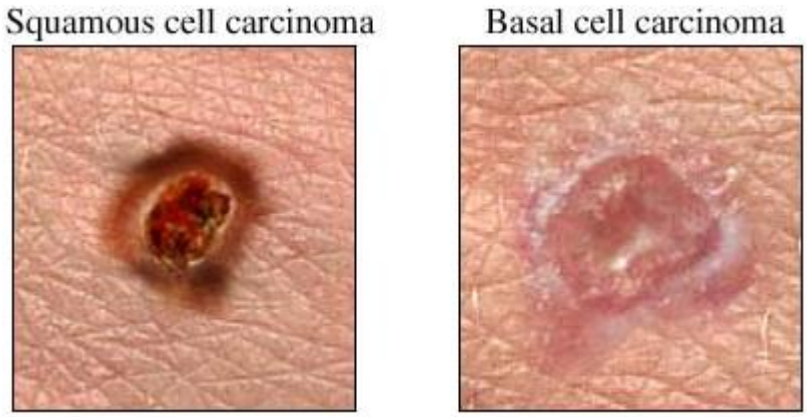

Figure 2.3 SCC and BCC showing common identifying characteristics (Duff, 2011).

2.2.2 UV Radiation

While there are manmade sources of UV radiation used to irradiate skin for various reasons (e.g. tanning booths), the primary source of UV radiation comes from the sun. Of the radiant energy emitted from the sun, approximately 50% lies in the infrared region, 40% in the visible region, and 10% in the UV region (Fu, 2003). Although solar radiation emissions entering the atmosphere only consist of about 10% in the UV region, UV radiation is the main risk factor for developing NMSC due to its higher intrinsic energy.

Biological effects of UV radiation vary enormously with wavelength (Diffey, 2002). Consequently, the UV spectrum is subdivided into three wavelength regions: UVA (400-320nm), UVB (320-290nm), and UVC (290-200nm). Almost all of UVC and the majority of UVB emitted by the sun are absorbed by the earth's ozone layer (Diffey, 2002). This results in approximately 95% UVA entering the earth's atmosphere, while only 5% is UVB (Diffey, 2002). Although both UVA and UVB radiation function as initiators and promoters in carcinogenesis, it has been demonstrated in animal models that UVB is more effective at inducing skin cancer than UVA (Rass et al. 2008). This is

thought to be due to UVB being mainly absorbed in the epidermis, while UVA is mainly absorbed in the dermis, as shown in Figure 2.4. Also, the shorter wavelengths of UVB have been found to more significantly affect the major processes of biological organisms (e.g. metabolism, growth, proliferation, etc.) than the longer wavelengths of UVA (Diffey, 2002).

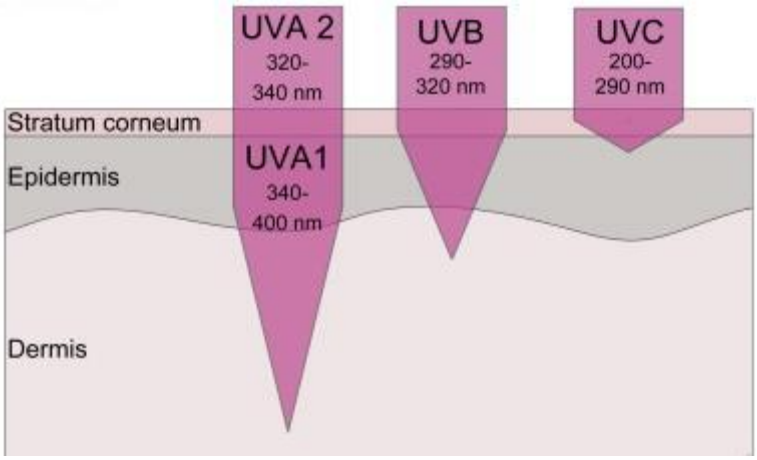

Figure 2.4 Skin penetration of UVA, UVB, and UVC radiation (Maverakis et al. 2010).

UVB radiation is known to cause direct DNA damage. Upon a DNA strand's absorption of a UVB photon, the photon's energy is used up in the formation of covalent bonds between two adjacent pyrimidine nucleotide bases (cytosine or thymine), resulting in a pyrimidine dimer (Rass et al. 2008). This alters the DNA's structure and may lead to mutation if the damage is left unrepaired. The two most common photoproducts of UVB-induced DNA damage are cyclobutane pyrimidine dimers (CPDs) and 6-4 photoproducts (Rass et al. 2008), shown in Figure 2.5. Both CPDs and 6-4 photoproducts can give rise to C→T or CC→TT transitions, which are the main genetic markers for UV-induced mutagenesis (Melnikova et al. 2005). These transitions are essentially DNA mutations in which one or both cytosine bases of the dimer are incorrectly replaced with thymine

during DNA replication (Melnikova et al. 2005). If such mutations accumulate in the genetic sequence of a tumor suppressor gene, such as p53, the activity of the corresponding tumor suppressor may be altered in such a way that favors cell tumorigenesis, ultimately leading to NMSC (Melnikova et al. 2005).

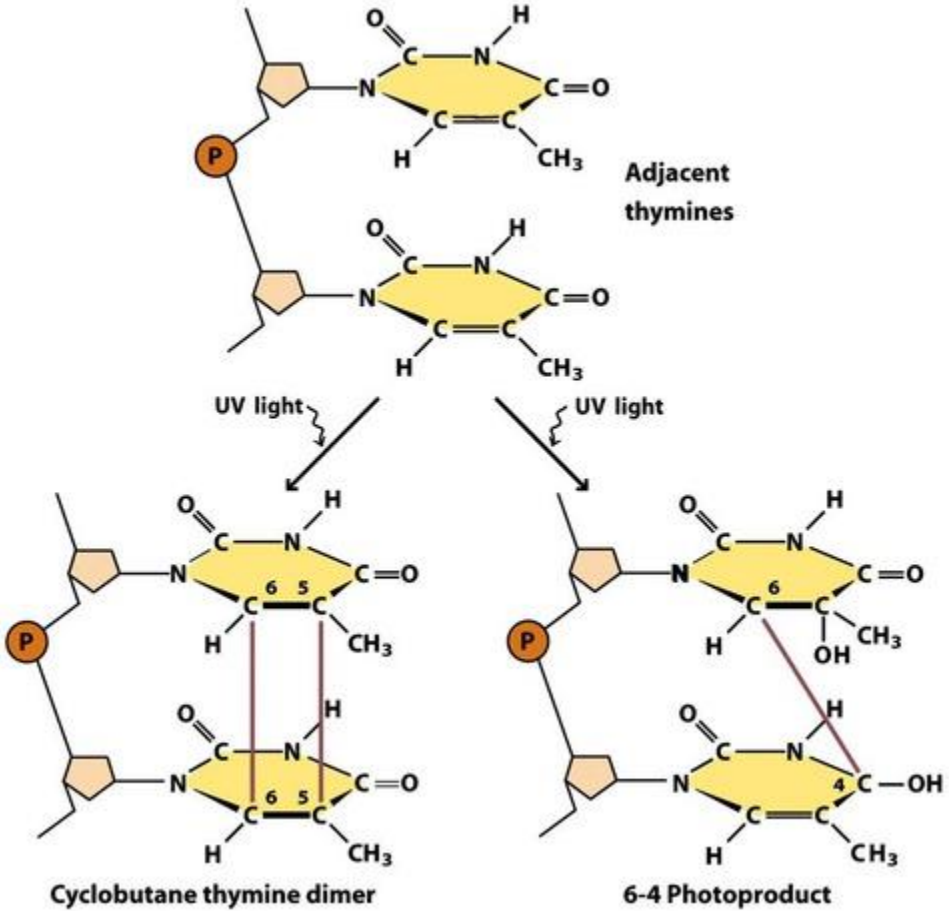

Figure 2.5 Common photoproducts of UVB-induced DNA damage (Nelson et al. 2008).

While UVB is mainly associated with direct DNA damage, UVA is mainly associated with indirect DNA damage since it is predominantly absorbed by chromophores other than DNA (Rass, 2008). When absorbed by chromophores of the skin, UVA is known to produce different types of reactive oxygen species (ROS), such as superoxide and hydrogen peroxide, depending on the chromophore (Rass, 2008). ROS

produced in the skin can in turn, directly induce DNA damage, including single strand breaks, oxidative base damage, and DNA-to-protein crosslinks, all of which may lead to NMSC-related DNA mutations.

In addition to DNA damage, UV radiation on the epidermis can also cause an inflammatory response and post-inflammatory immunosuppression. Studies have shown that UV radiation induces an increase in inflammatory cytokines, such as IL-1, TNFα, IL-6, and COX-2, in human keratinocytes (Ravi et al. 2013). The increase in these molecules leads to the migration of immune cells (e.g. macrophages and neutrophils) into the epidermis and an increase in inflammatory cytokine levels via a positive feedback loop (Ravi et al. 2013). Such cytokines create an inflammatory environment that supports the progression of carcinogenic cells (Ravi et al. 2013). This may partly be due to inflammatory cells producing ROS, thus increasing oxidative damage to DNA and the risk of carcinogenic mutations (Svobodova et al. 2006). UV-induced immunosuppression is known to be caused by several factors, including the increase in macrophage secretion of IL-10, which results from a UV-induced inflammatory response (Maverakis, 2010). IL-10 is an anti-inflammatory cytokine capable of inhibiting the surface expression MHC class II and costimulatory molecules that are important for T cell activation and antigen recognition, thus hindering the immune response (Maverakis, 2010). Apoptosis of Langerhans cells and T cells due to photodamaged DNA is also known to play a role in UV-induced immunosuppression (Maverakis, 2010). UV-induced immunosuppression increases NMSC carcinogenesis, since the body's surveillance for tumor cells is decreased.

2.2.3 Pathogenesis

It takes years to decades of normal daily sun exposure for NMSC to occur. Accordingly, NMSC has been found to be more common in people older than 50 years (Balk, 2011). Like all types of cancer, NMSC develops in a step-wise fashion that is commonly divided into three stages: initiation, promotion, and progression (see Figure 2.6). Initiation, a rapid and irreversible step, occurs when a normal keratinocyte experiences mutagenic DNA damage from UV radiation, and acquires a slight change in phenotype that enables it to form a tumor (Cataisson et al. 2012). Cellular changes required for initiation include enhanced proliferation and migration, inhibited terminal differentiation, and reduced expression of normal keratinocyte differentiation markers (Cataisson et al. 2012).

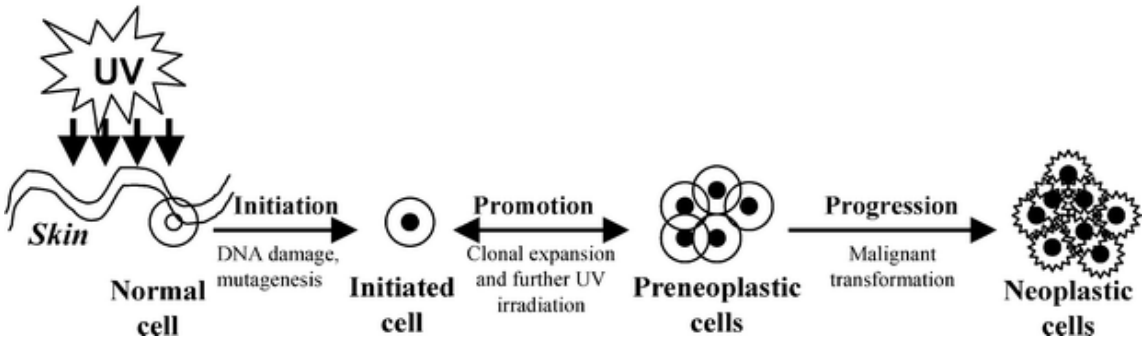

Figure 2.6 Pathogenesis of NMSC (Baliga et al. 2006).

Promotion occurs through the repeated application of substances called tumor promoters to initiated keratinocytes, which causes selective clonal expansion of these cells to produce multiple small benign epithelial tumors, or papillomas (Yuspa, 1994). Mutations that are often associated with promotion are loss-of-function gene mutations in p53, PTCH1, DNA repair genes, ras, and Fas (Yuspa, 1994). These genes all encode proteins that act as tumor suppressors. Promotion in the development of NMSC is known

to be promoter dependent, requiring chronic UV radiation to repeatedly generate DNA damage and mutations (Yuspa, 1994). Progression on the other hand, is generally promoter independent and occurs spontaneously (Yuspa, 1994). This stage of cancer pathogenesis involves repeated cycles of cell selection in order for a specific premalignant cell genotype to dominate and cause clonal outgrowth (Yuspa, 1994). Through a sufficient accumulation of specific oncogenic and tumor suppressor gene mutations in premalignant cells, NMSC transpires. The malignant (or neoplastic) cells of NMSC usually proliferate rapidly, and have the ability to invade nearby tissue and metastasize (Yuspa, 1994).

Besides UV radiation, other factors that may positively influence the pathogenesis of NMSC are a decreased immune response, insufficient antioxidant levels, hereditary factors, oncoviral infections, and inflammation (Yuspa, 1994). An appropriate immune response is needed to defend the body against tumor cells, as well as oncoviral infections. Antioxidants are needed to prevent oxidative damage of ROS. Hereditary factors such as light skin color may increase an individual's susceptibility to NMSC, since light skin lacks an adequate amount of melanin to protect cells against UV-induced DNA damage. Other hereditary factors that positively influence NMSC development include genes that increase one's susceptibility to tumor initiators and promoters. Oncoviral infections can cause the insertion of viral oncogenic genes into one's genome, thus provoking NMSC development. Lastly, inflammation, which may be caused by viral infections and UV radiation, can create an inflammatory environment within the epidermis that supports cancer growth.

2.2.4 Prevention

Currently, there are numerous preventative measures against NMSC. Most of these measures involve protecting the skin from direct UV radiation, the main risk factor for NMSC. For example, individuals can wear protective clothing that block the skin from solar UV rays, seek shady areas during the day when the sun's UV rays are most intense, and avoid using tanning booths and sunlamps. In addition, the application of sunscreen is commonly used to prevent NMSC. Sunscreen, which has been around for more than 70 years (Bissonnette, 2012), is used worldwide as a topical lotion that protects the skin from solar UV radiation. It works by either absorbing or reflecting UV rays, depending on its ingredients. Organic compounds used in sunscreen (e.g. avobenzone, ecamsule, oxybenzone, etc.) work by absorbing UV radiation through their chemical bonds, which eventually break down and release the energy as heat (Bissonnette, 2012). Inorganic compounds used in sunscreen (e.g. titanium dioxide or zinc oxide) work by reflecting and scattering UV radiation away from the skin (Bissonnette, 2012). Although sunscreen can effectively protect the skin from UV radiation, many individuals use it inappropriately. For example, while the FDA recommends that sunscreen be reapplied every 2 hours regardless of its strength (FDA, 2013), it is likely that an individual either forgets to reapply or is unaware of the necessity for reapplication of sunscreen. Also, it is recommended that 1 oz (about a shot glass full) of sunscreen be applied evenly to the skin to obtain the advertised protection; however, studies show that most people apply only half to a quarter of that amount (Skin Cancer Foundation, 2013). Because the incidence of NMSC continues to rise despite the numerous preventative measures currently

available, there is an ongoing search for alternative methods that can better prevent NMSC.

Many natural agents are being studied for their photoprotective properties in skin, such as omega-3 fatty acids (Black, 2006), resveratrol, and green tea polyphenols (Afaq, 2010). A recent clinical trial has shown that dietary omega-3 fatty acids, which are a group of fats found in marine and plant oils, play a chemopreventative role in NMSC development in humans (Pilkington et al. 2013). The study showed that dietary omega-3 fatty acids significantly inhibit UV-induced immunosuppression in human skin, one of the risk factors of NMSC. Resveratrol and green tea polyphenols are currently being studied for their dietary and topical preventive effects against NMSC. Studies on these natural agents in mice have shown that they dramatically enhance UVB-induced apoptosis of pre-malignant epidermal cells, underlining their potential as chemopreventative agents against NMSC (Afaq, 2010). Numerous other natural agents are being studied for their chemopreventative potential against NMSC. However, the mechanisms of most of these agents are not fully understood and additional studies are needed before these agents are deemed safe and effective for clinical use.

2.3 Normal Human Epidermal Keratinocyte Culture

Normal human epidermal keratinocytes are often derived from primary cell cultures, which are isolated directly from the tissue with no passaging, or subculturing (i.e. transferring the cells from one culture vessel to a new one with fresh growth medium) (Stacey, 2005). Once primary cells are passed however, they are more correctly referred to as a finite cell line (Stacey, 2005). Finite cell lines have a limited number of population doublings before the cells undergo senescence (Stacey, 2005). The maximum

passage limit of a cell line is known as the "Hayflick limit," at which the cells cease division and become senescent (Stacey, 2005). It is common for primary cell cultures to be composed of a mixture of cell types. A chemically defined growth medium that favors the desired cell type is often used in combination with several passages to select for the desired cell type and to create a more phenotypically uniform population (Stacey, 2005).

Human keratinocytes are isolated from either adult skin or neonatal foreskin biopsies, using a protease (e.g. trypsin) and a chelating agent (e.g. EDTA) to break apart intercellular anchoring junctions and dissociate cells from the skin (Price et al. 2008). Once cells are extracted from the tissue, they are normally grown in plastic culture flasks and incubated in a physiological environment (e.g. 37°C, humid). Chemically defined keratinocyte medium is used to support, enhance, and select for keratinocyte growth, and to inhibit the growth of other cell types, such as fibroblasts. Because keratinocytes are adherent in nature, they adhere to the two-dimensional bottom surface of the culture flask and form islands that grow outwards horizontally. As islands of keratinocytes grow, daughter cells of those in the center of the island start to stratify and up to 12 cell layers may form (Price, 2008). Under a white light microscope, human keratinocytes appear to have a polygonal form, and are convex (not flat) in elevation. Also, when keratinocytes undergo mitosis, they dissociate from the monolayer and under a white light microscope, appear to have a spherical shape with a distinct white border (see Figure 2.7). The mean cell cycle time for a primary human keratinocyte is 22-24 hours (Price, 2008). The age, sex, and biopsy site of the tissue donor influences the characteristics of a specific primary cell culture (Price, 2008). For example, epidermal keratinocytes isolated from healthy

neonatal foreskins are capable of undergoing between 50-60 population doublings, but this decreases with age (Price, 2008).

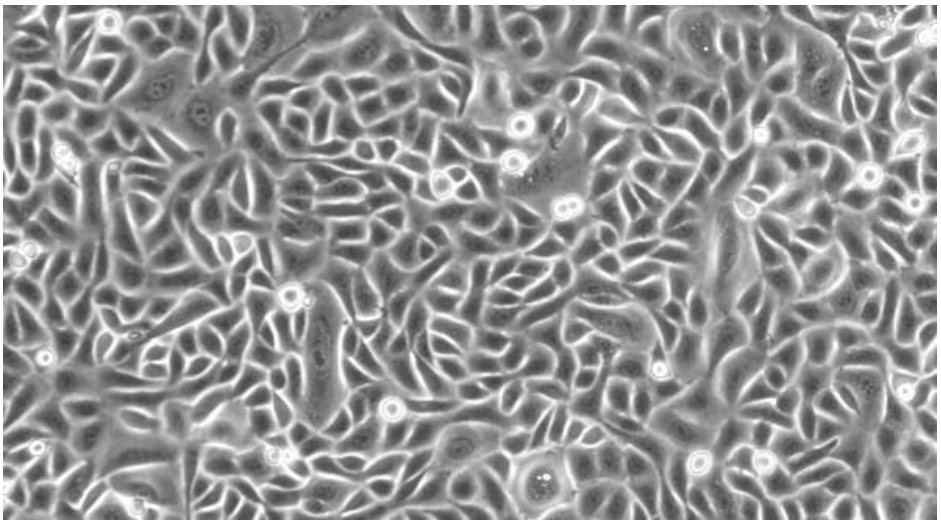

Figure 2.7 Human keratinocyte monolayer at 100x magnification (ScienCell Research Laboratories, 2009).

Normal human epidermal keratinocyte culture is used widely in cellular and molecular biology research, as it provides consistent and reproducible living model systems that have physiological characteristics very similar to the native human epidermis (Stacey, 2005). Furthermore, keratinocytes cultured in monolayer are easy to visually examine under an inverted microscope, and provide a more simple and predictable model system when compared to skin tissue constructs or animal models. Cell culture in general, involves much less materials and procedures for experiments compared to other methods, which allows for cost-effective, straightforward analyses. However, while there are many advantages of normal human epidermal keratinocyte culture, there are also many disadvantages. For example, the cellular characteristics from cell line to cell line can vary depending on the genetics and disease status of the tissue donor, as well as the number of passages the cells have undergone (Stacey, 2005). The

characteristics of cells derived from primary cell cultures change with every passage, since each passage inevitably selects for cells that are the most capable of proliferating in the plastic culture flask. Thus, it is highly crucial that cells from the same cell line and passage are used in any one experiment to obtain reliable results. Another disadvantage of keratinocyte culture is that it requires frequent passaging, with the optimal confluence for passing keratinocytes being 80% (ATCC, 2013). In fact, if keratinocytes are allowed to reach 100% confluence, they begin to terminally differentiate, acquiring an altered phenotype incapable of proliferating (ATCC, 2013). Thus, keratinocyte cultures must be examined under a microscope regularly (every 1-2 days) to avoid terminal differentiation and maintain normal proliferative capacity (ATCC, 2013).

2.4 Human p21 Protein

2.4.1 Overview

Human p21 protein (also called Cip1 or Waf1) is a major suppressor of cell cycle progression, whose expression is controlled by the tumor suppressor protein p53. Upon detection of DNA damage, for example, p53 is upregulated as part of the cellular stress response and in turn transcribes p21. This results in increased levels of p21 within the DNA-damaged cell. Localized in the nucleus, p21 is known to interact with protein complexes called cyclin-cyclin-dependent kinases (cyclin-CDKs) to induce cell cycle arrest in response to various factors (e.g. DNA damage, serum starvation, differentiation, etc.) (Hattinger et al. 2002). In addition, nuclear p21 is known to interact with and regulate proliferating cell nuclear antigen (PCNA), a protein necessary for DNA synthesis and repair (Lee et al. 2009). While p21 is known to interact with numerous

other cellular proteins involved in cell cycle regulation, it is generally accepted that its interactions with cyclin-CDK and PCNA are paramount to its many functions.

The p21 protein is comprised of 164 amino acids with a molecular mass of 21 kDa (Blundell, 2006). In response to cellular stimuli, p21 expression is tightly regulated at transcriptional and post-translational levels through mechanisms involving RNA stabilization, phosphorylation, and ubiquitination (Warfel et al. 2013). The p21 protein is capable of forming various conformations, which may explain its ability to interact with other proteins aside from cyclin-CDK and PCNA (Tillhon et al. 2013), such as calmodulin, GADD45, and c-myc (Rodriguez-Vilarrupla et al. 2002). The binding domains of PCNA, calmodulin, GADD45, and c-myc are all found at the C-terminus of p21 with several overlaps; while the binding domains of nearly all cyclin-CDKs are found at the N-terminus of p21 (see Figure 2.8) (Tillhon et al. 2013). In addition to its numerous overlapping binding domains, p21 also has a nuclear localization signal (NLS) located at the C-terminus. The NLS of p21 is responsible for its nuclear localization following translation in the cytoplasm. Cytoplasmic localization of p21 can also occur if kinases phosphorylate Thr145 and Ser146 residues near the NLS region (Tillhon, 2013); however, many studies have shown that nuclear p21 has a stronger inhibitory effect against cell proliferation compared to cytoplasmic p21 (Rodriguez-Vilarrupla, 2002).

Figure 2.8 Schematic structure of p21 showing the regions responsible for binding cyclins, CDK, and PCNA (Tillhon, 2013).

2.4.2 Interactions with Cyclin-CDKs

The eukaryotic cell cycle is the process through which a cell undergoes growth and division, and is comprised of four sequential phases: G1 (cell growth), S (DNA synthesis), G2 (cell growth), and M (mitotic cell division). When a cell becomes senescent (ceases to divide), it enters a fifth phase called G0. Most terminally differentiated cells and DNA-damaged cells are found in G0; however, they may be stimulated to reenter the cell cycle given the appropriate environmental factors which favor cell division (Lodish, 2013). In order to ensure proper cell division and avoid genetic damage, the cell cycle consists of control mechanisms known as checkpoints. Checkpoints make the initiation of each phase dependent on the proper completion of the previous phase. The G1/S checkpoint, in particular, is the first checkpoint of the cell cycle and occurs at the end of G1 phase. This checkpoint controls the transition of a cell from G1 phase into S phase, ensuring the cell's genome is undamaged and ready to be replicated, and that levels of DNA synthesis proteins are adequate for S phase to properly transpire. The other two major checkpoints of the cell cycle are the G2/M checkpoint, which occurs at the end of G2 phase; and the metaphase checkpoint, which occurs at the metaphase stage in the middle of M phase.

Checkpoints of the cell cycle are controlled by protein kinases called cyclin-dependent kinases (CDKs), which regulate the activities of various proteins (via phosphorylation) needed to pass cell cycle checkpoints (Lodish, 2013). Although CDK levels are constant throughout the cell cycle, CDKs have no kinase activity unless they are associated with a regulatory subunit known as cyclin (Lodish, 2013). The G1/S checkpoint, for example, is controlled by cyclin D-CDK4/6 (G1 cyclin-CDK) and cyclin

E-CDK2 (G1/S cyclin-CDK). Additionally, CDK activity is regulated by inhibitory phosphorylation on specific tyrosine and threonine residues that maintain the cyclin-CDK complex in an inactive state. In particular, the G1/S phase CDK is regulated by inhibitory phosphorylation on tyrosine 15 (Tyr-15) (Lodish, 2013). This inhibitory phosphorylation is removed by Cdc25A, a protein phosphatase activated near the end of G1.

During G1, activity of G1 CDK rises due to growth factor stimulation of G1 cyclin and Cdc25A dephosphorylation of Tyr-15 (Lodish, 2013). In turn, G1 cyclin-CDKs phosphorylate and inactivate the retinoblastoma protein (Rb), which binds to and inhibits a family of transcription factors called E2F transcription factors (E2Fs) (Lodish, 2013). When Rb is inactivated through its phosphorylation, it dissociates from E2F (Lodish, 2013). This then allows E2F to activate genes encoding G1/S phase cyclins, S phase cyclins, and proteins involved in DNA synthesis (Lodish, 2013). Because G1/S phase cyclin gene transcription is stimulated by E2F, G1/S cyclin-CDKs increase in activity and, in a positive feedback loop, further phosphorylate Rb (Lodish, 2013). Cells pass the G1/S checkpoint once levels of G1/S cyclin-CDKs are sufficiently high (Lodish, 2013). A schematic of this pathway is depicted in Figure 2.9.

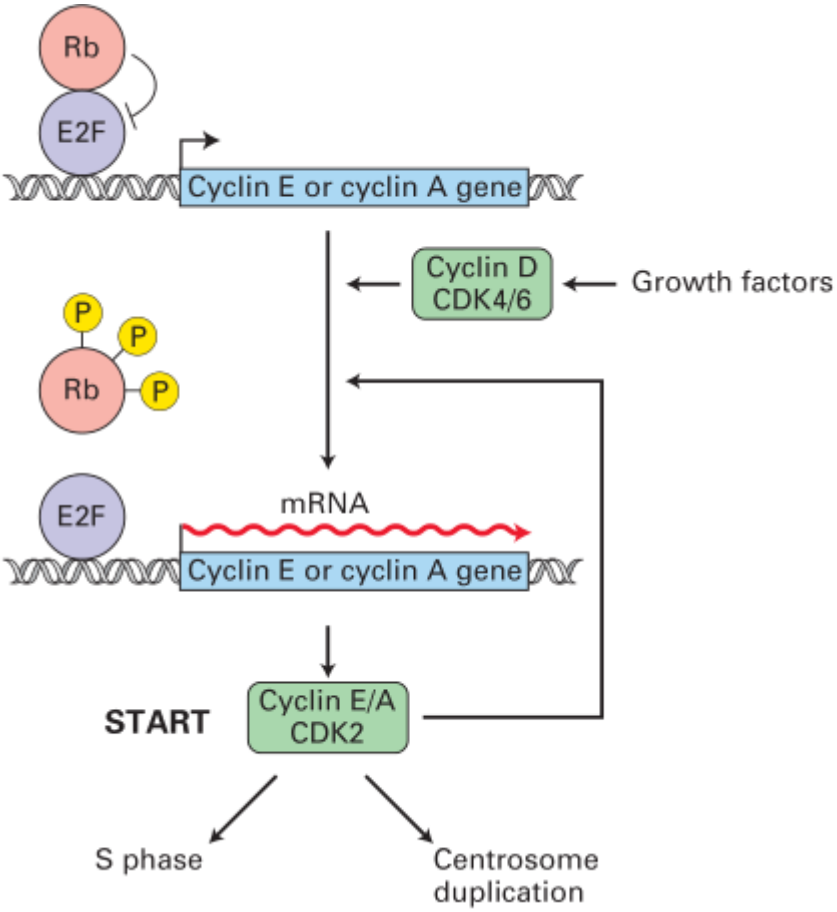

Figure 2.9 G1/S checkpoint regulation (Lodish, 2013).

CDK inhibitors (CKIs) are involved in the regulation of cell cycle checkpoints, since they function by non-covalently binding and inhibiting cyclin-CDKs (Lodish, 2013). The p21 protein is classified as a CKI that can bind to almost all cyclin-CDKs, and is well known for its ability to efficiently inhibit G1 cyclin-CDKs (Lodish, 2013). Overexpression of nuclear p21 inhibits cells from passing the G1/S checkpoint and causes G1 cell cycle arrest (Lodish, 2013). Also, overexpression of nuclear p21 can arrest cells in G2 phase, since p21 is capable of interacting with mitotic CDKs that are needed to pass the G2/M checkpoint; however, this pathway is less common as previous studies have shown p21 to have little mitotic CDK inhibitory capacity (Lopez-Contreras et al. 2012). Aside from its direct inhibition of cyclin-CDKs, p21 can also indirectly inhibit

cyclin-CDKs by competing for the same binding site as Cdc25A on the cyclin-CDK complex (Ball, 1997). Thus, p21 prevents the dephosphorylation and activation of CDKs by Cdc25A protein phosphatase (Ball, 1997). Because p21 efficiently arrests cells in G1, this protein is overexpressed in senescent (G0) cells and is significantly reduced in S phase (Cazzalini et al. 2010).

In contrast to the G1 cyclin-CDK inhibitory function of p21, p21 may also function as an assembly factor for G1 cyclin-CDKs (Ball, 1997). More explicitly, despite its inhibitory function, p21 is conversely capable of promoting the assembly of cyclin D and CDK4/6 into G1 cyclin-CDK, thus promoting downstream events of G1 cyclin-CDK activation (Ball, 1997). This dual function of p21 protein is regulated by the protein's expression level. At low and intermediate concentrations, p21 acts as an assembly factor, while at high concentrations it acts as an inhibitor (Blundell, 2006).

2.4.3 Interactions with PCNA

PCNA is a ring-shaped protein that plays a major role in DNA replication and repair (Haracska et al. 2001). During DNA synthesis, PCNA functions as a sliding clamp along DNA that can bind to DNA polymerase δ (Pol δ) and DNA polymerase ε (Pol ε), the main polymerases involved in DNA replication and nucleotide excision repair (NER) (Haracska et al. 2001). Thus, PCNA functions to increase the stability and processivity of Pol δ and Pol ε along the single DNA template strand. PCNA has also been found to stimulate the activity of DNA polymerase η (Pol η), a translesion synthesis (TLS) polymerase capable of replicating through DNA lesions such as UV-induced cyclobutane pyrimidine dimers (Haracska et al. 2001). If Pol δ and Pol ε are unable to remove a specific DNA lesion, a replication block occurs that can lead to cellular senescence or

cell death (Rastogi et al. 2010). Thus, TLS is needed to bypass or repair these lesions and prevent cell death. While Pol η is generally error prone when dealing with undamaged DNA compared to the main replicative DNA polymerases, it must be closely regulated by PCNA to limit the unnecessary introduction of point mutations.

The p21 protein has been shown to non-covalently bind with strong affinity to PCNA in a manner that does not seem to affect the loading of PCNA onto DNA, or the ability of PCNA to move along DNA (Gulbis et al. 1996). However, the binding of p21 to PCNA does affect other PCNA functions, usually through p21 obstructing the binding sites of other molecules that interact with PCNA. In a recent study, for example, p21 was shown to prevent the interaction of PCNA with Pol η (a TLS polymerase), without affecting DNA polymerases involved in normal DNA replication (Mansilla et al. 2013). Consequently, TLS activity is restricted as long as a sufficient level of nuclear p21 is maintained to prevent PCNA-Pol η activity. In another study, a p21 peptide containing the PCNA binding domain was shown to block both DNA replication and NER (Jung et al. 2010).

It is important to note that the current understandings on the regulatory effects of p21 on PCNA are highly controversial. For example, in response to UV-induced DNA damage, nuclear p21 interactions with PCNA have been shown to both promote and inhibit PCNA functions in DNA repair (Lee et al. 2009). This can be explained by reports suggesting that p21 activities in particular cellular processes have either positive or negative functions depending on the experimental context (e.g. cell type) (Jung, 2010). In general, however, the majority of studies suggest that p21 functions to inhibit various

DNA repair pathways, by disrupting PCNA interaction with DNA repair molecules as well as promoting PCNA ubiquitin-dependent degradation (Jung, 2010).

2.4.4 UV-Induced Pathways

The severity of UV-induced DNA damage determines the type of cellular stress response in a multicellular organism. In particular, there are two opposing pathways a cell may undergo upon detection of UV-induced DNA damage: DNA repair followed by continued cell proliferation and inhibition of DNA repair followed by programmed cell death. For example, if DNA damage is not too severe and may be repaired with little risk of carcinogenic mutations, then the cell usually takes a pathway that results in DNA repair followed by continued cell proliferation. On the other hand, if DNA damage is extremely severe and there is a high risk of mutagenic DNA repair and carcinogenesis, then the cell typically favors a pathway called apoptosis or programmed cell death. The p21 protein is known to play a critical role in both DNA damage-induced cellular pathways, which is also called the DNA damage response (DDR).

While p21 is known to contribute to the regulation of cell cycle progression and apoptosis, the exact role of p21 in UV-induced DDR is still unclear. For example, one study showed that p21 plays a negative role in the DNA repair of UV-induced DNA damage, while another study indicated the opposite (Lee et al. 2009). Also, Lei et al. (2010) showed that p21 has an anti-apoptotic function, and must be degraded following UV irradiation to facilitate apoptosis of premalignant cells. While in direct opposition, Kanagasabai et al. (2010) showed that p21 has a pro-apoptotic function, and that its prolonged expression in the nucleus enhanced apoptosis. These contradictory reports

suggest that UV-induced p21 activities are dependent on experimental variables, such as cell type, UV wavelength and irradiation dose, and post-UV incubation period length.

Several studies have supported the hypothesis that UV wavelength and irradiation dose affects p21 functions and expression levels. For example, Mansilla et al. (2013) showed that p21 is degraded following UVC irradiation of HeLa cells in a dose-dependent manner. If the UVC dose was sufficient to induce DNA lesions that require TLS for repair, then p21 was found to be degraded in order for PCNA to recruit Pol η and initiate TLS. It was shown that while PCNA bound to p21 at replication forks serves to control the timing of TLS onset, the appropriate removal of p21 from replication forks is a crucial event required for DNA repair to occur (Mansilla, 2013). Bendjennat et al. (2003) also found that low ($< 40 J/m^2$) but not high doses of UVC causes p21 degradation in a variety of cell types immediately after irradiation, and that cell cycle arrest occurs despite p21 degradation. Like the study performed by Mansilla et al. (2013), this study found UVC-induced p21 degradation to be necessary for DNA repair to occur. The study also suggested that at high UVC doses, DNA damage would be overwhelming, and therefore it would be futile to attempt repair by degrading p21 and risk having the survival mutated cells (Bendjennat, 2003).

In opposition to reports suggesting that UV-induced p21 expression inhibits DNA repair and leads to apoptosis, Lei et al. (2010) showed that in normal human epidermal keratinocytes treated with $20 mJ/cm^2$ of UVB radiation, p21 has an anti-apoptotic function. In this study, post-UVB p21 levels were initially reduced at 1.5 hours, but later increased around 6 and 9 hours (Lei, 2010). The increase in p21 levels was shown to protect the UVB-irradiated keratinocytes from apoptosis. In agreement with this, a recent

review suggested a model (see Figure 2.10) in which p21 protein will promote DNA repair in the presence of low levels of DNA damage, while its removal will favor apoptotic cell death when high levels of DNA damage are present (Cazzalini, 2010).

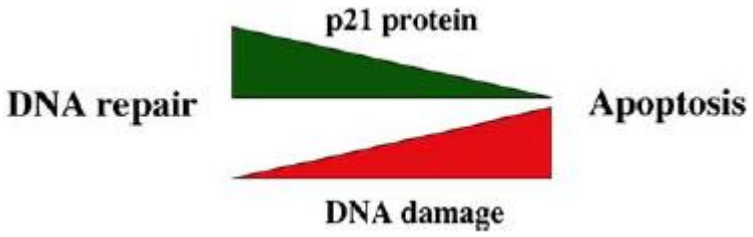

Figure 2.10 DNA repair and apoptosis dependency on p21 protein and DNA damage (Cazzalini, 2010).

The hypothesis that post-UV incubation period lengths affect p21 activities is supported by the recent study performed by Kanagasabai et al. (2010). In this study, human adenocarcinoma cells (MCF-7) were treated with UVC radiation to study the protective role of heat shock protein 27 (Hsp27) and p21-dependent survival pathways. UV-induced DNA damage was found to immediately increase Hsp27 expression and nuclear p21 levels, and facilitated the stabilization of Akt, also known as protein kinase B (Kanagasabai et al. 2010). In turn, Akt was found to phosphorylate p21 and translocate it to the cytoplasm where it was degraded, causing cell survival through the removal of the p21-induced cell cycle arrest (Kanagasabai et al. 2010). The location and levels of p21 were found to greatly depend on post-UV incubation times. For example, high levels of p21 localized in the nucleus were found at 8hrs post-UV treatment (Kanagasabai et al. 2010). This was attributed to the idea that p21 must be initially stabilized in the nucleus after UV-induced DNA damage to halt the cell cycle and allow DNA repair to occur. Also, nuclear p21 levels, along with cell cycle arrest occurrences, were found to be significantly low around 24hrs post-UV treatment, while cytoplasmic p21 levels were

found to be relatively high at this time. The study suggested that if nuclear p21 levels remained high after the 8-hour post-UV time point, then p21 would function to enhance apoptosis. Consequently, nuclear p21 was considered to have an anti-apoptotic function up to 8 hours post-UV irradiation; while after 8 hours post-UV irradiation, nuclear p21 was considered to have a pro-apoptotic function. While the critical post-UV time points of p21 expression suggested in this study may have been highly dependent on the experimental procedures used, they provide a practical trend that has been supported in other studies: that after the detection of UV-induced DNA damage, p21 levels initially increase in the nucleus to promote DNA repair and cell survival, and is later translocated to the cytosol where it is degraded to prevent apoptosis (Hattinger et al. 2002). Thus, p21 may play dual roles in cell cycle regulation mechanisms by functioning to either promote or inhibit tumorigenesis, depending on the cellular and environmental context.

2.5 Sphingomyelin

In milk, fat droplets are surrounded by a thin membrane known as the milk fat globule membrane (MFGM) (Evers, 2004). This membrane, responsible for emulsifying milk fat in the aqueous phase, is where the majority of milk phospholipids are found (Evers, 2004). Of the total phospholipids found in bovine milk, the most abundant phospholipids are phosphatidylcholine (34.5%), phosphatidylethanolamine (31.8%), and sphingomyelin (25.2%) (Miura et al. 2004). These milk phospholipids are all known to have important functions in human health, such as regulation of inflammation and chemotherapeutic activity (Contarini et al. 2013). In particular, the degradation products of sphingomyelin, i.e. ceramide, sphingosine, and sphingosine-1-phosphate (S1P), are considered as highly bioactive compounds and have major effects on cell regulation

(Vesper et al. 1999). For example, ceramide and sphingosine are known to inhibit growth and induce apoptosis of unhealthy cells, while S1P is known to promote growth and inhibit apoptosis (Vesper, 1999).

Sphingomyelin, classified as a complex sphingolipid, consists of a hydrophilic polar head group called phosphorylcholine, and two nonpolar hydrocarbon tails (sphingosine and a fatty acid) which make up ceramide (see Figure 2.11) (Sturm, 2013). Sphingomyelin plays an essential role in eukaryotic cell viability, as displayed by the inability of mammalian cells to survive in culture when they are unable to produce sphingomyelin; however, the precise single function that sphingomyelin fulfills that is necessary for cell survival is not clear (Gault et al. 2010). Sphingomyelin is one of the major lipid components of cell membranes in animals, with significant amounts found in the myelin sheath of neurons (Nagata et al. 2006). It is also located in lipoproteins (especially LDL and HDL) and other lipid-rich structures, such as skin (Vesper, 1999). As with all sphingolipids, sphingomyelin is thought to be exclusively localized to the outer leaflet of the plasma membrane, as well as the luminal side of the Golgi apparatus (Vesper, 1999). Sphingomyelin and other sphingolipids affect cell membrane structure and function by associating closely with cholesterol in the formation of lipid rafts (Gniadecki et al. 2002). Helping to compartmentalize cellular processes to specific regions along the plasma membrane, lipid rafts are small, highly ordered and rigid membrane domains that organize signaling molecules to promote kinetically favored interactions (Gniadecki et al. 2002). Although there is little evidence that dietary sphingomyelin itself is bioactive, its degradation products (i.e. ceramide and sphingosine)

derived in the intestine have been shown to have a large bioactive impact on the developmental fate of many cell types (Hellgren, 2001).

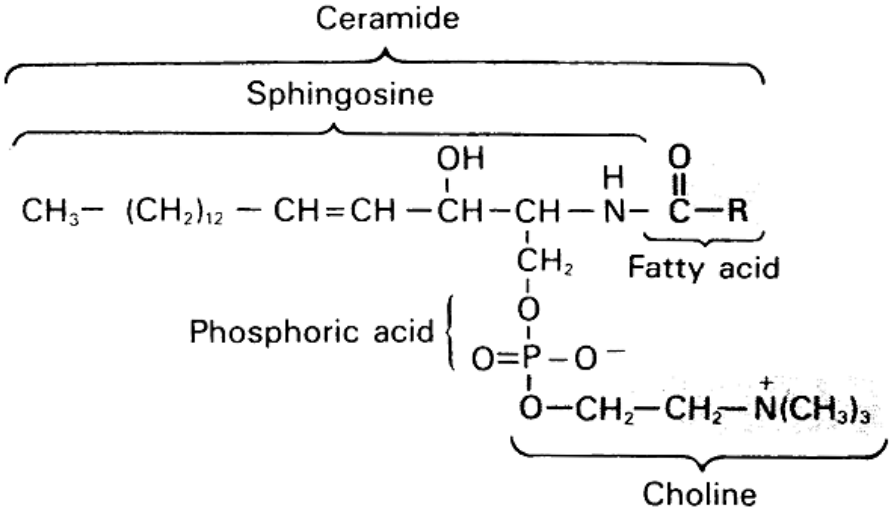

Figure 2.11 Structure of sphingomyelin (Sturm, 2013).

Sphingomyelin is synthesized naturally in eukaryotic cells through the action of sphingomyelin synthases (SMS) (Gault, 2010). SMS catalyzes the reaction in which a phosphorylcholine head group is transferred from phosphatidylcholine to a ceramide to produce sphingomyelin and diacylglycerol (DAG) (Gault, 2010). In humans, there are two SMS genes, SMS1 and SMS2, which are predominantly located in the trans-Golgi and plasma membrane, respectively (Gault, 2010). The catabolism of sphingomyelin occurs through the action of the sphingomyelinase (SMase) family, a family of hydrolase enzymes that is broken down into three groups: acid SMases, alkaline SMases, and neutral SMases (Gault, 2010). Acid SMases are mainly found in lysosomes where they break down sphingomyelin on endosomal membranes, and can also be secreted extracellularly to break down sphingomyelin in lipoproteins and on the outer leaflet of the plasma membrane (Gault, 2010). Alkaline SMases are exclusively localized in the liver and intestine, where they degrade dietary sphingomyelin (Gault, 2010). Less is

known about neutral SMases; however, different species have been predominantly found in the endoplasmic reticulum (ER) and on the cytosolic leaflet of the plasma membrane and Golgi of cardiac and skeletal muscle cells (Gault, 2010). Although the three types of SMases are all localized to different regions, they all function similarly by catalyzing the hydrolysis of sphingomyelin to produce ceramide and phosphocholine (Gault, 2010). Following this step, ceramide can be broken down into sphingosine (in specific organelles), which is broken down into S1P (in the cytosol), and finally, hexadecenal and phosphorylethanolamine (in the ER) (see Figure 2.12) (Gault, 2010). Extracellular signals of platelet-derived growth factor (PDGF) and TNFα are known to bind to their respective cell membrane receptors and induce sphingomyelin catabolism within the cell by activating SMase or other degradation enzymes (Gault, 2010).

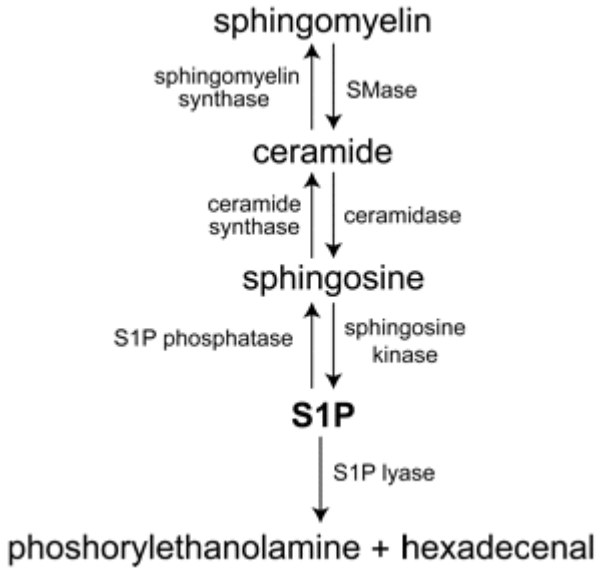

Figure 2.12 Sphingomyelin catabolism (adapted from Nagata, 2006).

Sphingolipids, such as sphingomyelin, make up about 25% of the lipids located in the stratum corneum and are considered to be a major element of the epidermal permeability barrier (Holleran et al. 1990). Both acid and neutral SMases are found in the

skin, and function to produce ceramide, sphingosine, and S1P from sphingomyelin to act as secondary messengers in different skin cell regulation pathways (Holleran et al. 1990). Because of this, numerous studies have investigated the potential of sphingomyelin breakdown products as targets for cancer therapy. For example, Pyne et al. (2012) showed S1P signaling is directly involved in tumorigenesis through its positive regulation of cancerous cell growth and survival. In addition, Birt et al. (1998) showed that the topical application of low doses of sphingosine on mice skin can prevent the development of early stages of skin carcinogenesis to carcinomas; and on the other hand, high doses of sphingosine can promote skin carcinoma development. While further studies are needed to fully comprehend the exact roles sphingomyelin breakdown products play in skin cancer, the use of these breakdown products as targets for skin cancer therapy is promising.

Exogenous sphingomyelin has been shown to be taken up and incorporated into different cell types in culture, such as human skin fibroblasts (Kudoh et al. 1983) and rat cerebellar neurons and astrocytes (Riboni et al. 1994). In particular, Pillai et al. (1999) reported that in human keratinocyte cultures, exogenously added sphingomyelin is taken up by the cells and is incorporated into the cell plasma membrane. Furthermore, the exogenously added sphingomyelin was found to inhibit keratinocyte differentiation and activate proliferation; however, the precise mechanisms behind these processes remained to be elucidated (Pillai et al. 1999). Nevertheless, it was hypothesized that the exogenously added sphingomyelin could have disrupted the lipid rafts located throughout the cell membrane, increasing membrane fluidity and permeability, which may have led to the observed increase in keratinocyte proliferation (Pillai et al. 1999). This hypothesis

is based off of previous findings of a positive correlation between membrane fluidity and cell proliferation (Tanaka et al. 1989).

2.6 Overview and Scope of Thesis

The premise of this thesis is based on previous findings (Russell et al. 2010 and Achay, 2011) that bovine milk sphingomyelin has the potential for protecting human skin from UV-induced DNA damage. This may lead to future research into the potential of sphingomyelin as a chemopreventive agent for non-melanoma skin cancer. Currently, however, the exact bioactive mechanisms of sphingomyelin *in vitro* have yet to be fully elucidated. Consequently, this thesis aims to provide further investigation on the *in vitro* use of bovine milk sphingomyelin for its protection against UV-induced DNA damage in a human skin model system, namely normal human epidermal keratinocytes.

This thesis utilizes immunocytochemistry to obtain fluorescence intensity values of p21 expression in normal human epidermal keratinocytes treated with different factors (either UV or no UV treatment, and either sphingomyelin or no sphingomyelin treatment). These intensity values are used to statistically analyze whether or not there is an interaction between sphingomyelin treatment and UV photodamage, as indicated by p21 expression. Although immunofluorescence can be a useful technique for observing cellular mechanisms, numerous factors contribute to obtaining reliable images, many of which rely on the experimental protocol used. Thus, this thesis also aims to optimize the complete protocol used for the detection of p21 expression in cultured keratinocytes, including procedures for UV and sphingomyelin treatments. This is done by determining the appropriate reagents and concentrations needed to achieve reliable images of p21 expression; and by determining the optimal incubation times and UV treatment doses to

provide clear and consistent p21 expression. The same 302nm UV lamp (95-0251-01, UVP, LLC, Upland, CA) used in the previous studies is used in this thesis to irradiate the cells following a 24hr sphingomyelin treatment, in which bovine milk sphingomyelin is exogenously added to the culture medium of the appropriate treatment groups.

A detailed description of the preliminary studies performed in order to optimize the final protocol is given in Chapter 3, while a description of the final protocol itself is given in Chapter 4. In Chapter 5, the effects of bovine milk sphingomyelin and UV radiation on nuclear p21 fluorescence intensity in human keratinocytes are statistically evaluated. In Chapter 6, the implications of sphingomyelin's protective effects against UV photodamage (i.e. nuclear p21 expression) in human keratinocytes are discussed, as well as challenges and limitations of the finalized protocol. Conclusions made using the results compiled in Chapter 5 are also given in Chapter 6. Lastly, this thesis is concluded with recommendations for future work, given in the final section of Chapter 6.

Chapter 3: Preliminary Studies

3.1 General Experimental Overview

The foundational protocol used in this thesis consisted of 6 basic steps: 1) cell cultivation, 2) sphingomyelin (SM) treatment, 3) UV irradiation, 4) cell fixation and immunostaining, 5) confocal imaging, and 6) image analysis. While one of the main goals was to obtain reliable fluorescent images of keratinocyte p21 expression, it was essential to optimize steps 2-4 of the foundational protocol through preliminary studies and preparation. The preliminary studies carried out in this thesis are briefly discussed in the following paragraph; a flowchart of the experimental studies is given in Figure 3.1. More detailed descriptions of the preliminary studies are given in sections 3.2-3.8.

The first primary concern that arose when beginning the experimental studies of this thesis was being able to obtain reproducible UV doses. To address this issue, an initial prototype of a UV containment apparatus (called the UV tent; see Figure 3.2A) was created to help standardize the UV lamp output and irradiation doses given to the cells. Using the UV tent, an initial preliminary study was performed to analyze keratinocyte p21 expression after four different post-UV incubation periods: 1hr, 10hrs, 24hrs, and 36hrs. The results of this study led to the selection of 24hrs as the optimal post-UV incubation period, and also revealed the need to improve upon the UV tent design by creating a second prototype. Thus, the UV box (see Figure 3.2B) was created to replace the UV tent. After this, a second preliminary study was performed to analyze keratinocyte p21 expression using the 24hr post-UV incubation period and three different UV doses: 10, 20, and 40mJ/cm^2. While numerous issues were encountered through this study, the results ultimately led to the selection of 40mJ/cm^2 as the optimal UV dose, and

the use of formaldehyde as the optimal fixative reagent (compared to Histochoice). Next, another preliminary study was performed to evaluate different primary and secondary antibody concentrations for effectively staining p21 protein. This study led to the selection of 1/400 as the optimal dilution for both primary and secondary antibody solutions. In an additional preliminary study, three different SM concentrations were analyzed for their treatment effects on keratinocytes: 0.1%, 0.5%, and 1.0% (w/v). After analyzing the results, 0.1% was selected as the optimal SM concentration. Following this preliminary study, two complete experiments were performed to gather data for the final results of this thesis. However, the combined data was insufficient for performing a definitive statistical analysis. Because cells from different passages are known to acquire different characteristics (see Chapter 2.3) and because inherent variables arise from performing separate experiments at different times, it was decided that doing one large experiment using cells from the same passage would be more ideal. Before performing the final experiment, however, one last preliminary study was performed to compare the current blocking reagent used (Image-iT FX Signal Enhancer, Life Technologies, Grand Island, NY) with a potentially more cost effective and readily available alternative, donkey serum. This study led to the selection of donkey serum as the optimal blocking reagent.

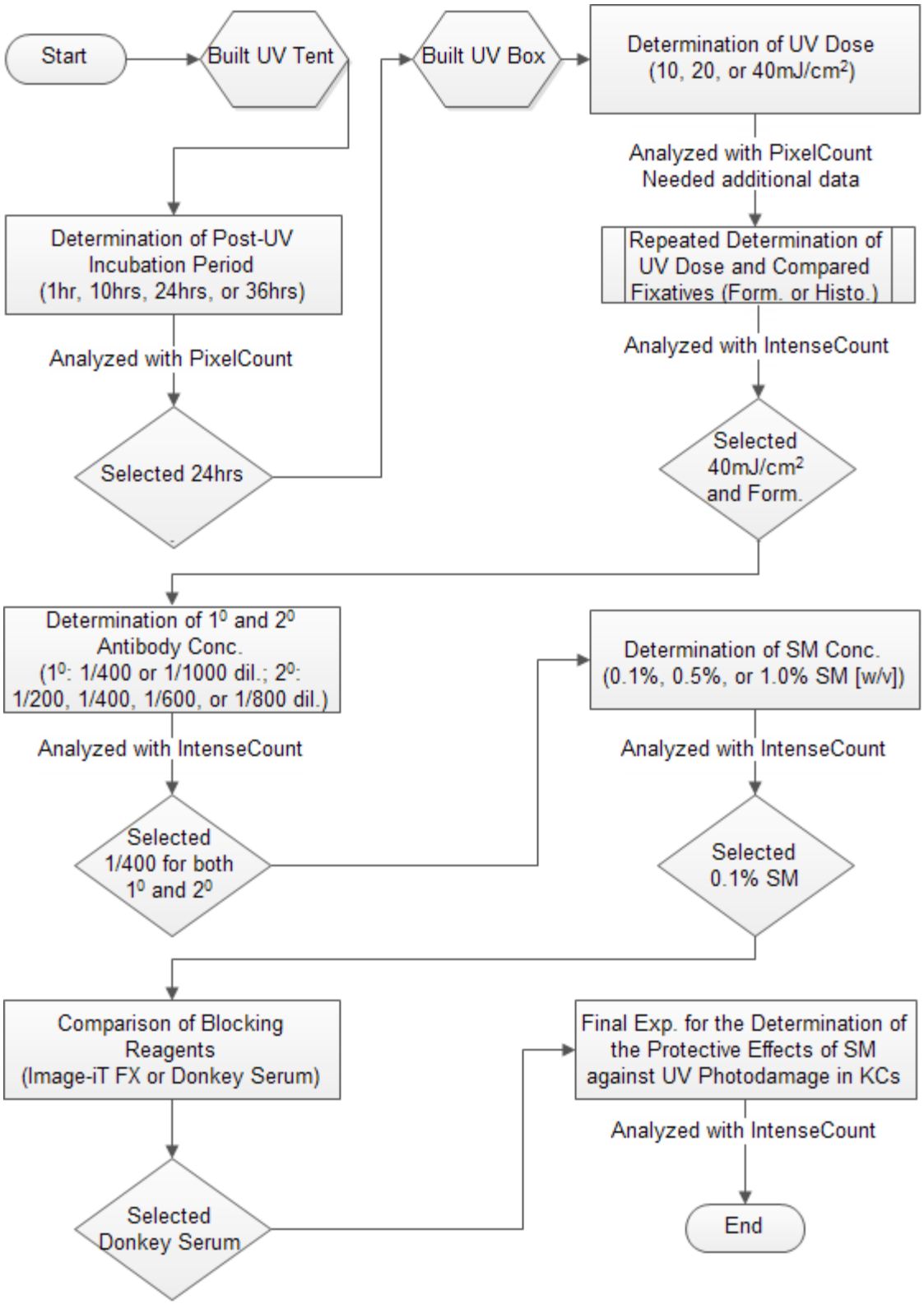

Figure 3.1 Flowchart of experimental studies.
Abbreviations: Form. (formaldehyde), Histo. (Histochoice). Conc. (concentration), SM (sphingomyelin), Exp. (experiment), KCs (keratinocytes).

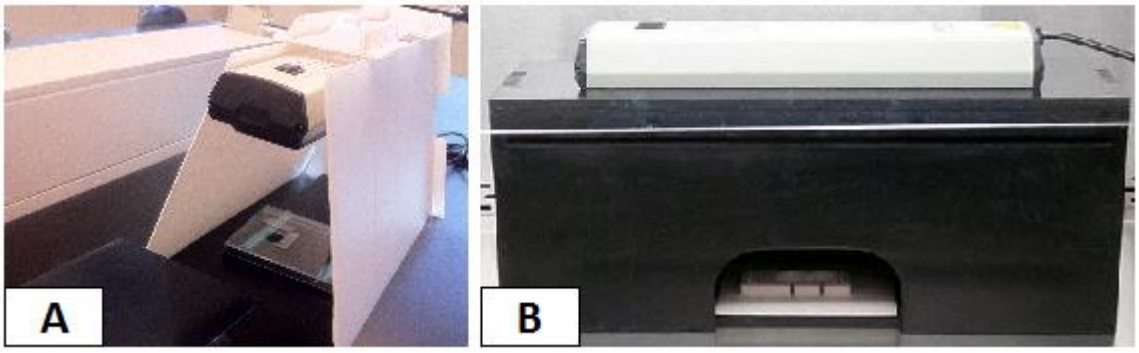

Figure 3.2 UV containment apparatuses. A) UV tent encasing UVB lamp and stand. B) UV box with UVB lamp in place.

To analyze the images obtained from the various experiments performed, two MATLAB programs were written by Bradley Schab (a graduate student at California Polytechnic State University). The first program created, called PixelCount, was used to calculate a p21 expression ratio (number of p21-expressing nuclei/total nuclei) per image. A flowchart describing the PixelCount program is given in Figure 3.3., and the program code in its entirety may be found in Appendix A. The PixelCount program calculates the p21 expression ratio by first opening each image one-by-one from a specified folder. Once an image is opened, the blue and green channels are separated. The blue channel (cell nuclei) is thresholded to create a binary image. In this binary image, connected pixels of a minimum size of 200 pixels (considered to be the minimum size of a cell nucleus) are computed and any holes within connected pixels are filled to form a solid nucleus. In the green channel (p21 expression), all green pixels are trimmed out except for those overlapping a single cell nucleus defined by the binary image of the blue channel. The image of the green pixels within a single nucleus is then thresholded to create a binary image. In this binary image, connected pixels of a minimum size of 5 pixels are computed, and the total green pixel area within a nucleus is determined. A

percentage ratio of 2% green pixels within the total nucleus pixel area was considered to be the minimum percentage ratio needed for a nucleus to be counted as positive for nuclear p21 expression. Using this threshold, the program steps through each nucleus one-by-one and finds all nuclei containing greater than 2% green pixels. Once the program scans the entire image, it reports (in an Excel spreadsheet file) the number of nuclei containing greater than 2% green pixels (p21-expressing nuclei), the total number of nuclei within the image, and the ratio of p21-expressing nuclei to total nuclei (p21 expression ratio) for all images located in the specified folder. A high p21 expression ratio was correlated with high nuclear p21 expression.

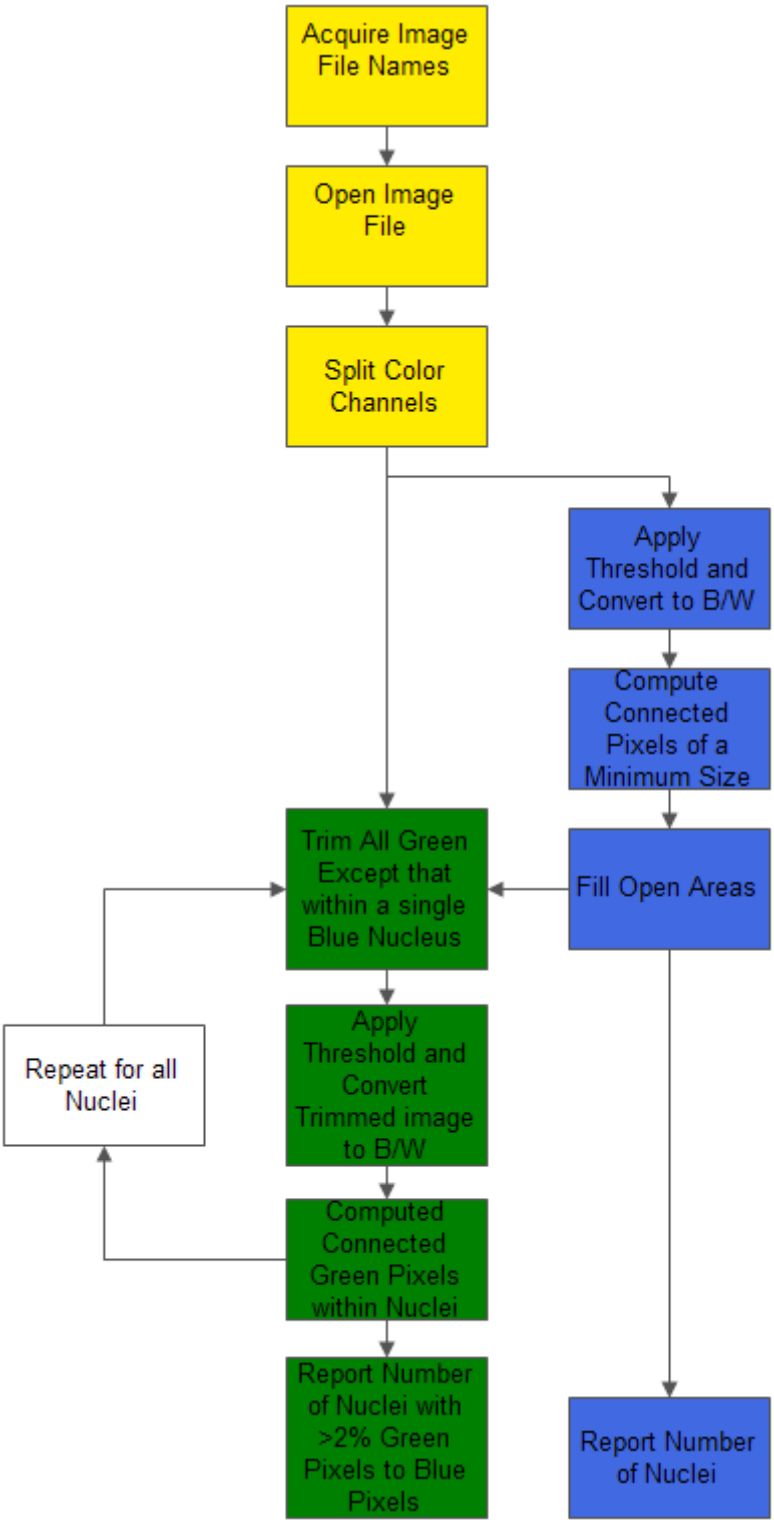

Figure 3.3 Flowchart of the PixelCount MATLAB program.

The second MATLAB program created, called IntenseCount, was used to calculate the mean pixel intensity (0-255) of nuclear p21 expression (green pixels within blue nuclei) per image. A flowchart describing the IntenseCount program can be seen in Figure 3.4. The program works by opening each image one-by-one from a specified folder. Once an image is opened, the blue and green channels are separated. The blue color channel (cell nuclei) is thresholded to create a binary image. In the binary image, connected pixels of a minimum size of 200 pixels are computed and any holes within the connected pixels are filled to form a solid nucleus. In the green color channel (p21 expression), all green pixels are trimmed out except for those overlapping a single cell nucleus defined by the binary image of the blue channel, and the nuclear p21 mean pixel intensity is computed. The program steps through each nucleus one-by-one to calculate the nuclear p21 mean pixel intensity for all nuclei. Once the program scans the entire image, it reports (in an Excel spreadsheet file) the overall mean nuclear p21 intensity for all nuclei and the total number of nuclei within the image for all images located in the specified folder. This program was considered to provide a more valuable analysis than PixelCount, since it did not require thresholding of the p21 data and, more importantly, took into account the intensity of p21 expression. A high value of nuclear p21 pixel intensity was correlated with high nuclear p21 expression. The IntenseCount program code in its entirety is given in Appendix B.

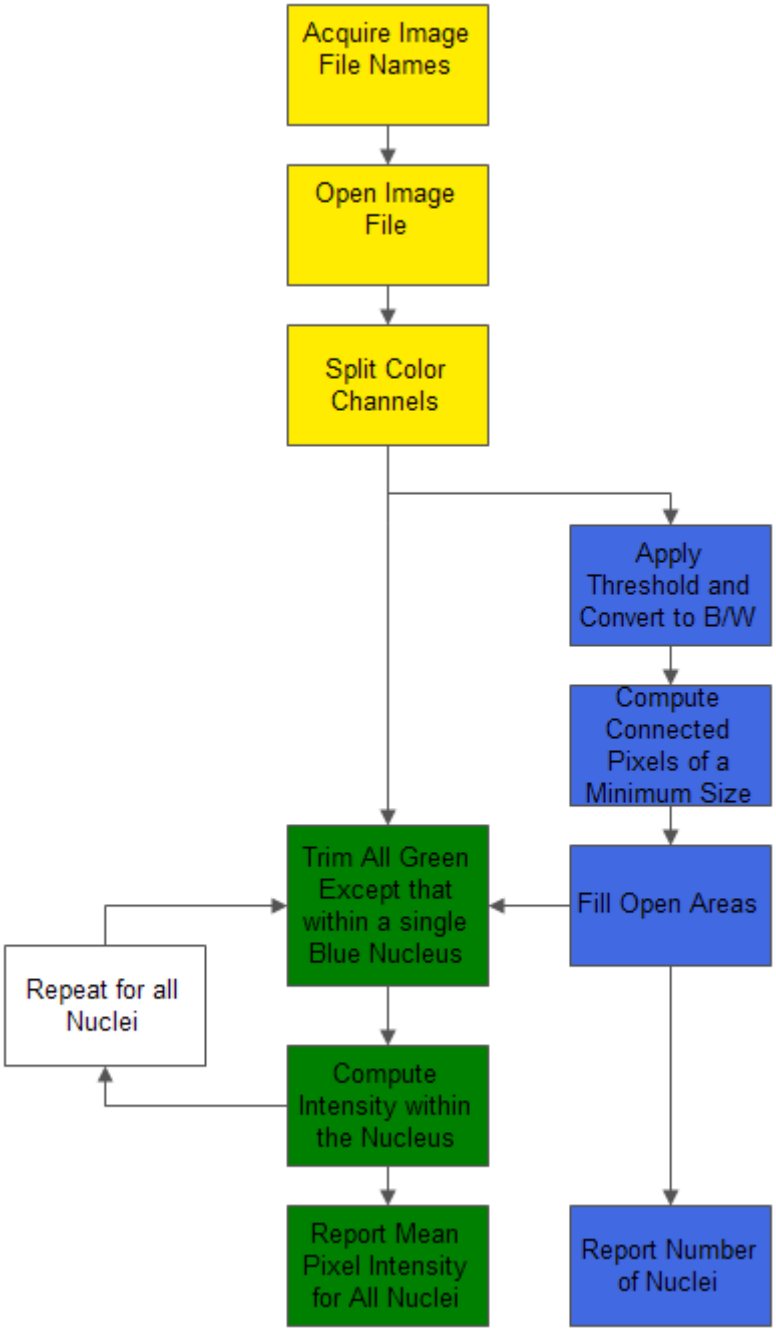

Figure 3.4 Flowchart of the IntenseCount MATLAB program.

3.2 UV Treatment Standardization

3.2.1 Overview

In order to obtain reliable and reproducible results, the UV irradiation procedures were standardized under the guidelines of Bolton et al. (2003). Two prototypes of a

bench-scale UV containment apparatus were created for a UV lamp (95-0251-01, UVP, LLC, Upland, CA). Knowing that the output of many UV lamps is highly sensitive to temperature variations (Bolton et al, 2003), the main design criterion was to create an enclosure that decreases changes in air drafts which affect the local system temperature. Other design criteria were to create an easy-to-assemble compact enclosure that can fit inside a sterile hood, an accurate shutter system for UV dose repeatability, and a tray to hold a power meter sensor (S120UV, ThorLabs, Newton, NJ) and cell culture plate to provide accurate sensor readings and consistent specimen placement across every UV treatment. Also, only durable materials that could withstand sterilization with isopropyl alcohol were used. A power meter sensor system (ThorLabs, Newton, NJ) was used to test how well each apparatus prevented UV radiation from escaping the walls of the apparatus and the effectiveness of the shutter system. This was done by ensuring the sensor detected little to no UV irradiance outside of the apparatus and inside of the apparatus when the shutter was closed.

3.2.2 UV Tent Containment Apparatus

The first prototype of a bench-scale UV containment apparatus was the UV tent. This design was constructed from inexpensive, readily available materials, such as white corrugated plastic, black electrical tape, and material from a T-225 culture flask. The UV tent consisted of four light-weight walls made of corrugated plastic, a small table-like manual shutter also made of corrugated plastic and covered with black electrical tape, and a clear plastic tray used to align a 4-well cell culture plate or power meter sensor at a precise location underneath the UV lamp (see Figure 3.5). The four walls of the tent were designed to enclose the UV lamp and stand shown in Figure 3.5D, with one open end for

accessing the inside. To UV irradiate cells, the UV lamp was first turned on and the manual shutter was slid inside the tent. After a 5 minute period of the lamp warming up, the 4-well plate was carefully placed on the alignment tray (see Figure 3.5B) inside the tent, with the cover of the plate removed. The cells were then exposed to UV radiation by manually sliding out the shutter. The shutter was slid back inside immediately after the exposure period was over and the 4-well plate was returned back to the incubator.

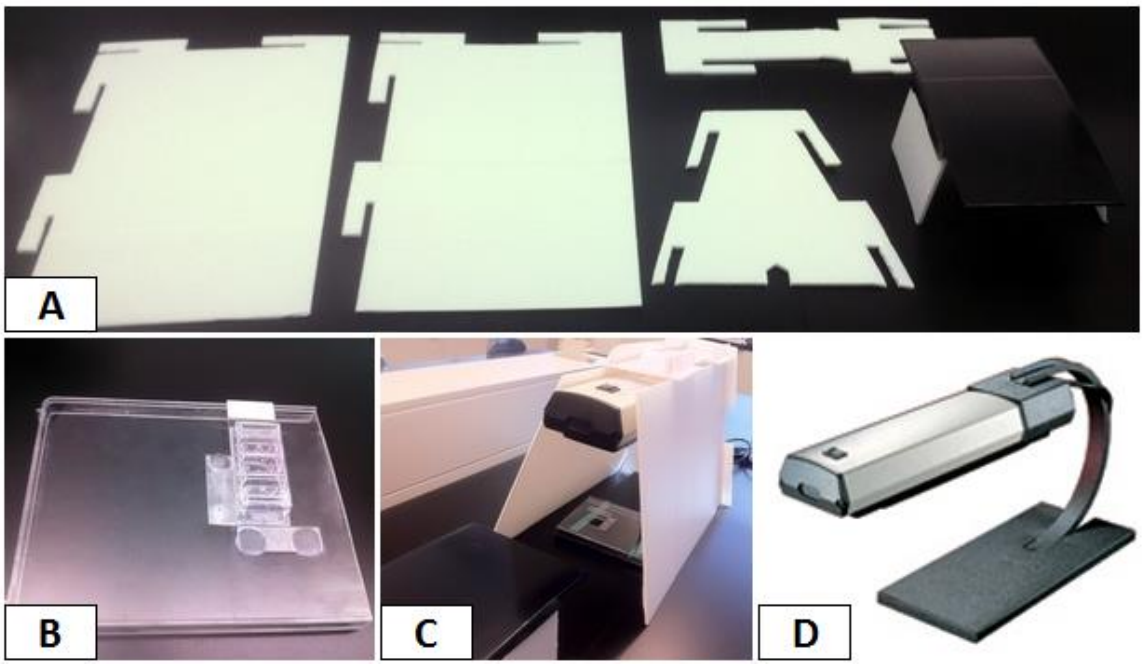

Figure 3.5 UV tent containment apparatus. A) Disassembled UV tent, showing the four walls and manual shutter. B) Alignment tray with 4-well plate. C) Open end of UV tent. D) UV lamp and stand (UVP.com).

The UV tent was a quick and simple solution for creating a UV lamp enclosure. When tested with the power meter sensor, the shutter was found to adequately block out UV radiation from the sample area and there was no significant amount of UV power detected outside the walls of the UV tent. While the UV tent was a good first attempt at creating a UV lamp enclosure, it showed to have many flaws. For example, the corrugated plastic walls became more flimsy when sprayed with IPA; and when

assembled, they left many gaps at their intersections for air drafts to pass through. Also the relatively large number of parts to the system (8 parts total) made setting up difficult since each part needed to be sterilized with IPA before being placed inside the sterile hood. Therefore, a second prototype, the UV box, was created to address these issues and is described in the next section.

3.2.3 UV Box Containment Apparatus

The UV box was constructed out of black Delrin plastic sheets, used to form a rectangular box with a removable top and bottom. The four walls of the box were permanently assembled (using aluminum alignment pins and glue) to minimize the number of parts to the system. The top had a rectangular cutout for placement of the UV lamp; while the bottom had railings to align a removable ABS plastic tray (rapid prototyped), which was used to hold the 4-well plates and the power meter sensor. In the front face of the UV box, a 6-inch wide window was made to slide the plastic tray in and out of the box during UV irradiation. Since the UV box was used for the finalized protocol, the UV irradiation procedures involving the UV box are discussed in detail in Chapter 4. Representative images of the UV box assembled inside the sterile hood with the UV lamp in place, and the ABS plastic tray holding the power meter sensor and two 4-well plates are shown in Figure 3.6.

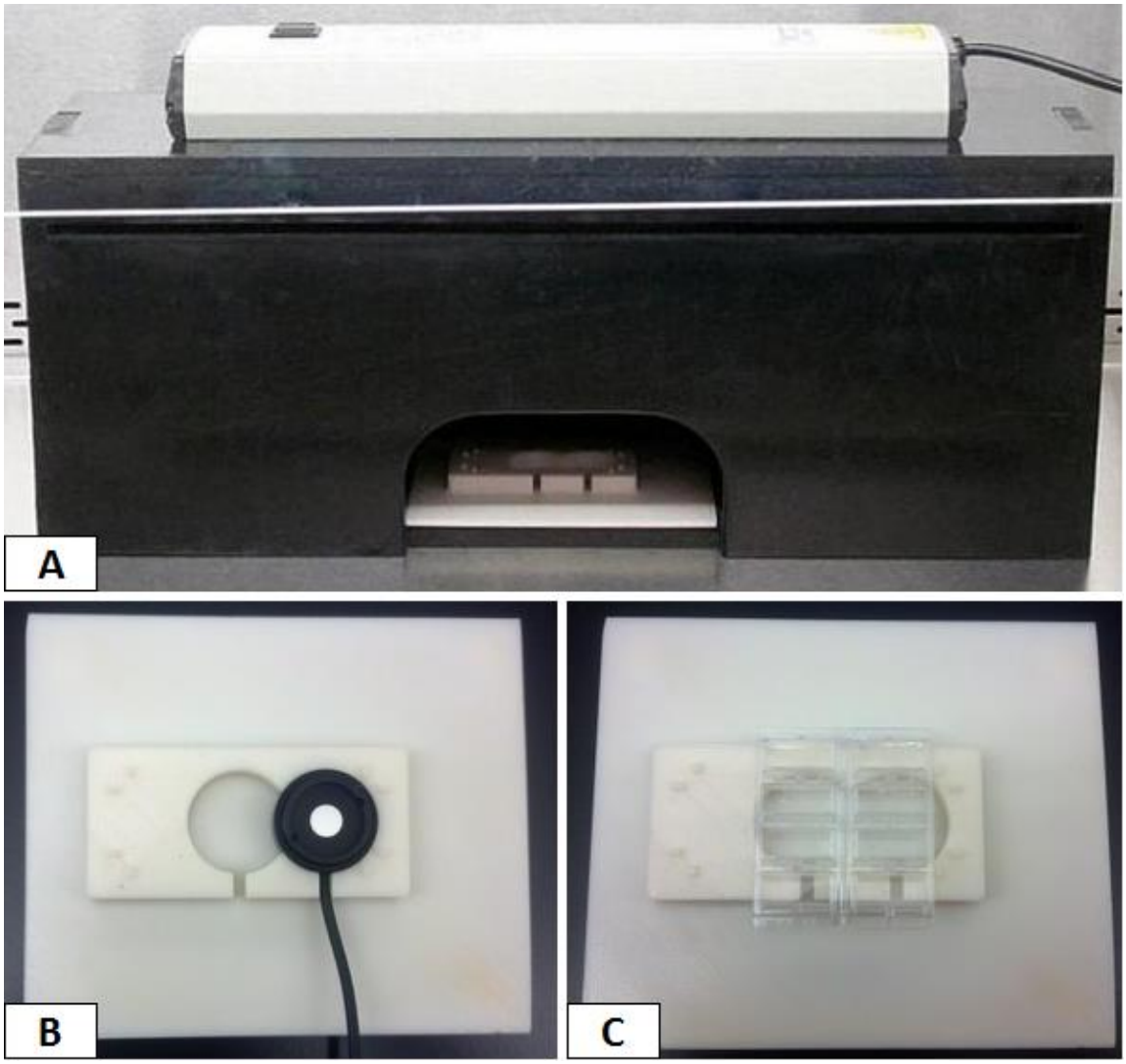

Figure 3.6 UV box containment apparatus. A) UV box and UV lamp assembled. B) ABS plastic tray holding the power meter sensor. C) ABS plastic tray holding two 4-well plates.

Compared to the UV tent, the UV box was significantly more durable and had fewer parts, altogether (5 parts total). Additionally, the UV box was more capable at decreasing changes in air drafts than the UV tent, since the walls of the box were flush with one another and the window opening was smaller in size. When tested with the power meter sensor, there was no significant amount of UV irradiation detected

anywhere outside the walls of the UV box. Thus the UV box was used as the final prototype for a UV containment apparatus.

Nevertheless, the UV box design can still be considerably improved upon. The major improvement that can be done would be to make an apparatus that is capable of collimating the UV beam. Such a design would narrow and align the UV rays parallel to one another so that they are normal to the sample surface and spatially homogeneous. This would provide a more standardized and predictable UV beam, and would allow UV intensity to be measured more accurately, since light sensors typically only measure light normal to the sensor's surface (EPA, 1986). Quasi-collimation can be achieved with apertures placed at a few distances from the lamp to define the UV beam and create quasi-parallel radiation (Bolton, 2003). However, in order for any aperture to be effective at creating quasi-parallel radiation, the distance between the sample surface to be irradiated and the UV lamp should be at least 20cm to minimize the effect of UV rays radially spreading out away from the source (Bolton, 2003). This distance is also thought to be important for limiting changes in temperature due to air drafts caused by shutter movement. Due to limited time and resources, the UV box was not tall enough to benefit from the addition of an aperture or shutter, as it provided a distance of only 18cm from the UV lamp to the sample surface. Therefore, a future prototype should be made taller to provide a large enough distance for quasi-collimating the UV beam using apertures, and should incorporate a shutter for more accurate UV dosing.

Another improvement that can be made is using a lighter weight material that still provides sufficient durability. The high-density Delrin plastic used for the UV box made the apparatus undesirably heavy and difficult to carefully transport into and out of the

hood. Thus, using a lighter weight material with sufficient durability would make designing a taller, yet easy-to-assemble apparatus more plausible. Lastly, redesigning the ABS plastic tray to securely hold several 4-well plates at one time would improve the efficiency of the UV irradiation process.

3.3 Determination of Post-UV Incubation Period

3.3.1 Overview

In the study performed by Kanagasabai et al. (2010) (see Chapter 2.4.4), the activity of p21 in MCF-7 cells was shown to be dependent on post-UV incubation times. Based on this study, as well as the studies by Lee et al. (2009) and Hattinger et al. (2002), it was hypothesized that following UV-induced DNA damage, p21 levels initially increase in the nuclei of human keratinocytes to promote DNA repair and cell survival; but at a later time point, nuclear p21 becomes pro-apoptotic and must be translocated to the cytosol where it is degraded to prevent apoptosis. In cells treated with high doses of UV radiation (>40mJ/cm^2), nuclear p21 is not degraded and persists in the cell for up to 24hrs post-UV to prevent mutagenic DNA repair (Bendjennat et al. 2003). Based on this knowledge, it was important to determine the optimal post-UV incubation period for human keratinocytes, which was to be characterized as producing the greatest difference between levels of nuclear p21 expression in non-UV-treated and UV-treated keratinocytes. Significantly different levels of nuclear p21 expression in UV-treated keratinocytes, compared to those in non-UV-treated keratinocytes, were assumed to be a reliable indication of UV-induced DNA damage and the cellular stress response.

The following post-UV incubation periods were studied: 1hr, 10hrs, 24hrs, and 36hrs. Eight 4-well plates of normal human epidermal keratinocytes were used, with 4

plates treated with 60mJ/cm^2 of 302nm UVB radiation and the other 4 plates (controls) treated with no UV radiation. The UVB dose of 60mJ/cm^2 was used because it had been reported as the minimal erythema dose (MED) for normal human skin irradiated with 305nm UV light (Giacomoni, 2007). A schematic of the 4-well plate setup used in this preliminary study is shown in Figure 3.7.

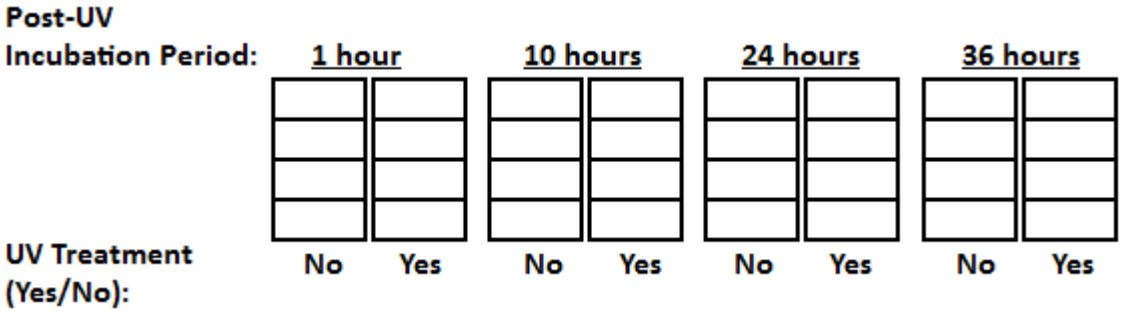

Figure 3.7 Four-well plate setup for the determination of the optimal post-UV incubation period.

A fluorescent live/dead stain (L-3224, Life Technologies, Grand Island, NY) was used on one well of every 4-well plate to stain live cells green and dead cells red, immediately following the corresponding post-UV incubation period. Only one well for each treatment group was stained with the live/dead stain, since the stain was simply intended for making casual observations on the correlation between nuclear p21 expression and cell viability for each post-UV incubation period. One image of each live/dead-stained cell culture well was taken using a widefield fluorescence microscope and saved as a TIFF file. The live/dead images were then analyzed using ImageJ, image processing software created by the National Institutes of Health (NIH). In ImageJ, the RGB color channels for each live/dead image were split and thresholded to create a binary image for both the green (live) channel and the red (dead) channel. After this step, the "Analyze Particles" command was used to determine the total number of live and

dead cells in each image. This command works by scanning a binary image until it runs into the edge of an object or particle (e.g. a cell). Once a particle is found, an outline is drawn around it and certain user-specified measurements are calculated and recorded (e.g. pixel area, circularity, mean gray value, etc.). The command then continues scanning the rest of the image, counting and measuring each particle it encounters. Once the command finishes scanning the image, it reports its results in a summary window that gives the total particle count and the specified measurement values. The live and dead counts determined using "Analyze Particles" were stored in an Excel spreadsheet and used to calculate the cell viability (in % live cells to total cells) in each image. Using these calculated percentage values, the percent difference between the value of the non-UV-treated sample and the UV-treated sample in each particular treatment group was determined and used for comparison.

In the other three wells of each 4-well plate, keratinocytes were fixed using Histochoice; and p21 protein and cell nuclei were stained for using Alexa Fluor 488 and DAPI, respectively. After staining, a confocal microscope was used to capture 5 images per well, and each image was saved as a TIFF file. Using ImageJ, the blue (DAPI) channel of these images was thresholded to create a binary image of the cell nuclei. Cell viability was again evaluated using the "Analyze Particles" command, this time by scanning the cell nuclei binary images and measuring the mean cell nucleus area (in pixels^2) per image. During cell death, cell nuclei are known to shrink in size (pyknosis) and later undergo fragmentation (karyorrhexis) (Boya et al. 2005). Thus, it was assumed that significantly smaller means of cell nuclei area in UV-treated keratinocytes compared to those in non-UV-treated keratinocytes positively correlated with cell death. Once the

mean cell nucleus area for each image was measured in ImageJ, the means were stored in an Excel spreadsheet, and the overall means of nucleus area of the 8 different treatment groups were calculated. Using JMP statistical software (SAS Institute Inc., Cary, NC), t-tests (α=0.05) were performed to detect any significant differences between the mean nucleus area of the 8 treatment groups and to determine specifically between which groups a significant difference existed.

The confocal images taken were also used to evaluate nuclear p21 expression. This was done by utilizing the PixelCount program (see Chapter 3.1) to obtain a p21 expression ratio (p21-expressing nuclei/total nuclei) for each image. The five p21 expression ratios obtained from the 5 images taken per well were averaged in Excel to obtain one mean p21 expression ratio per well. JMP software was then used to perform t-tests (α=0.05) to statistically compare the mean p21 expression ratios (n=3) of the 8 treatment groups and to determine the location of any significant difference that existed.

3.3.2 Results and Discussion

The live/dead fluorescent images taken for each treatment group are shown in Figure 3.8. Overall, it was found that, when compared to the 1hr, UV and 10hr, UV treatment groups, the 24hr, UV and 36hr, UV treatment groups resulted in relatively high cell death, with the cell viability being less than 55% in both UV-treated groups (see Figure 3.9). As depicted in Figure 3.9, cell viability (%) for UV-treated keratinocytes (red line) decreases as post-UV incubation period increases from 1hr to 36hrs. This trend was expected because it is known that UV irradiation does not cause immediate cell death under normal circumstances. In fact, reports have shown that UV-induced apoptosis in human keratinocytes occurs between 24 to 48 hours following UV irradiation (Raj et al.

2006). It was initially expected that the non-UV-treated keratinocytes (blue line in Figure 3.9) would follow a similar trend as the UV-treated keratinocytes, since the cells were not given fresh cell culture media at any time post-UV and were expected to undergo cell death through lack of nutrients over time. However, as shown by the blue line in Figure 3.9, it was found that cell viability increased from the 10hr to 24hr treatment groups. This increase could be explained by the non-UV-treated keratinocytes undergoing normal cell proliferation up to 24hrs post-UV, indicating that the cell media was still sufficient for growth at the 24hr time point. It is important to note, however, that the small sample size used for the live/dead stain (n=1) could have also caused the up-and-down pattern in cell viability in the non-UV treatment groups. The percent difference between the cell viabilities of the non-UV-treated and UV-treated group for each incubation period is given in Table 3.1. The 24hr treatment group showed the largest percent difference (46.61%) between the non-UV treatment and UV treatment cell viability values, while the 36hr treatment group showed the second largest percent difference (29.00%). The large percent difference observed in the 24hr treatment group could be explained by the 24hr, non-UV-treated group having relatively high cell viability (87.8%) compared to the other non-UV-treated groups (possibly due to small sample size). Additionally, small sample size was considered to be the reason why the percent difference between cell viabilities of the 10hr, non-UV and UV treatment groups (1.253%) was relatively low.

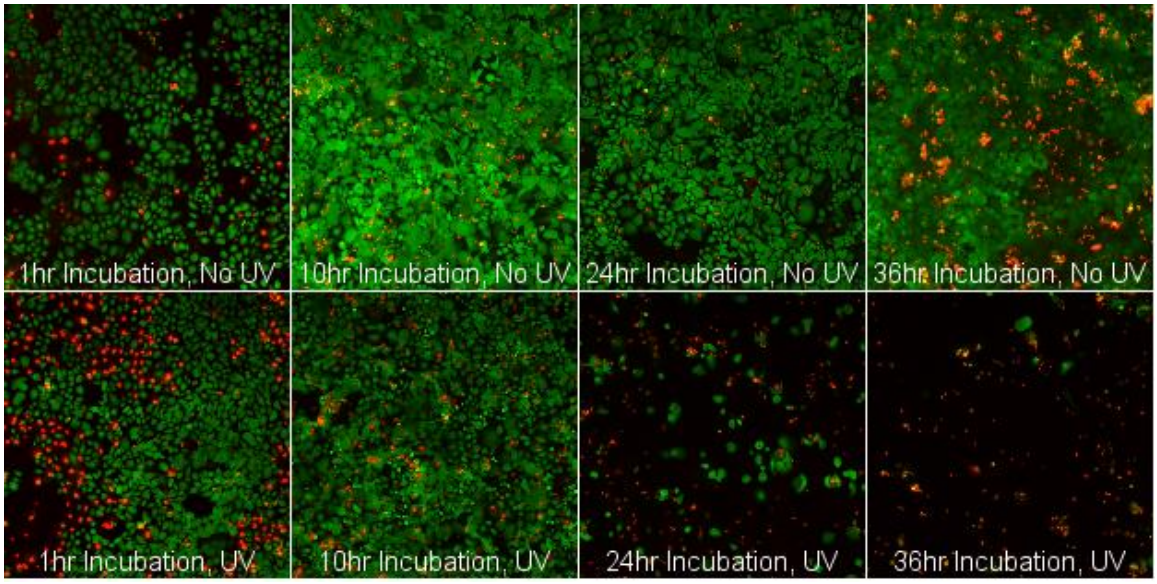

Figure 3.8 Live/dead fluorescent images taken for each treatment group.

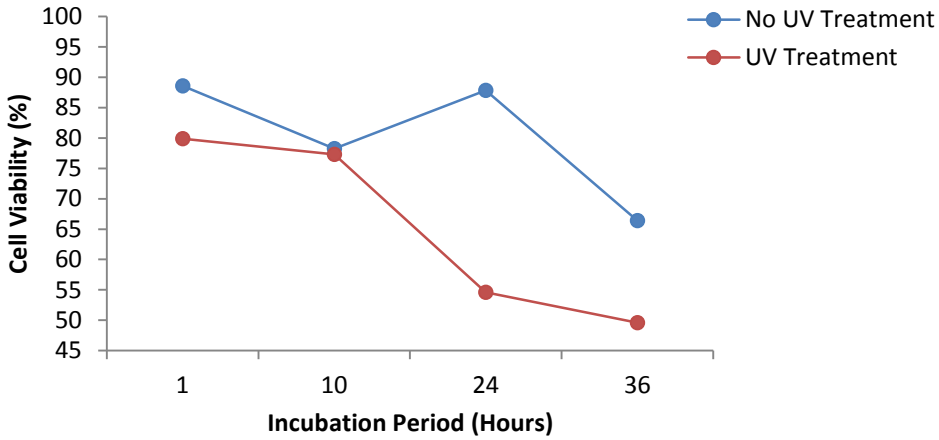

Figure 3.9 Cell viability (%) calculated from live/dead stain images taken immediately after each post-UV incubation period.

Table 3.1 Percent Differences between Cell Viability of Non-UV-Treated and UV-Treated Groups of Similar Incubation Periods

Post-UV Incubation Period (hours)	% Difference Between No UV and UV Treatment
1	10.32
10	1.253
24	46.61
36	29.00

While the live/dead image analysis (n=1) suggested that the percentage of viable cells decreased with increasing incubation period and UV treatment, more data was needed to determine if statistically significant differences existed between the cell viabilities of the 8 treatment groups. Thus, cell viability was also evaluated by comparing the mean cell nucleus area data of which there was a larger sample size (n=3). A box plot showing the distribution of the mean cell nucleus area (in pixels^2) of each treatment group is given in Figure 3.10. Overall, Figure 3.10 shows that the distribution of mean cell nucleus area of each UV-treated group was lower than the corresponding non-UV-treated group. In other words, UV treatment for all four incubation periods caused keratinocyte nuclei to decrease in size compared to non-UV treatment. The mean nucleus area of the UV-treated group for both the 24hr and 36hr incubation periods was roughly half the size of the mean nucleus area of the corresponding non-UV-treated group (nucleus pixel area of 503.8 ± 32.2 versus 855.2 ± 32.2 and 419.0 ± 32.2 versus 795.0 ± 32.2, respectively; via t-tests, $p<0.05$). Additionally, the mean nucleus area of the 24hr, UV treatment group was about 30% smaller than that of the 1hr, UV treatment group (via t-test, $p<0.05$); while the mean nucleus area of the 36hr, UV treatment group was about 40% smaller than those of the 1hr and 10hr, UV treatment groups (via t-tests, $p<0.05$). These results were consistent with the live/dead stain results, since the UV-induced decrease in nucleus area observed in the 24hr and 36hr treatment groups is a main characteristic of programmed cell death.

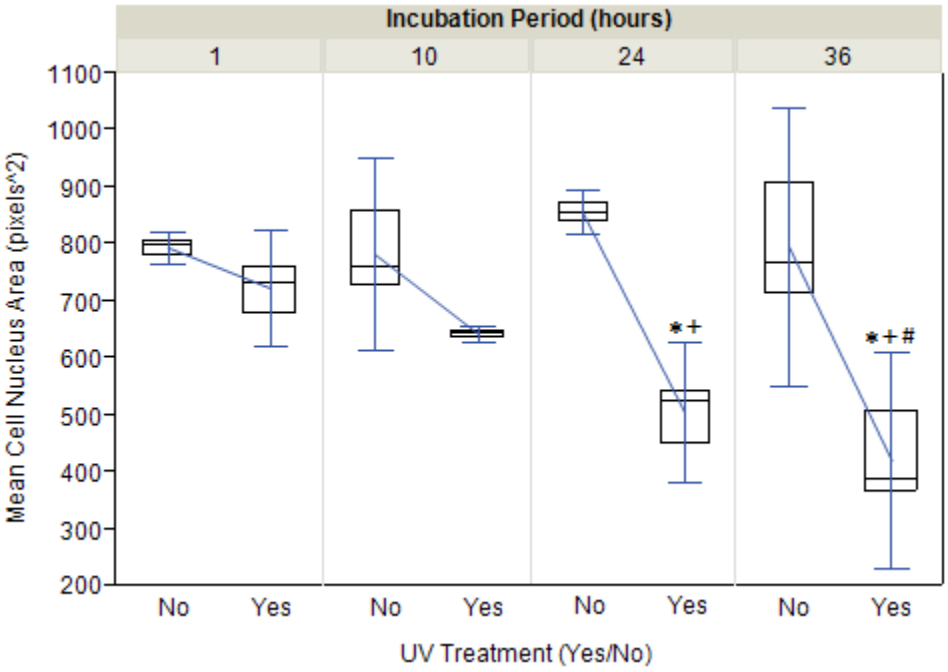

Figure 3.10 Box plot of the distribution of mean cell nucleus area for each group.
* indicates $p<0.05$ via t-test compared with non-UV treatment of same incubation period.
$^{+}$ indicates $p<0.05$ via t-test compared with 1hr, UV treatment group.
$^{\#}$ indicates $p<0.05$ via t-test compared with 10hr, UV treatment group.

As shown in Figure 3.11, the mean p21 expression ratios (number of p21-expressing cells/total number of cells) for the non-UV and UV treatment groups of the 1hr, 10hr, 24hr, and 36hr incubation periods approximately ranged between 0.3 and 0.6. The two mean p21 expression ratios (for non-UV and UV) corresponding to any particular incubation period had very similar values to one another. Consequently, and because of small sample size (n=3), no significant difference was found between the mean p21 expression ratio of any particular UV treatment group and that of the corresponding non-UV treatment group (via t-tests, $p>0.05$). The mean p21 expression ratio was highest in the 24hr, UV treatment group, being nearly twofold greater than that of the 10hr, UV treatment group (p21 expression ratio of 0.591 ± 0.08 versus 0.324 ± 0.08; via t-test, $p<0.05$). Overall, the results for the effect of post-UV incubation period

on UV-induced nuclear p21 expression were inconclusive, since no statistically significant differences were found between non-UV and UV groups.

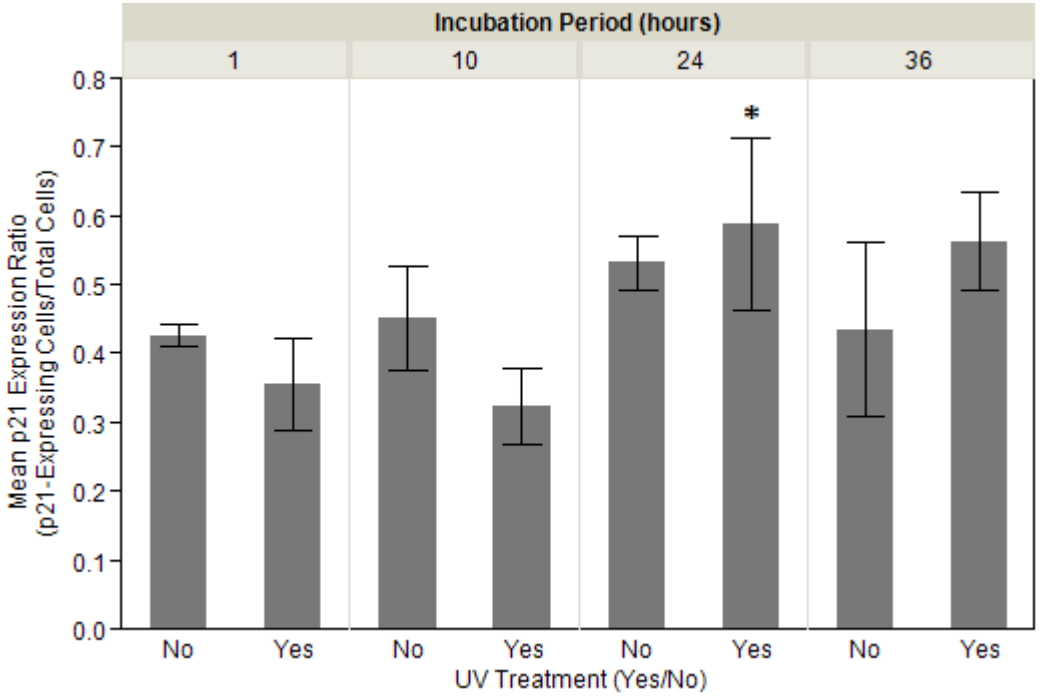

Figure 3.11 Mean p21 expression ratio of each treatment group.
* indicates $p<0.05$ via t-test compared with 10hr, UV treatment group.
Error bars represent 1 standard error from the mean.

Both analyses of cell viability (see Figures 3.9 and 3.10) suggested that the 24hr and 36hr incubation periods resulted in significant cell death in the UV-treated samples. Although the results for p21 expression were inconclusive (see Figure 3.11), the trends in p21 expression were still considered in support of the cell viability results. Of the keratinocyte samples tested, UV-induced nuclear p21 expression was highest at 24hrs post-UV incubation, which was followed closely by the 36hr incubation period. This is consistent with literature reports that UV-induced p21 expression is highest at 24 to 48 hours post-UV in normal human keratinocytes treated with high doses of UVB (Ahmed et al. 1999). Based off the findings that the 24hr, UV treatment group showed the first

signs of significant cell death compared to the non-UV treatment group, and showed the highest mean nuclear p21 expression of all the treatment groups tested, the 24hr time point was considered to be the point at which the keratinocytes had fully reacted to the UV irradiation. Also based off these finding, it was confirmed that the UV dose used ($60mJ/cm^2$) is the minimal erythema dose (MED) for normal human neonatal epidermal keratinocytes and causes severe and irreparable DNA damage. With elevated levels of cell death and nuclear p21 expression, 24hrs was considered to be a reliable time point for observing the UV-induced DNA damage response in normal human epidermal keratinocytes and was selected as the optimal post-UV incubation period to be used in the finalized protocol.

3.4 Determination of UV Dose

3.4.1 Overview

Once the optimal post-UV incubation period was selected, the next goal was to determine the maximum UV dose that could be used on human keratinocytes without causing cell death after the 24 hours of post-UV incubation, and would produce the largest difference in mean nuclear p21 expression between non-UV-treated and UV-treated keratinocytes. Since $60mJ/cm^2$ of UVB radiation followed by a 24hr post-UV incubation period was found to cause significant cell death (see Chapter 3.3), doses lower than $60mJ/cm^2$ were tested. The UV doses tested in this preliminary study were 10, 20, and $40mJ/cm^2$. Three 4-well plates were used and two wells were assigned to each treatment group as depicted in Figure 3.12.

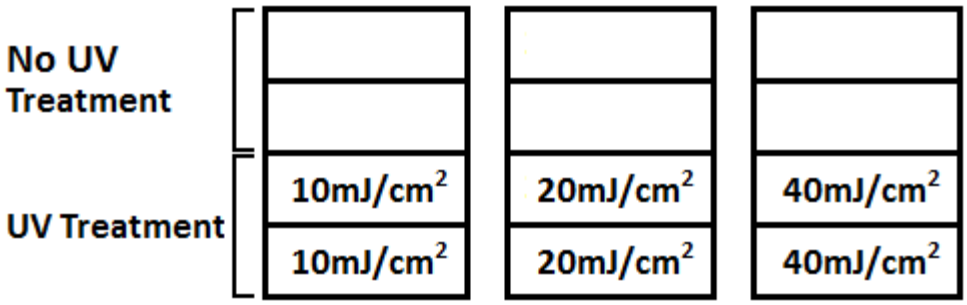

Figure 3.12 Four-well plate setup for the determination of the optimal UV dose.

This experiment was repeated a total of 4 times, giving 4 replicates, with each replicate using the setup in Figure 3.12. In the first replicate, Histochoice was used to fix the cells following the 24hr post-UV incubation period. Afterwards, p21 protein and cell nuclei were immunofluorescently stained (with Alexa Fluor 488 and Hoechst stain, respectively) to study how nuclear p21 expression of human keratinocytes is affected by different doses of UV radiation, 24hrs post-UV. Once all three 4-well plates were stained, a confocal microscope was used to capture 3 images per well and each image was saved as a TIFF file. PixelCount was used to calculate a p21 expression ratio per image and store each ratio value in an Excel spreadsheet. Using Excel, the mean p21 expression ratio was calculated for each well, giving two data points per treatment group (n=2). Afterwards, JMP software was used to perform t-tests (α=0.05) between the mean p21 expression ratios of the different treatment groups to analyze the effects of UV dose on nuclear p21 expression in human keratinocytes.

A second replicate was carried out in attempt to collect additional data necessary for determining any statistically significant differences between treatment groups. However, during the immunostaining procedures of this experiment, 1% Triton X-100 was mistakenly used instead of 0.1% Triton X-100 for cell membrane permeabilization.

Furthermore, poor fluorescence images of p21 expression were obtained, which was attributed to the high concentration of Triton X-100 used. Thus, a third replicate was performed. However, in the immunostaining procedures of this experiment, expired Triton X-100 was accidentally used. No p21 fluorescence was found in any of the samples, which was attributed to the expired Triton X-100.

Before performing a fourth replicate, research was done on standard protocols and reagents for immunocytochemistry to avoid additional errors in obtaining sufficient p21 fluorescence. In a general fixation protocol written by Molecular Probes, it was found that high-quality formaldehyde is important for good results (Molecular Probes Inc., 2005). Also, the protocol specifically recommended using 3.7% formaldehyde diluted (in buffer) from 16% ultrapure formaldehyde, methanol free. Previously, however, Histochoice was used as the fixative reagent. Therefore, in the fourth replicate of this preliminary study, both 3.7% formaldehyde and Histochoice were used for comparison. The comparison of these two fixative reagents is discussed in more detail in Chapter 3.5.

Ultimately, the samples fixed with 3.7% formaldehyde showed significantly greater nuclear p21 fluorescence compared with the samples fixed with Histochoice. Thus, two confocal images were taken for each treatment group of the formaldehyde-fixed samples and used for UV dose analysis. Because of the high nuclear p21 fluorescence, the IntenseCount program was used to analyze these images. This program was used to calculate the mean intensity of nuclear p21 fluorescence for every image and store each intensity value in an Excel spreadsheet. Apoptosis analysis was also performed on the formaldehyde-fixed sample images by noting any signs of nuclear fragmentation in the Hoechst (blue channel) images. The number of fragmented nuclei and total number

of nuclei per image were manually determined and used to estimate the average percentage of apoptotic nuclei per treatment group. Average percentages less than 10% were considered acceptable.

In order to combine the data of the fourth replicate with the first replicate experiment results, the confocal images of the first replicate were re-analyzed using IntenseCount. Because formaldehyde was used as the fixative in the fourth replicate, however, the resulting mean p21 intensity values were, overall, found to be significantly higher than those of the first replicate (which used Histochoice). To adjust for the differences in scale, both data sets were separately normalized from 0 to 1 before being combined for statistical analysis. Once the data sets were normalized and combined, JMP was used to perform t-tests (α=0.05) to statistically compare the mean nuclear p21 pixel intensities of the different treatment groups.

Further analysis was performed to evaluate the correlation between nuclear p21 pixel area and nuclear p21 pixel intensity (i.e. PixelCount results versus IntenseCount results), and to determine how effective each program was for image analysis. To do this, the confocal images of the fourth replicate were once again analyzed, this time using PixelCount to determine p21 expression ratios for each image. Once this was done, the PixelCount data of the fourth replicate were combined with the PixelCount data of the first replicate, and these combined data were normalized from 0 to 1. In JMP, t-tests (α=0.05) were done on the combined PixelCount data to re-evaluate whether significant differences existed between the mean p21 expression ratios of the different treatment groups. Additionally, a simple linear regression (α=0.05) was performed using the

combined IntenseCount results as the response variable and the combined PixelCount results as the explanatory variable.

3.4.2 Results and Discussion

No significant difference was found between any of the treatment groups in the first replicate experiment (via t-tests, $p>0.05$). As shown in Figure 3.13, mean p21 expression ratio was highest for the 40mJ/cm^2, UV treatment group, with the ratio for the 10mJ/cm^2, UV treatment group being second highest and only slightly lower. The mean p21 expression ratios of the 10 and 40mJ/cm^2 treatment groups were higher in the UV-irradiated samples compared to the non-UV-irradiated samples. While it was expected that the 20mJ/cm^2 treatment group would follow a similar trend, the mean p21 expression ratio of this group was found to decrease from the non-UV-irradiated group to the UV-irradiated group. It was unknown why this trend occurred exclusively in the 20mJ/cm^2 treatment group. However, a possible explanation was that the sample size used (n=2) was too small to accurately represent the population, meaning that the observed trend would not have been true for larger sample sizes. Another possible explanation was that the 302nm UV dose of 20mJ/cm^2 caused UV-induced p21 degradation to allow for DNA repair. This explanation is supported by reports in which certain doses of UV irradiation caused p21 degradation in human keratinocytes, where p21 was shown to inhibit DNA repair through its interactions with PCNA (Mansilla et al. 2013).

Representative images of Hoechst-stained nuclei from the 10, 20, and 40mJ/cm^2, UV-treated groups of the fourth replicate experiment are shown in Figure 3.14. Overall, signs of nuclei fragmentation (apoptosis) were observed in the 40mJ/cm^2, UV treatment group, while only round and normal-looking nuclei (0% apoptotic nuclei) were observed

in the other treatment groups. The extent of nuclei fragmentation observed in the 40mJ/cm^2, UV group, however, was considered to be acceptable, since the average percentage of apoptotic nuclei was estimated to be 9.964%, which is less than 10%.

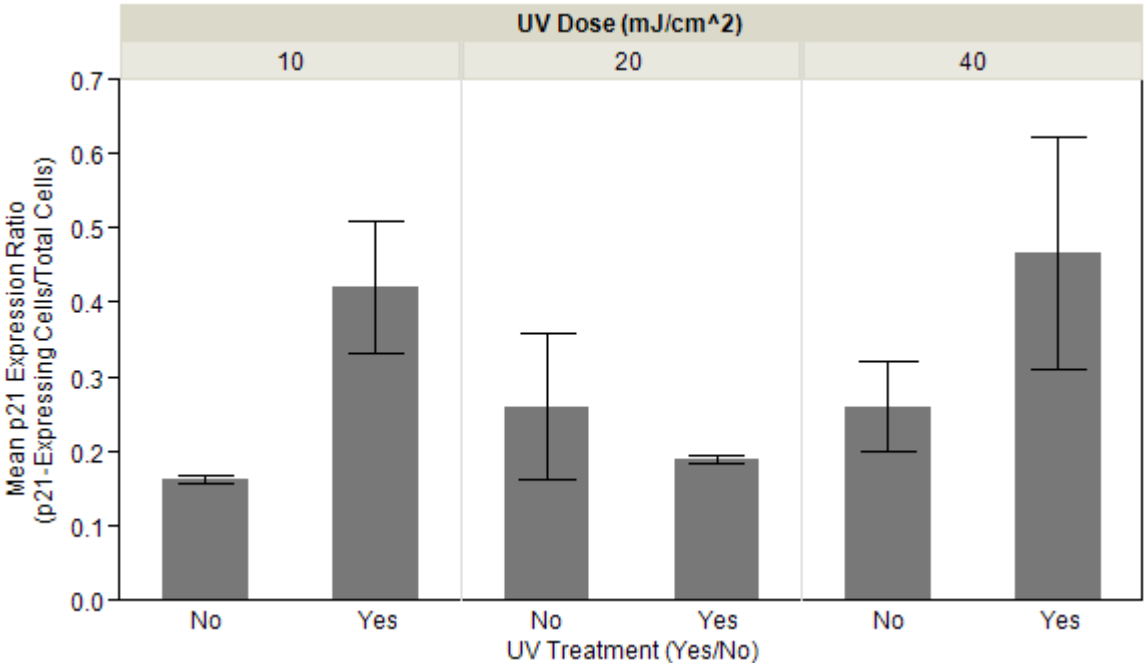

Figure 3.13 Mean p21 expression ratios from first replicate experiment for UV dose determination. Error bars represent 1 standard error from the mean.

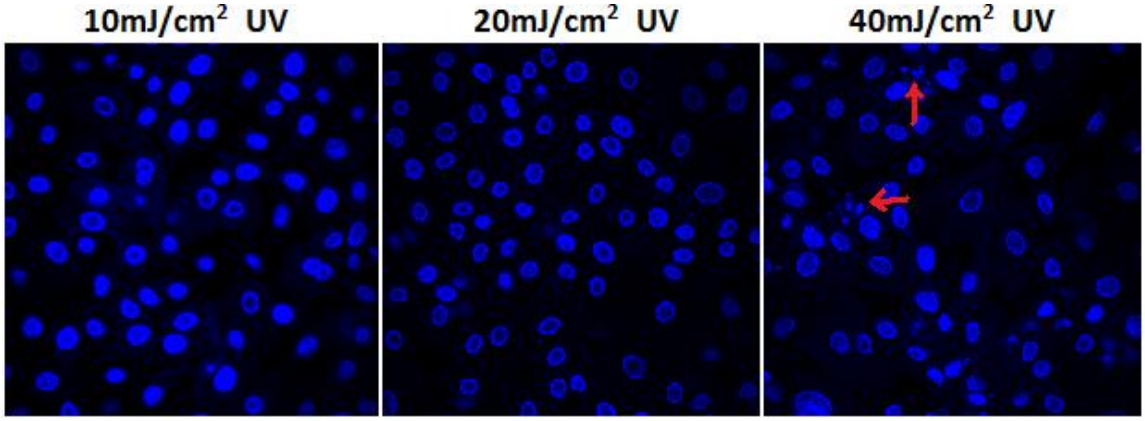

Figure 3.14 Representative confocal images of Hoechst-stained nuclei of the different UV dose groups (with UV treatment). Red arrows indicate presumed nuclei fragmentation.

As shown in Figure 3.15A, the overall mean p21 expression ratio of the formaldehyde-fixed samples of the fourth replicate was nearly equivalent to that of the Histochoice-fixed samples of the first replicate. Since mean p21 expression ratio is related to nuclear p21 pixel area, Figure 3.15A suggests that whether a sample is fixed with Histochoice or formaldehyde does not affect the area of nuclear p21 per nuclei as measured by PixelCount. However, a larger sample size is needed to confirm this observation. Figure 3.15B shows that the overall mean nuclear p21 intensity of formaldehyde-fixed cells of the fourth replicate was nearly twofold greater than that of Histochoice-fixed cells of the first replicate (mean p21 signal intensity of 12.3 ± 3.44 versus 5.37 ± 1.27; via t-test, $p<0.05$). This result was expected, since, through visual inspection of the images, it was clear that the formaldehyde fixed samples showed much higher nuclear p21 intensities than the Histochoice fixed samples. Thus, it was necessary to normalize the intensity results of the first and fourth replicates before combining the two data sets.

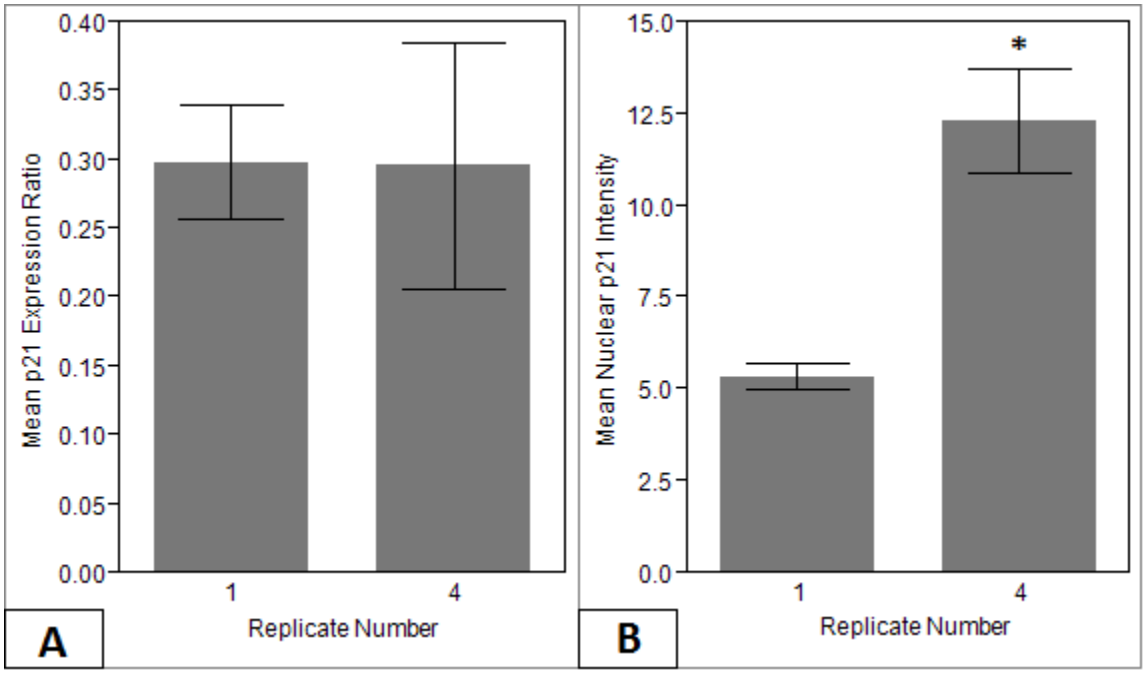

Figure 3.15 Overall mean values of first and fourth replicates for UV dose determination. A) Mean p21 expression ratios of first and fourth replicates, obtained from PixelCount analysis. B) Mean p21 pixel intensities of first and fourth replicates, obtained from IntenseCount analysis. * indicates $p<0.05$ via t-test compared with the first replicate. Error bars represent 1 standard error from the mean.

Figure 3.16 shows a bar chart of the combined data sets of the first and fourth replicate experiments, for both the normalized PixelCount data (light gray bars) and the normalized IntenseCount data (dark gray bars). The normalized PixelCount data in Figure 3.16 was obtained from combining the mean p21 expression ratios of the first and fourth replicates, and was compared with the initial PixelCount data for just the first replicate that is depicted in Figure 3.13. In comparing Figure 3.16 to Figure 3.13, it was found that combining the two PixelCount data sets did not alter the trends initially observed in Figure 3.13. For both bar chart figures, the PixelCount data showed nuclear p21 expression to increase from the non-UV to UV group of the 10 and 40mJ/cm^2 UV doses, and decrease from the non-UV to UV group of the 20mJ/cm^2 UV dose. Combining the two PixelCount data sets did affect the statistical analysis results, however. In particular,

the combined PixelCount data showed that the nuclear p21 expression value of both the 10 and 40mJ/cm^2, UV-treated groups was significantly greater than that of the non-UV-treated group of the same UV dose (via t-tests, $p<0.05$), and significantly greater than that of the 20mJ/cm^2, UV-treated group (via t-tests, $p<0.05$).

The dark gray bars in Figure 3.16 represent the normalized and combined IntenseCount data of mean nuclear p21 intensity. Nuclear p21 intensity was considered to be directly related to nuclear p21 expression. Thus, like the PixelCount data, the combined IntenseCount data showed nuclear p21 expression to be higher in the UV treatment group compared to the non-UV treatment group for both the 10 and 40mJ/cm^2 UV doses, with the opposite trend shown for the 20mJ/cm^2 UV dose. Unlike the PixelCount data, however, the IntenseCount data showed that only the nuclear p21 expression value of the 40mJ/cm^2, UV-treated group was significantly greater than that of the non-UV-treated group of the same UV dose (via t-test, $p<0.05$), and significantly greater than that of the 20mJ/cm^2, UV-treated group (via t-test, $p<0.05$). These results indicate that nuclear p21 expression ratio measured by PixelCount is not completely correlated with mean nuclear p21 intensity measured by IntenseCount. For example, in the 10mJ/cm^2 treatment groups, the normalized nuclear p21 expression ratio was significantly larger in the UV group compared to the non-UV group (two light gray bars furthest to the left in Figure 3.16); however, the normalized mean nuclear p21 intensity values of the two 10mJ/cm^2 treatment groups showed no significant difference (two dark gray bars furthest to the left in Figure 3.16). Furthermore, in the 20mJ/cm^2 treatment groups, the nuclear p21 expression ratio showed a bigger decrease from the non-UV group to the UV group compared to the mean nuclear p21 intensity, which showed only a

slight decrease. These results were expected because PixelCount and IntenseCount measure two fundamentally different things. While PixelCount was used to calculate the ratio of nuclei containing greater than 2% green pixels (p21 fluorescence) to the total number of nuclei per image, IntenseCount was used to calculate the mean intensity for all nuclear p21 pixels within an image.

Nevertheless, a positive linear association was found between the IntenseCount data and PixelCount data (via simple linear regression; p-value<0.05). A scatterplot of the normalized IntenseCount data versus the normalized PixelCount data obtained from the JMP regression output is given in Figure 3.17. This scatterplot shows the calculated regression line going through the middle of the data points with a positive slope. An R-squared value of 65% was considered to be a moderately good fit, and indicated that about 65% of the variation in the normalized IntenseCount data is explained by the regression using the normalized PixelCount data as a predictor variable. The positive correlation found between the IntenseCount and PixelCount data suggests that an increase in number of nuclei containing greater than 2% green pixels is associated with an increase in mean nuclear p21 intensity. This correlation showed that both PixelCount and IntenseCount give consistent and reliable measurements of nuclear p21 expression.

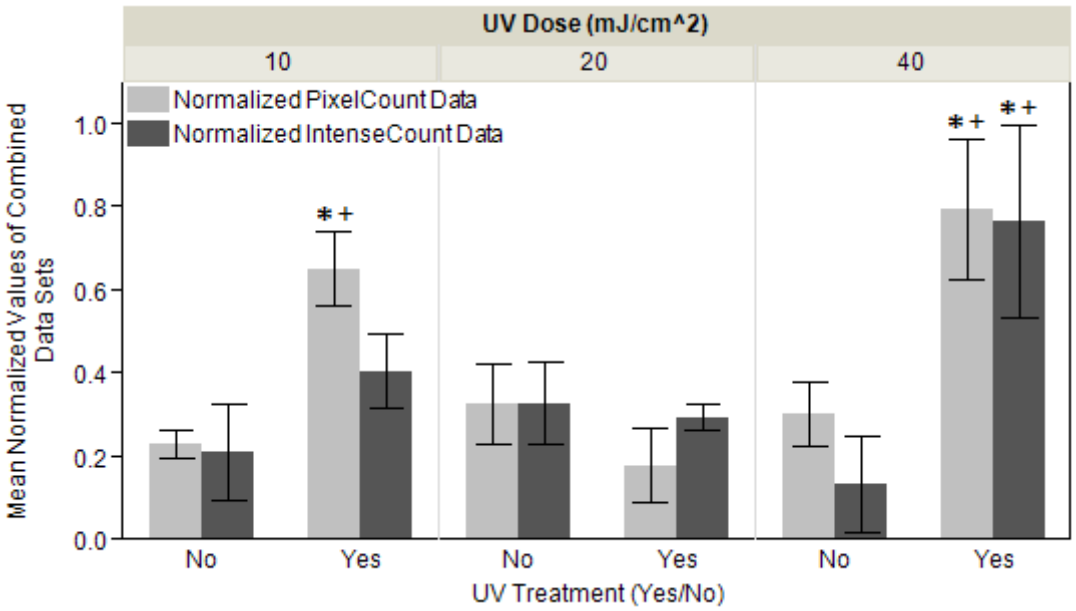

Figure 3.16 Mean p21 intensities from combined data sets of first and fourth replicates. * indicates $p<0.05$ via t-test compared with no UV group of same UV dose and data type. $^{+}$ indicates $p<0.05$ via t-test compared with 20mJ/cm^2, UV group of same data type. Error bars represent 1 standard error from the mean.

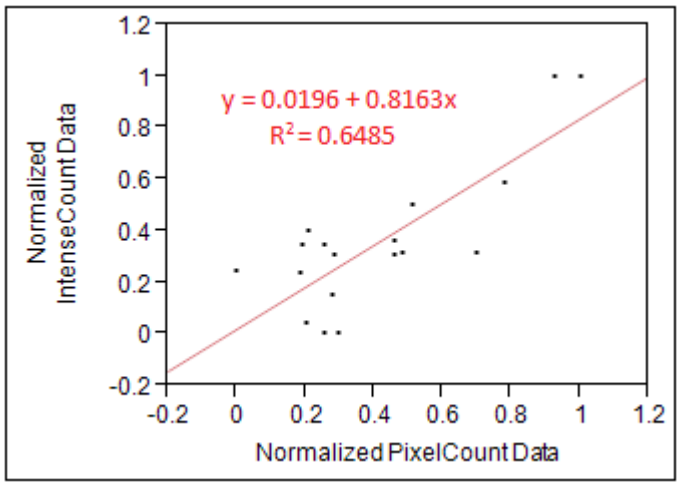

Figure 3.17 Scatter plot of normalized IntenseCount data versus normalized PixelCount data. Equation of linear regression line and R-squared value are displayed in red.

All UV irradiation doses were expected to cause an increase in nuclear p21 expression 24hrs post-UV, since p21 overexpression is known to cause cell cycle arrest in response to various cellular stressors (Hattinger et al. 2002). However, this was found to only be true for the 10 and 40mJ/cm^2 UV doses. While this may have been due to small

sample size, it is also possible that the 302nm UV dose of 20mJ/cm^2 caused degradation of p21 to remove the inhibitory effect of p21-PCNA interactions against DNA repair, since p21 expression is known to be dependent on UV dose (Mansilla et al. 2013). Overall, because 40mJ/cm^2 was the highest UV dose that produced a significant difference between the mean p21 expression values of the non-UV-treated and UV-treated groups, and caused relatively little cell death after the 24 hours of post-UV incubation, the UV dose selected for use in the finalized protocol was 40mJ/cm^2.

3.5 Comparison of Fixative Reagents

3.5.1 Overview

Both Histochoice and formaldehyde fix tissue and cells by creating covalent bonds between soluble proteins to prevent them from degradation; however, Histochoice is known to form much weaker bonds than formaldehyde (Vince et al. 1997). This may cause Histochoice to be less effective at fixing certain types of tissues or cells compared to formaldehyde. Thus, the comparison of these two fixative reagents (formaldehyde and Histochoice) was carried out simultaneously with the fourth replicate of the UV dose determination study described in Chapter 3.4. A schematic of the 4-well plate setup is given in Figure 3.18.

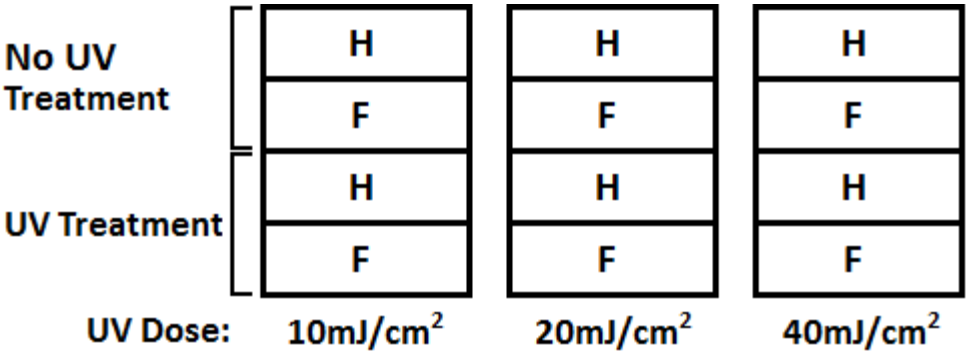

Figure 3.18 Four-well plate setup for the comparison of fixative reagents. Abbreviations: H (Histochoice), F (3.7% formaldehyde).

After 24 hours of post-UV incubation, cell culture wells were either fixed with Histochoice for 30 minutes or 3.7% formaldehyde (diluted from 16% formaldehyde [Cat. #15710, Electron Microscopy Sciences, Hatfield, PA] using PBS) for 15 minutes, both at room temperature. Both treatment groups were then immunostained in the same manner, with p21 and cell nuclei labeled with Alexa Fluor 488 and Hoechst stain, respectively. Using a confocal microscope, two images were taken per well and stored as TIFF files. Images were later visually evaluated for their quality of nuclear p21 fluorescence. No statistical analysis was performed.

3.5.2 Results and Discussion

Keratinocyte samples fixed with formaldehyde produced significantly greater nuclear p21 fluorescence compared to samples fixed with Histochoice. As shown in the representative confocal images in Figure 3.19, p21 fluorescence appeared as green specks mostly localized within keratinocyte nuclei (blue ovals) for both treatment groups. However, the nuclear p21 fluorescence of the formaldehyde-fixed samples had a higher frequency, was clearly visible in the majority of nuclei, and covered significantly greater pixel areas within nuclei compared to that of the Histochoice-fixed samples. Through the visual evaluation of p21 fluorescence of the different treatment groups, it was evident that the quality of nuclear p21 fluorescence of the formaldehyde-fixed samples was superior to that of the Histochoice-fixed samples. Not only did the formaldehyde-fixed sample images show greater nuclear p21 fluorescence, but they also showed higher consistency and robustness in p21 fluorescence across all images compared to the Histochoice-fixed sample images. These results indicate that formaldehyde, not Histochoice, is an effective fixative for detecting p21 protein expression 24hrs post-UV irradiation in human

keratinocytes. In addition, because formaldehyde-fixed samples showed remarkably higher amounts of nuclear p21 fluorescence, the IntenseCount program was written to take into account nuclear p21 pixel intensity, as opposed to nuclear p21 pixel area.

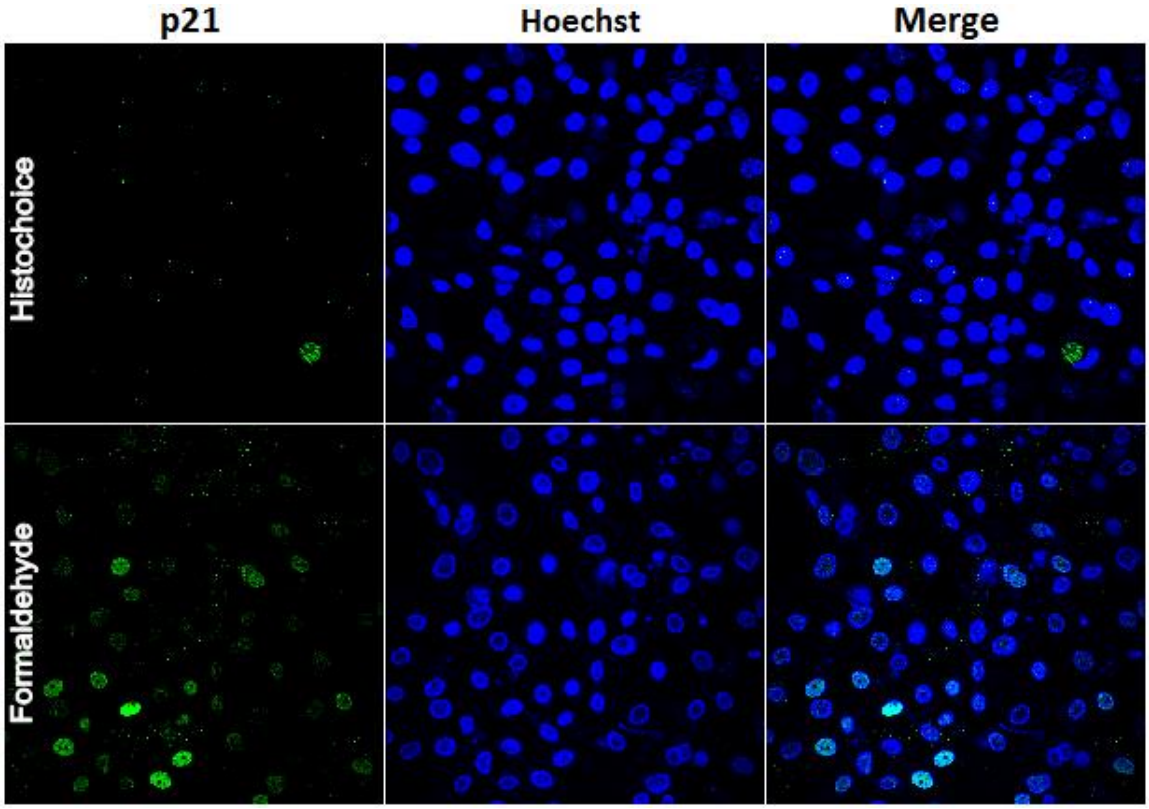

Figure 3.19 Representative confocal images of p21 fluorescence and cell nuclei of keratinocytes treated with 40mJ/cm^2 UV radiation and fixed with either formaldehyde or Histochoice.

After performing this preliminary study, it was realized that using Histochoice for cell fixation is inadequate for p21 detection and causes low nuclear p21 fluorescence intensity in human keratinocytes. It was initially assumed that the minuscule amounts of nuclear p21 fluorescence found in Histochoice-fixed samples (see Figure 3.19) were reliable and sufficient for statistical analysis. However, after seeing the significantly higher nuclear p21 fluorescence and consistency of formaldehyde-fixed samples compared to that of Histochoice-fixed samples, the p21 fluorescence values measured in

the previous experiments that used Histochoice was considered to be unreliable and possibly unsuitable for statistical analysis. Although the earlier experiments should have been redone using formaldehyde to obtain more definitive results, they were not repeated due to limited time, and the previous results were still trusted for use in the finalized protocol. In conclusion, formaldehyde was superior to Histochoice in fixing human keratinocytes so that nuclear p21 protein at the time of fixation was preserved. Thus, formaldehyde was selected to be used in the finalized protocol.

3.6 Determination of Primary and Secondary Antibody Concentrations

3.6.1 Overview

Different concentrations of primary and secondary antibodies were tested to see which concentrations (diluted in PBS) gave the highest p21 signal intensities with the least amount of background staining. For the primary anti-p21 antibody (ab18209, Abcam, Cambridge, MA), the dilutions tested were 1/400 and 1/1000, giving concentrations of 2.5μg/mL and 1.0μg/mL, respectively. These concentrations were chosen since a previous pilot study was done using a 1/1000 dilution (recommended by the manufacturer) of primary anti-p21 antibody and resulted in insignificant p21 fluorescence. Therefore, in this preliminary study, a 1/400 dilution of primary antibody was tested along with a 1/1000 dilution to see if the insignificant p21 fluorescence found in the previous pilot study was due to the primary antibody concentration being too low. For the secondary antibody, Alexa Fluor 488 (A11008, Life Technologies, Grand Island, NY), the following dilutions were tested: 1/200, 1/400, 1/600, 1/800. These dilutions corresponded to concentrations of 5.0μg/mL, 2.5μg/mL, 1.7μg/mL, and 1.0μg/mL, respectively. Hoechst stain (5μg/mL, diluted in PBS) was also used to stain keratinocyte

nuclei. A schematic of the 4-well plate setup used is shown in Figure 3.20. A UV dose of 40mJ/cm^2 was used for UV treatment. After 24 hours of post-UV incubation, cells were fixed with 3.7% formaldehyde and the appropriate immunostaining reagents were applied. After staining the cells, confocal microscopy was used to obtain two images per well. Images were saved as TIFF files for further analysis. The images were quantitatively analyzed using IntenseCount, and t-tests (α=0.05) were performed on the mean intensity data for the two primary antibody dilutions, the 4 secondary antibody dilutions, and the non-UV-treated samples and UV-treated samples. These results were used to determine the optimal primary and secondary antibody concentrations that would give the most nuclear p21 expression.

	2°: 1/200	2°: 1/200	2°: 1/200	2°: 1/200
	2°: 1/400	2°: 1/400	2°: 1/400	2°: 1/400
	2°: 1/600	2°: 1/600	2°: 1/600	2°: 1/600
	2°: 1/800	2°: 1/800	2°: 1/800	2°: 1/800
1° Antibody Dilution:	1/400	1/1000	1/400	1/1000
UV Treatment (Yes/No):	No	No	Yes	Yes

Figure 3.20 Four-well plate setup for the determination of optimal primary (1°) and secondary (2°) antibody concentrations.

3.6.2 Results and Discussion

The mean nuclear p21 intensity values calculated for the primary and secondary antibody dilutions are depicted in the bar graphs in Figure 3.21. As shown in Figure 3.21A, the 1/400 primary antibody dilution gave a higher mean p21 intensity, which was

nearly threefold greater than that of the 1/1000 primary antibody dilution (nuclear p21 intensity of 19.96 ± 2.43 versus 6.744 ± 2.8; via t-test, $p<0.05$). As shown in Figure 3.21B, the mean nuclear p21 intensities of the secondary antibody dilutions ranged between about 11-17 (grayscale units; 0-255). No significant differences were found between the mean intensity values of the secondary antibody dilution groups (via t-tests, $p>0.05$), which was most likely due to the small sample size used (n=4 for all t-tests between secondary antibody dilutions) and the fact that only two images were taken per well. For example, it is possible that the two images taken per well did not accurately represent the p21 fluorescence throughout the entire well.

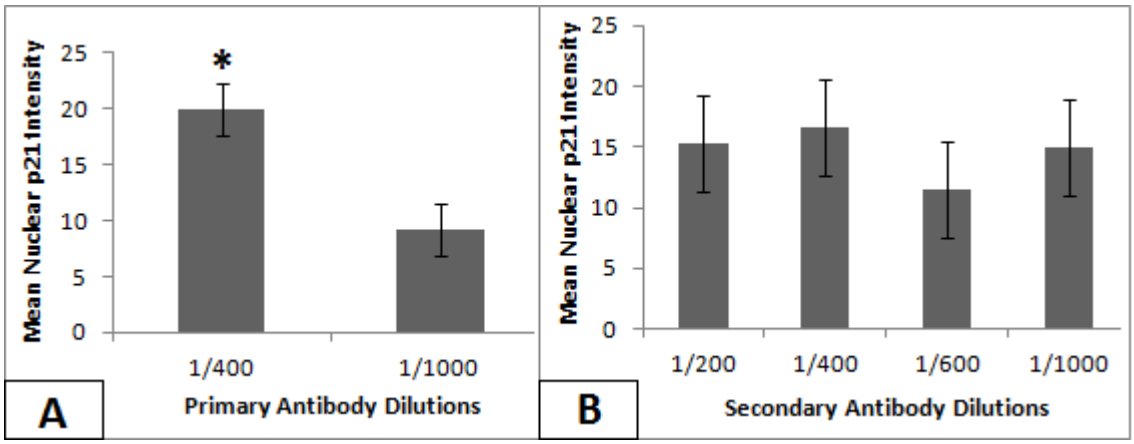

Figure 3.21 Mean nuclear p21 intensities for the tested antibody dilutions. A) Primary antibody dilutions tested. B) Secondary antibody dilutions tested.
* indicates $p< 0.05$ via t-test compared with 1/1000 primary antibody dilution.
Error bars represent 1 standard error from the mean.

There was also no significant difference found between the mean nuclear p21 intensities of the non-UV-treated samples and UV-treated samples (via t-test, $p>0.05$), with the mean p21 intensity and standard deviation of the non-UV-treated and UV-treated groups being 14.33 ± 10.1 and 15.97 ± 9.75, respectively. This was attributed to the small sample size used (n=8 for the number of wells assigned to each UV treatment group).

Thus, more data is needed to show a statistically significant difference between the two UV treatment groups, as well as between the means of the secondary antibody dilution groups. Due to limited time, however, this study was not repeated to obtain additional data; and it was assumed to be sufficient to select the optimal primary and secondary antibody concentrations based on the highest mean nuclear p21 intensity values and objective observations of the fluorescence images. Overall, the primary antibody dilution of 1/400 showed the highest mean nuclear p21 intensity. Although no significant differences were found between the mean p21 intensities of the different secondary antibody dilutions tested, the 1/400 secondary antibody dilution did give the highest mean nuclear p21 intensity and showed more consistent nuclear p21 fluorescence throughout the images captured compared to the other dilutions. Therefore, corresponding to the 1/400 dilutions, the concentrations selected to be used for the finalized protocol were 2.5μg/mL for the primary and 2.5μg/mL for the secondary antibody solution. Representative images of the keratinocyte samples stained using these selected antibody concentrations are shown in Figure 3.22.

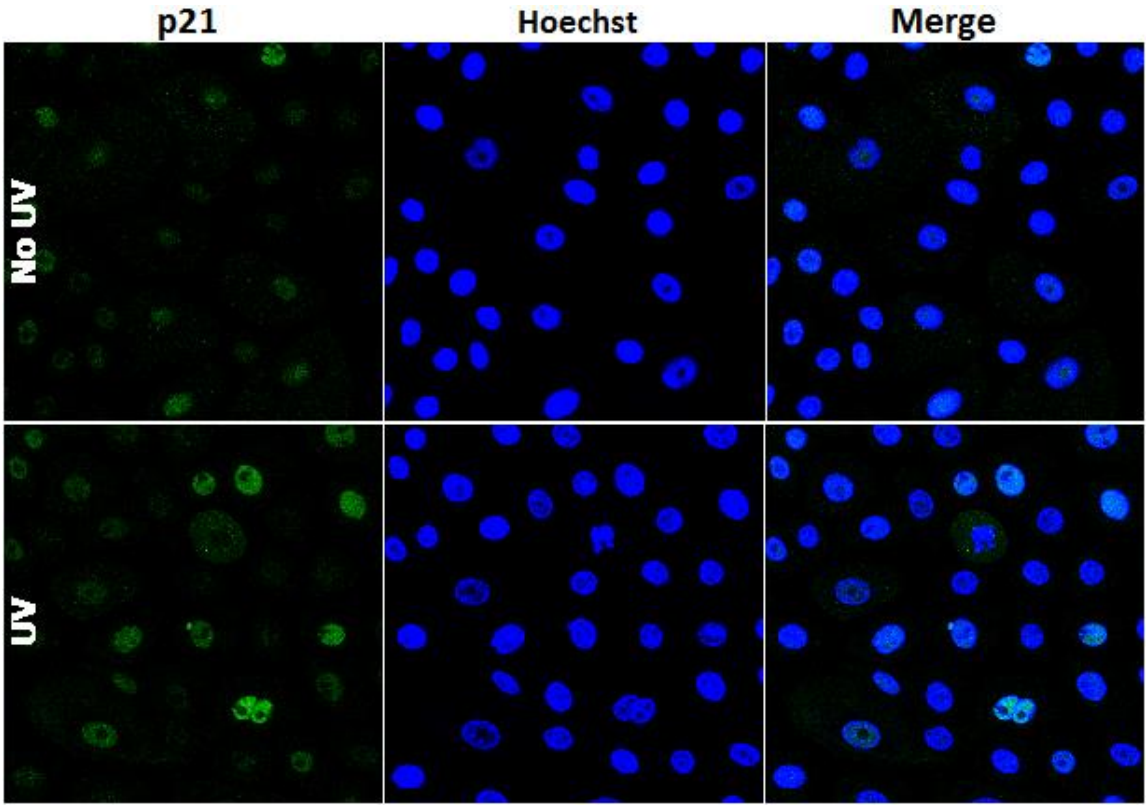

Figure 3.22 Representative images of keratinocyte samples stained with the optimal concentrations of primary and secondary antibody (both 2.5µg/mL), and Hoechst stain.

3.7 Determination of Bovine Milk Sphingomyelin Concentration

3.7.1 Overview

Several concentrations of bovine milk sphingomyelin (SM) dissolved in keratinocyte culture media were studied for their effectiveness in SM uptake by keratinocytes and for their protective effects against UV photodamage. In previous research, a 1.0% (w/v) SM solution was used to treat epidermal tissue constructs for the evaluation of SM's UV-protective effects in a human skin equivalent model (Achay, 2011). However, this concentration was thought to be too high for human keratinocyte culture, and that such a high concentration might result in excessive SM not absorbed by the cells and instead left in the media. Excessive SM was hypothesized to cause cell toxicity and possibly an undesirable UV-shielding effect. Therefore, the following SM

weight-by-volume percentages were tested in human keratinocyte cultures: 0.1%, 0.5%, and 1.0%. A schematic of the 4-well plate setup is shown in Figure 3.23.

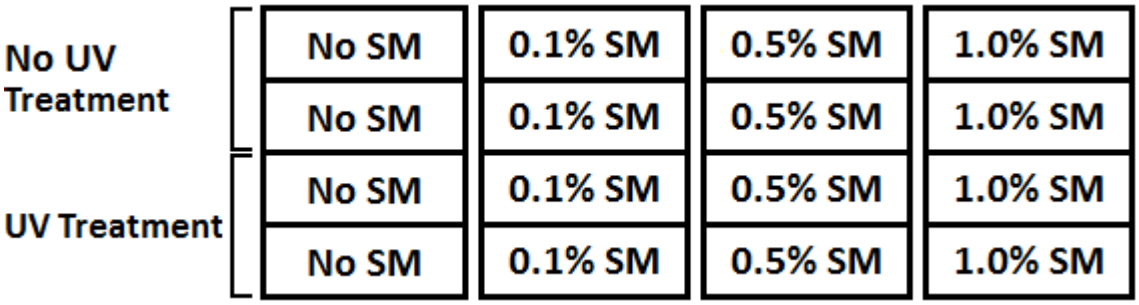

Figure 3.23 Four-well plate setup for the determination of the optimal bovine milk sphingomyelin (SM) concentration (w/v %).

All plates were incubated for 24 hours in the appropriate SM media solution. The plate assigned with no SM treatment (control plate) was given fresh keratinocyte growth medium. After 24 hours of incubation, the media was aspirated out and all wells were rinsed twice with fresh keratinocyte growth media. After rinsing, the general appearance of each cell monolayer was qualitatively analyzed by noting any differences in color or morphology between the different samples. Each well was then given 0.5mL of fresh keratinocyte growth media, and the wells assigned to UV treatment were exposed to 40mJ/cm^2 of UVB radiation. All samples were then incubated for an additional 24 hours prior to fixation with 3.7% formaldehyde. Following cell fixation, immunostaining of p21 protein and cell nuclei was performed. Once staining was complete, three confocal images were take for each well on each 4-well plate and saved as TIFF files. The IntenseCount program was then used to analyze the confocal images. After running IntenseCount and obtaining the mean nuclear p21 intensity values, t-tests (α=0.05) were performed using JMP to statistically compare the mean p21 intensity values of the different treatment groups and to determine where significant differences occurred.

3.7.2 Results and Discussion

A bar chart of the mean nuclear p21 intensity values for the treatment groups for each SM concentration is given in Figure 3.24. In this bar chart, it is shown that the highest mean p21 intensity value occurred in the 1.0% SM, UV treatment group, and the lowest mean p21 intensity value occurred in the 0.0% SM, non-UV treatment group. This result was expected because high SM concentration and UV treatment was likely to cause cellular stress; and p21 expression is known to increase in response to cellular stress to induce cell cycle arrest (Hattinger et al. 2002).

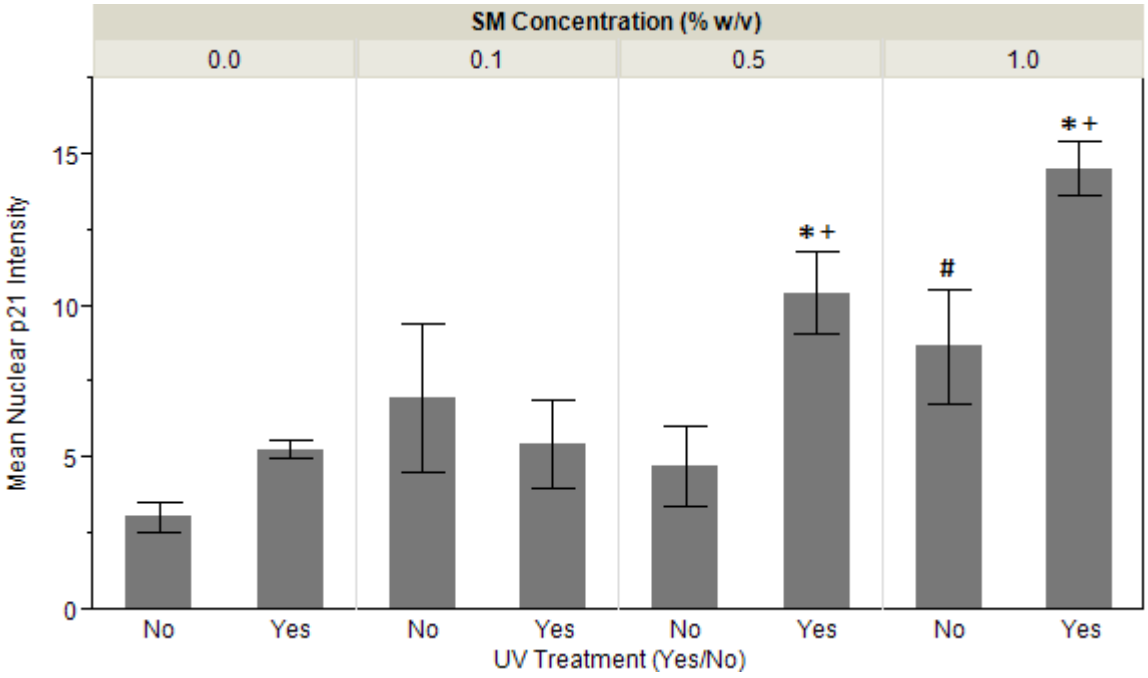

Figure 3.24 Mean p21 intensity for the determination of optimal SM concentration.
* indicates $p<0.05$ via t-test compared with no UV group of same SM concentration.
$^{+}$ indicates $p<0.05$ via t-test compared with 0.0% SM, UV and 0.1% SM, UV groups.
# indicates $p<0.05$ via t-test compared with 0.0% SM, no UV group.
Error bars represent 1 standard error from the mean.

Both the 0.5% and 1.0% SM concentrations of the UV-treated groups produced significantly greater means for nuclear p21 intensity compared with the non-UV-treated group of the corresponding SM concentration; and also compared with the 0% and 0.1%

SM, UV-treated groups (via t-tests, $p<0.05$). These results suggested that the 0.5% and 1.0% SM concentrations did not protect the keratinocytes from UV-induced DNA damage, since nuclear p21 significantly increased in response to UV irradiation in the samples treated with 0.5% and 1.0% SM. In addition, the 1.0% SM concentration caused a significant increase in mean nuclear p21 intensity compared with no SM treatment in non-UV-treated keratinocytes (via t-test, $p<0.05$). Overall, these results led to the conclusion that the 0.5% and 1.0% SM concentrations caused p21 levels to rise after 24 hours of post-UV incubation in UV-treated keratinocytes, while the 0.1% SM concentration did not. The rise in p21 levels was considered to be due to the 0.5% and 1.0% SM concentrations causing a toxic effect on the UV-treated keratinocytes, which could have lead to increased p21-induced cell cycle arrest. However, the exact mechanisms behind this conclusion remained uncertain.

The qualitative analysis performed after the rinse step following the 24hr incubation of keratinocytes in SM solution showed that wells treated with 0.5% or 1.0% SM had a different color and morphology than the control wells and wells treated with 0.1% SM. In all wells treated with either 0.5% or 1.0% SM solution, the keratinocyte monolayer appeared to be covered with a light, cream-colored film visible by the human eye. In some areas, the film appeared to be folded over as if agitation had caused it to separate from the cell monolayer. The control wells and wells treated with 0.1% SM solution had similar color and morphology, with no visible signs of an outer cream-colored film layer.

These results implied that the 0.5% and 1.0% SM concentrations were most likely too high for the intended application. While 0.5% and 1.0% SM were considered to cause

a toxic effect on UV-treated keratinocytes and were found to leave a cream-colored film on the keratinocyte monolayers after SM treatment, no adverse results were found in the 0.1% SM treatment groups. Thus, 0.1% SM was selected as the optimal SM concentration to be used in the finalized protocol.

3.8 Comparison of Blocking Reagents

3.8.1 Overview

The blocking reagent used throughout the majority of the experimental studies performed was a product called Image-iT FX Signal Enhancer (I36933, Life Technologies, Grand Island, NY). This product was initially selected for its ease-of-use, compatibility with the p21 immunostaining protocol, and its ability to effectively eliminate nonspecific fluorescence. However, towards the end of the experimental studies, when the supply of Image-iT FX was low and a replacement needed to be purchased, the concern arose that readily-available donkey serum could be a more cost effective blocking reagent. In fact, the cost of using Image-iT FX (I36933, Life Technologies, Grand Island, NY) was about $8.00 per 4-well plate, while the cost of using donkey serum (sc-2044, Santa Cruz Biotechnology, Inc., Paso Robles, CA) was about $1.50 per 4-well plate.

Thus, an experimental study was performed to compare the use of Image-iT FX and donkey serum as blocking reagents. In this study, one 4-well plate was used, with each treatment group corresponding to one well on the 4-well plate. The 4 treatment groups are depicted in the schematic of the 4-well plate setup in Figure 3.25.

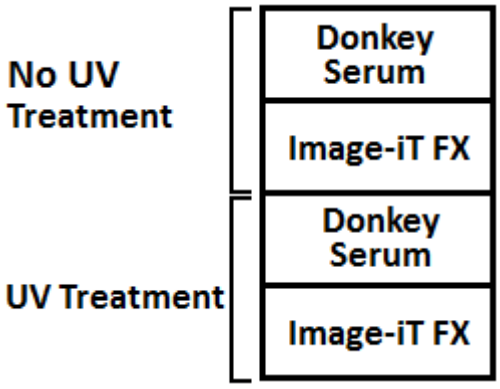

Figure 3.25 Four-well plate setup for the comparison of blocking reagents.

The two wells assigned with UV treatment were exposed to 40mJ/cm^2 of UV radiation, while the other two wells (controls) were exposed to no UV radiation by covering them with aluminum foil. After 24 hours of post-UV incubation, the samples were fixed with 3.7% formaldehyde, permeabilized with 0.1% Triton X-100, and blocked with either donkey serum or Image-iT FX. For the wells blocked with donkey serum, 3 blocking steps were performed, in which 1% donkey serum was added to the Triton X-100 solution and the primary and secondary antibody solutions (all diluted in PBS). For the wells blocked with Image-iT FX, 1 blocking step was performed, in which 4 droplets of Image-iT FX were added directly to each well. The p21 protein and cell nuclei were stained for using Alexa Fluor 488 and Hoechst stain, respectively. Once staining was complete, a confocal microscope was used to capture 2 confocal images per well. Each image was saved as a TIFF file for further analysis.

3.8.2 Results and Discussion

This preliminary study was meant to be a quick and simple test to see if donkey serum could be used as a replacement for Image-iT FX. Because of this, the sample size was small (n=1) and no statistical analysis was performed. Instead, the images were visually inspected for their quality of p21 staining (see Figure 3.26 for confocal images).

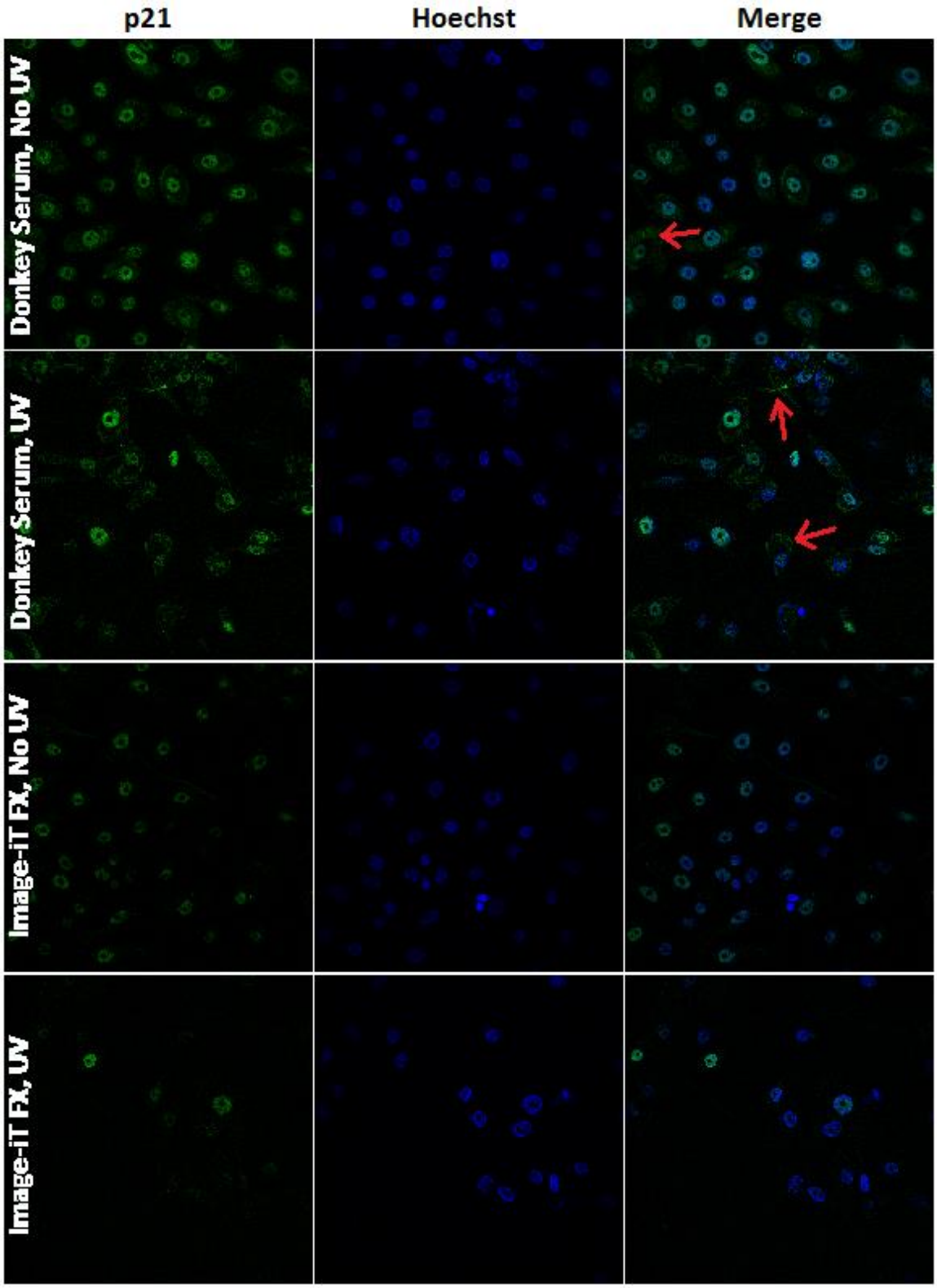

Figure 3.26 Representative confocal images of keratinocytes treated with different blocking reagents and with or without UV treatment. Red arrows indicate nonspecific fluorescence.

As depicted in Figure 3.26, the confocal images of the samples blocked with donkey serum showed relatively more nonspecific fluorescence, or background staining, compared to those blocked with Image-iT FX. The nonspecific fluorescence occurred mostly outside of cell nuclei and appeared to be within the cell cytoplasm. In addition, the images of the samples blocked with donkey serum showed relatively higher p21 (green) color intensity than those blocked with Image-iT FX. Nevertheless, both blocking reagents were considered to be adequate for producing satisfactory p21-stained fluorescence images, as samples blocked with either donkey serum or Image-iT FX all showed clear and reasonable nuclear p21 fluorescence. Because donkey serum showed to be more cost-effective and was readily available, it was selected to be used as the primary and sole blocking reagent in the finalized protocol.

Serum used for blocking reagents contains antibodies that bind to nonspecific reactive sites, thus preventing the secondary antibody from binding to these sites. Because the species that the secondary antibody (A11008, Life Technologies, Grand Island, NY) was generated in was goat, goat serum would have been a better blocking reagent than donkey serum. In fact, antibodies in goat serum have a higher affinity for binding to and blocking reactive sites that the goat secondary antibody would most likely nonspecifically bind to, compared to donkey serum. Due to the ready availability of donkey serum, however, donkey serum was used as an adequate alternative to goat serum.

Chapter 4: Methods for Finalized Protocol

4.1 Keratinocyte Culture

Aseptic technique in a sterile hood was used at all times during cell culture. Primary human epidermal keratinocytes isolated from normal, neonatal foreskin (PCS-200-010, ATCC, Manassas, VA) were cultured in a 37°C, 5% CO_2, humid incubator. Keratinocyte growth medium used for cultivation was prepared by mixing one Keratinocyte Growth Kit (PCS-200-040, ATCC, Manassas, VA), one bottle of Dermal Cell Basal Medium (PCS-200-030, ATCC, Manassas, VA), 0.5mL of Gentamicin-Amphotericin (PCS-999-025, ATCC, Manassas, VA), 0.5mL of Penicillin-Streptomycin-Amphotericin (PCS-999-002, ATCC, Manassas, VA), and 0.5mL of Phenol Red (PCS-999-001, ATCC, Manassas, VA) and passing the mixture through a 0.22μm filter. Keratinocytes were cultured in 4-well coverglass plates (155383, Thermo Scientific, Waltham, MA) and observed every 24 to 48 hours under a brightfield microscope to check for confluency, signs of microbial contamination, and cell morphology. Media was also changed every 24 to 48 hours, using 0.5mL of media per well. If any signs of over-confluency (≥100% confluence), microbial contamination, or unhealthy cell morphology were observed, cells were to be discarded so as not to risk the integrity of the experimental results.

A 70% confluent T-75 flask (passage 3) of keratinocytes was passed into twelve 4-well plates, giving an estimated seeding density of 6.8×10^4 cell/cm^2. This was calculated from a 1.8cm^2 surface area per well (Thermo Scientific) and a confluent T-75 flask estimated to contain 8.4 million cells (Life Technologies). Four treatment groups were used in this study with 3 4-well plates assigned to each group. Group 1(control

group) was to be treated with no sphingomyelin (SM) and no UV irradiation, Group 2 was to be treated with no SM and UV irradiation, Group 3 was to be treated with SM and no UV irradiation, and lastly, Group 4 was to be treated with both SM and UV irradiation (see Figure 4.1). Once all culture plates were about 70-80% confluent, the appropriate keratinocyte culture plates were treated with SM.

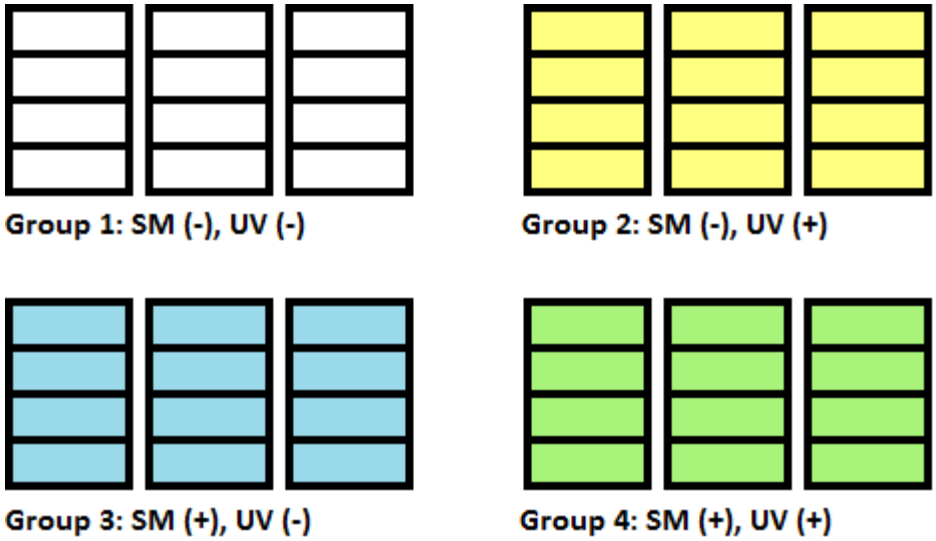

Figure 4.1 Schematic of the four treatment groups of human epidermal keratinocytes in 4-well plates.

4.2 Bovine Milk Sphingomyelin Treatment

Bovine milk sphingomyelin (SM) concentrate was provided by the team of Dr. Rafael Jiménez-Flores at the Dairy Science Department of California Polytechnic State University. The photo- and thermosensitive SM concentrate was stored at -20°C in a plastic conical tube wrapped in foil prior to use. A minimum of 12mL of sterilized SM solution was needed to treat the 6 4-well plates assigned with SM treatment (0.5mL SM solution per well). Since SM solution volume decreases when passed through a sterile filter, at least 12.5mL of SM solution was prepared.

A 0.1% SM solution was prepared by first weighing out at least 12.5mg of SM concentrate in a 15mL plastic conical tube (held upright by placing in a small glass beaker), using tweezers to transport the SM. When SM concentrate was placed on the scale, the scale mass readout was found to increase for a certain amount of time until it remained stable. This was thought to be due to the cold, dry SM powder absorbing moisture from the air. Thus, it was important to measure the SM mass as quickly as possible, in order to obtain accurate mass measurements. Once 12.5mg or more of SM concentrate was measured, the volume of keratinocyte growth media needed to make a 0.1% (w/v) SM solution was added to the 15mL conical. For example, 12.8mg of SM concentrate was measured out in this study, so 12.8mL of keratinocyte growth media was added. The SM solution was then heated to 37°C in a hot water bath to help the SM particles dissolve into solution. After heating to 37°C, the SM solution was vortexed (speed setting 7) until all SM particles dissolved. In a sterile hood, the SM solution was then sterilized by filtering it through a disposable 0.22μm syringe filter attached to a disposable 10mL syringe. The syringe filter was replaced if it became clogged up with particles that made it too difficult to push the solution through. Once the SM solution was filtered, it was placed in the 37°C hot water bath until needed.

Groups 3 and 4 both received SM treatment, which involved replacing the media in each well with 0.5mL of a 0.1% (w/v) SM solution and incubating the keratinocytes for 24 hours in the 37°C, 5% CO_2 incubator. Groups 1 and 2, which received no SM treatment, were given fresh keratinocyte growth media instead of the SM solution, and were likewise incubated for 24 hours. After the 24hr incubation period, all wells were rinsed twice with fresh keratinocyte growth media and then given 0.5mL of fresh media.

This was immediately followed by the appropriate UV irradiation treatments. (Note: All solutions placed on live keratinocytes were first warmed to 37°C in the hot water bath to avoid cold shocking the cells.)

4.3 UV Irradiation

UV irradiation was performed on Groups 2 and 4 using aseptic technique. Before UV irradiating the cells, the UV box (described in Chapter 3.2.3) was thoroughly sterilized by spraying and wiping with isopropyl alcohol (IPA) using paper towels, and then carefully placed and assembled inside the sterile hood. The UV lamp was also sprayed and wiped down with IPA and placed on top of the UV box inside the hood. The UV lamp used to irradiate the cells was a 302nm, polychromatic fluorescent lamp (95-0251-01, UVP, LLC, Upland, CA), and its spectral output is shown in Figure 4.3.

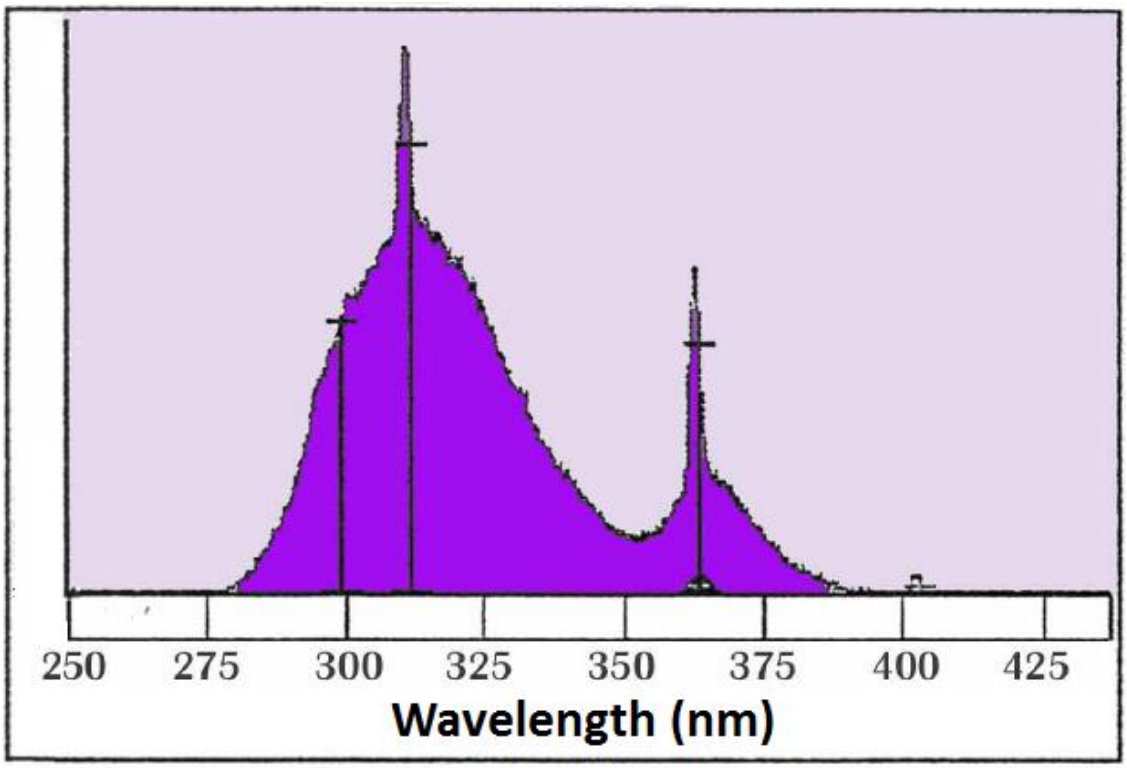

Figure 4.3 UV spectral chart for the 302nm UV lamp (UVP, LLC).

After the UV lamp and UV box were set up inside the hood, the switch for the 302nm bulb of the UV lamp was turned on. The UV lamp was then allowed to warm up for 5 minutes before UV power sensor readings were taken, using a power meter sensor (S120UV, ThorLabs, Newton, NJ). To obtain sensor readings, the outer casing of the sensor was first wiped down with IPA, without getting any IPA on the sensor itself. The sensor was then placed in one of the two circular holes in the ABS plastic tray inside of the hood (see Figure 3.6B). Next, the sensor was hooked up to the power meter (PM100, ThorLabs, Newton, NJ), and then slid into the UV box using the tray. Subsequently, the hood light and room lights were turned off, and a UV power measurement (in μW) was taken. For this study, the measured UV power was 212.5μW. This measurement was then used to calculate a measured irradiance value (in $\mu W/cm^2$), by dividing it by the sensor area of $0.7088cm^2$ (ThorLabs, Newton, NJ). This measured irradiance value was then used to calculate the exposure time necessary for a UV dose of $40mJ/cm^2$, which was determined to be 2 minutes and 13 seconds for this study. The following equation was used to calculate the exposure time:

$$\text{Exposure time (sec)} = \frac{\text{Presribed dose } (mJ/cm^2)}{(1mW/1000\mu W) \times \text{ Measured irradiance } (\mu W/cm^2)}$$

Once the appropriate exposure time was determined, the sensor and power meter were put away and the 4-well plates of Groups 2 and 4 were UV irradiated inside of the hood, again with the hood and room lights turned off. Two 4-well plates (one from each UV treatment group) were irradiated simultaneously by vertically aligning them side-by-side on the ABS plastic tray (see Figure 3.6C). The tray was manually slid in and out of the UV box at the appropriate times to achieve the determined exposure time. After

Groups 2 and 4 were UV irradiated, the UV lamp was turned off and removed from the hood. Groups 1 and 3 were then given a control treatment in which they were similarly placed inside of the UV box for the determined amount of exposure time, but with no UV irradiation. All 4-well plates were returned to the incubator and incubated for another 24 hours.

4.4 Fixation and Immunofluorescence Staining

After the 24hr post-UV incubation period, the twelve 4-well plates were removed from the incubator and the media from each well was aspirated out. Each well was then rinsed twice with warm (37°C) phosphate-buffered saline (PBS). Following this rinse step, warm (37°C) 3.7% formaldehyde (diluted from 16% formaldehyde [Cat. #15710, Electron Microscopy Sciences, Hatfield, PA] using PBS) was used to fix the keratinocytes in each well, incubating the plates for 15 minutes at room temperature. After the 15-minute incubation, the 3.7% formaldehyde solution was aspirated out of each well and the samples were rinsed twice with PBS. Once this was done, cells were permeabilized and nonspecific binding sites were blocked concurrently in a 0.1% Triton X-100, 1% donkey serum solution (diluted in PBS) for one hour at room temperature. Next, the cells were rinsed twice with PBS, and then incubated overnight at 4°C in the primary antibody solution, a 1/400 dilution of anti-p21 antibody (ab18209, Abcam, Cambridge, MA) with 1% donkey serum in PBS, which was to bind cellular p21 antigens. The following day, the primary antibody solution was aspirated out and the cells were rinsed twice with PBS. The secondary antibody solution, a 1/400 dilution of Alexa Fluor 488 (A11008, Life Technologies, Grand Island, NY) with 1% donkey serum in PBS, was then applied to each well to fluorescently tag the anti-p21 antibodies that

were bound to the cellular p21 antigens. Immediately after applying the secondary antibody, the plates were wrapped in foil to prevent photobleaching and incubated for one hour at room temperature. Once one hour passed, the secondary antibody was aspirated out, cells were rinsed twice with PBS, and Hoechst stain (5μg/mL, diluted in PBS) was applied to each well for 15 minutes at room temperature to stain cell nuclei. Finally, the Hoechst stain was aspirated out and the cells were rinsed twice with PBS. A thin layer (200μL) of fresh PBS was left in each well for the remainder of the study to prevent the cells from drying out and crystallization from occurring.

4.5 Imaging

Once the immunofluorescence staining procedures were completed, samples were imaged using an Olympus FluoView FV1000 confocal microscope (Olympus America, Centerville, PA). In the FluoView software window, the DAPI (for Hoechst stain) and Alexa Fluor 488 filter sets were selected. With the 40x oil immersion objective engaged, oil was added to the objective and a 4-well plate was mounted onto the stage. The keratinocytes were located and put into focus using transmitted light (brightfield). Once in focus, widefield fluorescence imaging was used to locate an area with high keratinocyte nuclei confluency (blue ovals), little background staining, and clear p21 expression (green spots). Next, using the FluoView software, the scan speed was set to 4μs/pixel, image size was set to 512 x 512 pixels, and zoom was set to 1x. The "XY Repeat" button, which is used for repeated scanning, was then selected to start the confocal laser scanning of the sample. The laser power, HV, and offset settings were adjusted to optimize the signal and quality of each channel (DAPI and Alexa Fluor 488). HV, or high voltage, is used to control the sensitivity of the photon detector to produce a

clear signal; and offset is used to adjust the overall signal level to reduce background noise. With the "Sequential" function selected to avoid bleed-through fluorescence, five confocal images were taken for each well in each of the twelve 4-well plates (a total of 240 images). To ensure sample observations were independent of one another (important for statistical analysis), plates were imaged in a randomly selected order and the treatment groups were kept unknown to the researcher throughout imaging, with the aid of an assistant. All images were saved as TIFF files for image analysis. Also, in order to be able to properly compare the images to one another, the same settings (e.g. laser power, HV, offset, etc.) were used for every image.

4.6 Image Analysis

The IntenseCount program (see Chapter 3.1) was used to read in the confocal images and calculate the mean pixel intensity (0-255) of nuclear p21 expression per image. The raw mean intensity values were stored in an Excel spreadsheet for further analysis. The 5 raw mean intensity values corresponding to each of the 5 images taken per well, were averaged to obtain one data point per well. This gave a total of 4 data points for each of the 4-well plates, with each plate in a particular treatment group considered as one replicate. Since there were three 4-well plates per treatment group, the analysis consisted of 3 replicates with 4 data points per replicate per treatment group, giving a total of 48 data points to be statistically analyzed. Using JMP statistical software (SAS Institute Inc., Cary, NC), an ANOVA (α=0.05) was performed on the 48 data points to compare the mean nuclear p21 intensity data between all four treatment groups and to determine if significant differences exist. The model effects tested for were the effect of SM treatment, the effect of UV treatment, the interaction effects between SM treatment

and UV treatment, and the effect of replicate (plate) number. Additionally, in conjunction with the ANOVA, Tukey's test (α=0.05) was used to find out between which two groups a significant difference exists, if any.

Chapter 5: Results for Finalized Protocol

5.1 Verification of ANOVA Assumptions

For an ANOVA test to be valid, the following three conditions had to be met: 1) independent observations, 2) equal variances, and 3) normally distributed residuals. Because the confocal images of the different treatment groups were randomly and blindly taken (see Chapter 4.5), and because the sample plates were randomly assigned to each treatment, the independence assumption was considered to be met. The residual versus predicted plot in Figure 5.1 was used to determine if the equal variances assumption was met. In this graph, sample variances are represented by the vertical spread of the residual data points at each predicted mean nuclear p21 intensity. Since the vertical spread of the stripe of points furthest to the left was smaller than the vertical spread of the other two stripes of points, the variances were not considered to be equal. However, it is known that when treatment groups have equal sample sizes, the ANOVA test is robust enough to accommodate for unequal variances (Rogan, 1977). Because the sample sizes used in the finalized protocol were equal, the violation of the equal variances assumption was considered to be okay, and the ANOVA test results could still be trusted.

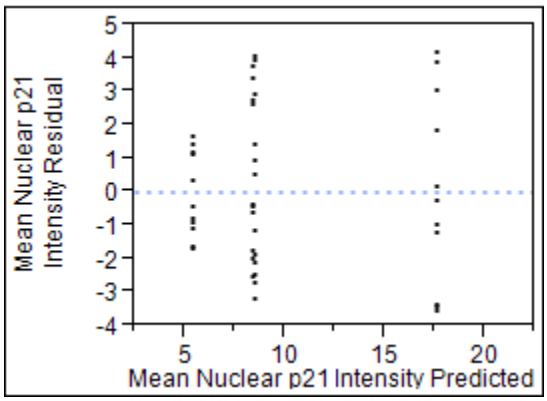

Figure 5.1 Residual versus predicted plot for mean nuclear p21 intensity.

In testing the third ANOVA assumption of normally distributed residuals, the residuals were initially found to not follow a normal distribution. As seen in the histogram of residuals in Figure 5.2A, one outlier existed in the data, which occurred in the first replicate of the SM (-), UV (+) treatment group and was considered to skew the data enough to violate the normality assumption. After excluding this outlier, the residuals were found to follow a normal distribution. This was determined through observation of the normal quantile plot given in Figure 5.2B, which shows the data points roughly following the red diagonal line of the ideal normal distribution. Thus, the third ANOVA assumption was considered to be met.

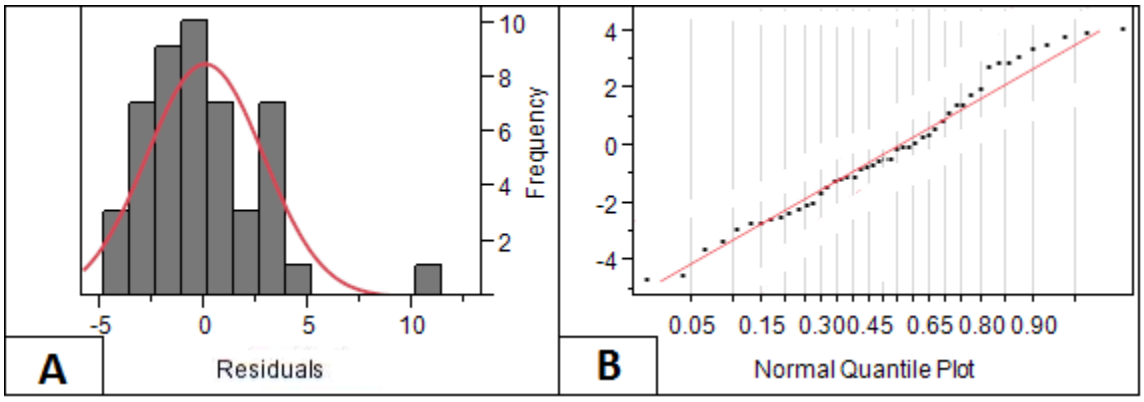

Figure 5.2 Residuals of mean nuclear p21 intensity data. A) Histogram of residuals before removing outlier with overlying normality curve (red line). B) Normal quantile plot of residuals after removing outlier.

5.2 Statistical Analysis

The effects of SM and UV treatment, as well as the interaction effects between SM and UV, caused significant differences in mean nuclear p21 intensity in the confocal images of human keratinocytes (via ANOVA; $p<0.05$), while the effect of replicate number did not (via ANOVA; $p>0.05$). In other words, nuclear p21 expression in human keratinocytes was found to be dependent on whether or not exogenous SM was added to the culture media and whether or not the cells were exposed to UV radiation, and did not

depend on replicate number. A summary table of mean nuclear p21 intensities and standard errors for each treatment group is given in Table 5.1. (Note: The four treatment groups are color-coordinated corresponding to Figure 4.1.)

Table 5.1 Mean Nuclear p21 Intensities and Standard Errors

Treatment Group	Mean Nuclear p21 Intensity (0-255)	Standard Error
SM (-), UV (-)	5.431	0.36
SM (-), UV (+)	17.63	0.87
SM (+), UV (-)	8.443	0.70
SM (+), UV (+)	8.537	0.76

A box plot showing the distribution of mean nuclear p21 intensity of each treatment group is shown in Figure 5.3. As depicted in this figure, the highest mean nuclear p21 intensity 24hrs post-UV occurred in the UV-irradiated keratinocytes with no SM treatment. Based on statistical analysis, mean nuclear p21 intensity of UV-irradiated keratinocytes treated with no SM was over threefold greater than that of non-UV-irradiated keratinocytes treated with no SM (via Tukey's test; $p<0.05$), and approximately twofold greater than that of both the SM-treated keratinocyte groups (via Tukey's test; $p<0.05$). These results indicated that keratinocytes treated with SM were protected from UV-induced nuclear p21 overexpression at 24hrs post-UV, whereas keratinocytes not treated with SM were not protected. Additionally, the mean nuclear p21 intensities of the two SM (+) treatment groups were both over one and a half times larger than the mean of the SM (-), UV (-) control group (via Tukey's test; $p<0.05$). No significant difference existed between the mean nuclear p21 intensities of the two SM-treated groups (via Tukey's test; $p>0.05$). An interaction plot showing the effects of SM and UV treatment on mean nuclear p21 fluorescence intensity in keratinocytes is given in Figure 5.4.

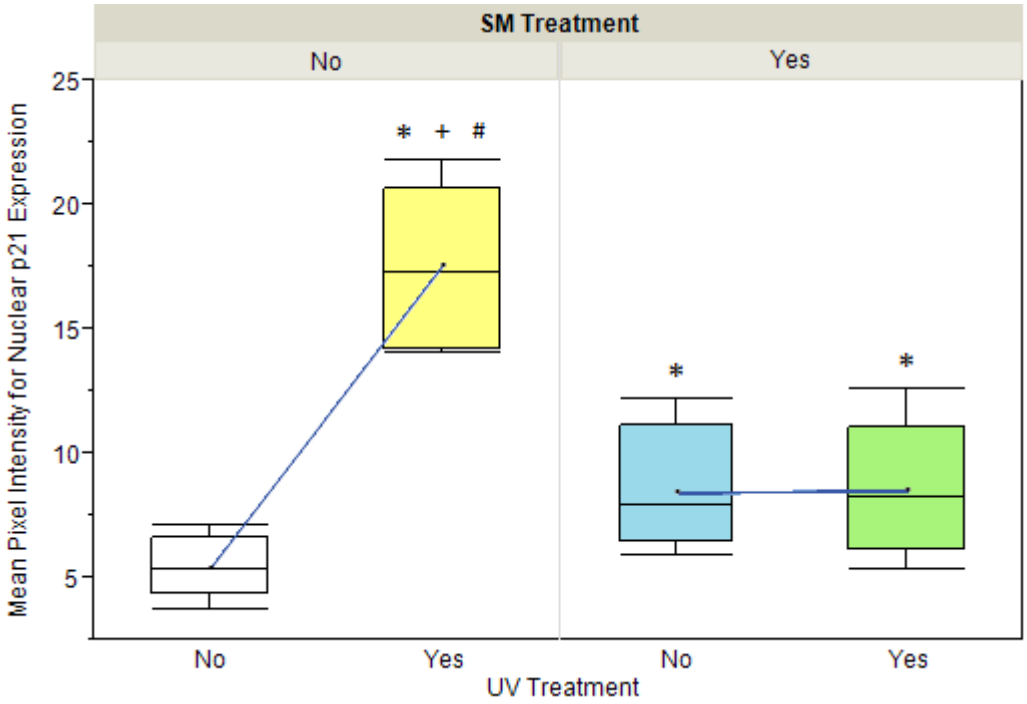

Figure 5.3 Box plot of the distribution of mean nuclear p21 intensity for each group.
* indicates p<0.05 via Tukey's test compared with SM (-), UV (-) control group.
$^{+}$ indicates p<0.05 via Tukey's test compared with SM (+), UV (-) group.
$^{\#}$ indicates p<0.05 via Tukey's test compared with SM (+), UV (+) group.

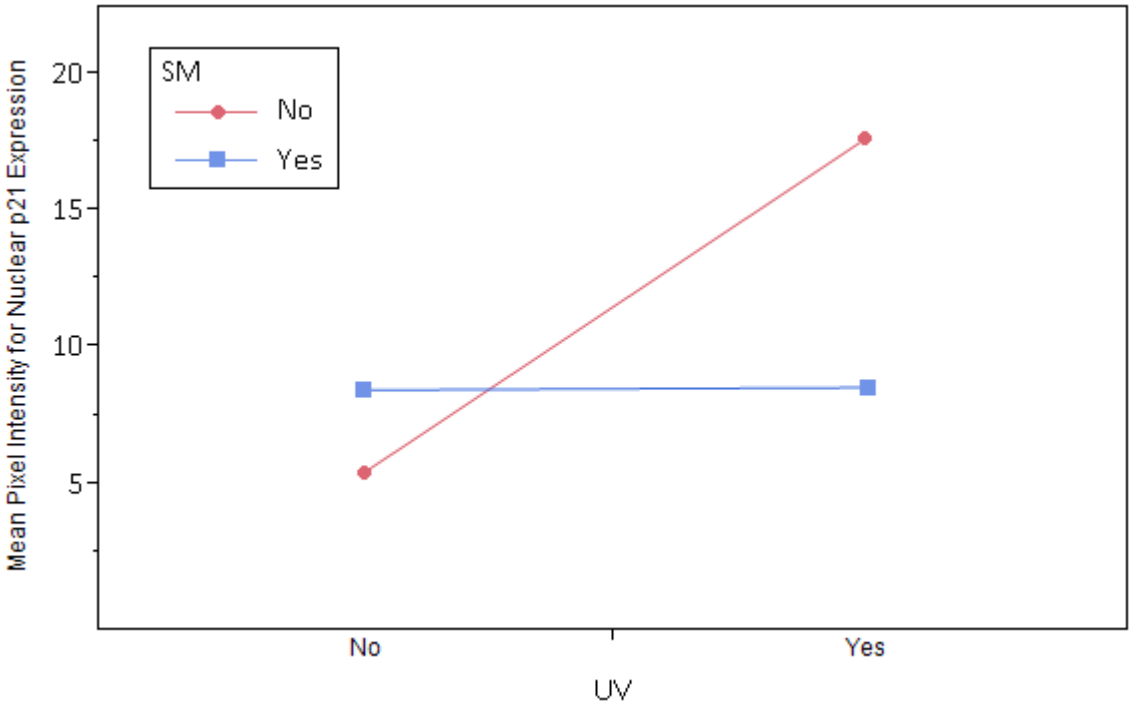

Figure 5.4 Interaction plot showing the effects of SM and UV treatments on mean nuclear p21 intensity, corresponding to nuclear p21 expression in human keratinocytes.

As shown in Figure 5.4, the nuclear p21 intensity means for the two SM-treated groups (blue line) were about the same. On the other hand, in the two non-SM-treated groups (red line), the mean nuclear p21 pixel intensities for the UV-treated group were higher than the mean intensities for the non-UV-treated group. Thus, the effect of UV treatment on nuclear p21 expression in human keratinocytes depended on whether or not keratinocytes were given SM treatment. In the case of no SM treatment, UV treatment caused a significant increase in keratinocyte nuclear p21 expression compared to the non-UV treatment control. When SM treatment was given, however, UV treatment caused no significant difference in keratinocyte nuclear p21 expression compared to the non-UV treatment control. Furthermore, in the two no UV groups, mean nuclear p21 intensity was higher in keratinocytes treated with SM compared with those not treated with SM.

5.3 Confocal Images

Representative confocal images of the four treatment groups are given in Figure 5.5. Overall, nuclear p21 fluorescence was scarce in the SM (-), UV (-) control group, as depicted by the lack of bright green ovals in the first row of Figure 5.5. The SM (-), UV (+) group showed the greatest intensities of nuclear p21 fluorescence compared to the other groups, as depicted by the bright green ovals in the second row of Figure 5.5. Similar to the SM (-), UV (-) control group, nuclear p21 fluorescence was scarce in the two SM-treated groups, whose images showed only around 1-3 relatively intense green ovals per image. Throughout imaging, p21 fluorescence outside of cell nuclei, either in the cytoplasm or extracellular space, appeared as scattered green specks. However, it was unclear whether the extranuclear p21 fluorescence occurred from cell signaling or nonspecific staining. No significant signs of apoptosis were found during imaging.

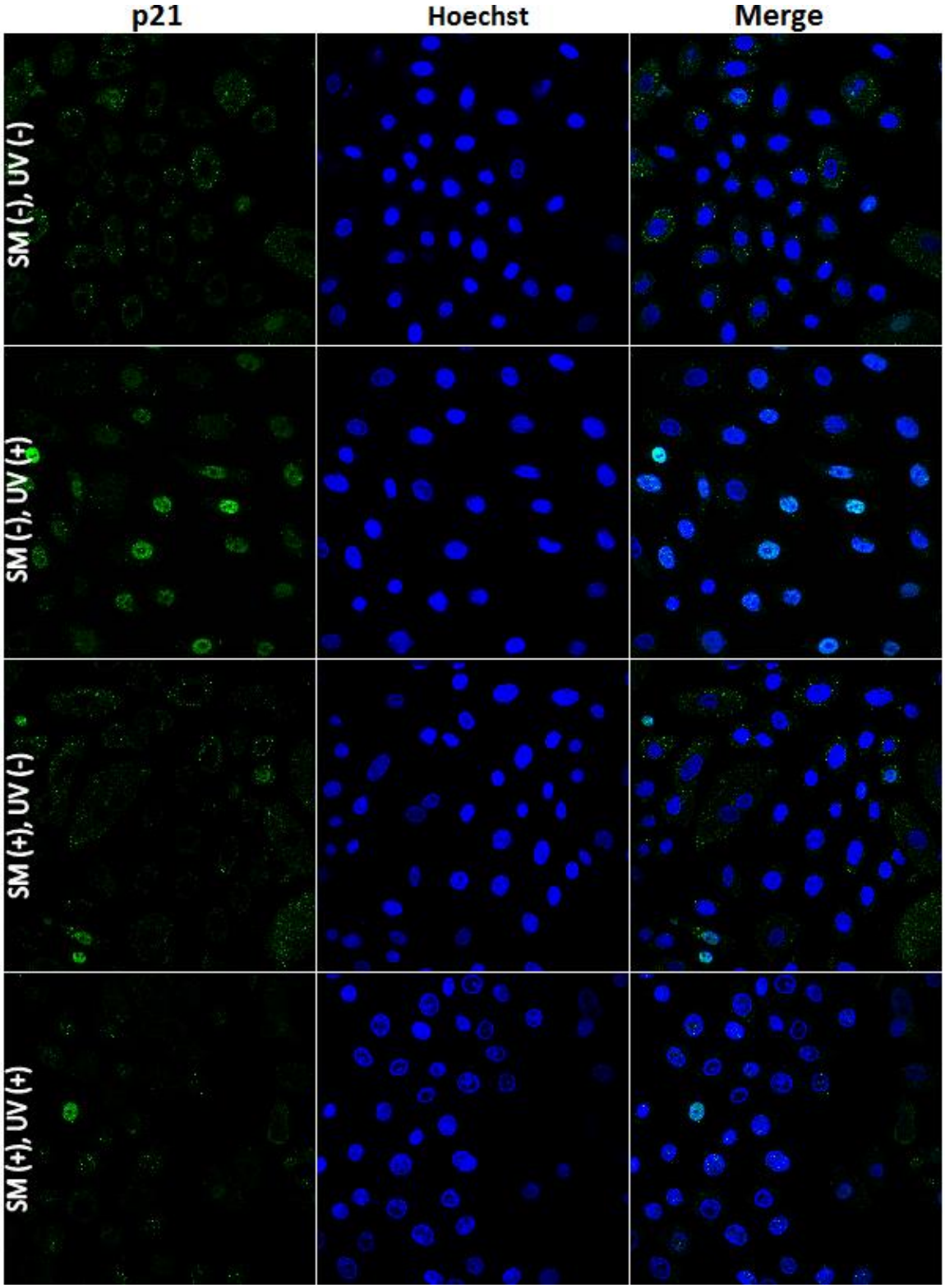

Figure 5.5 Representative confocal images of p21 expression (green) and keratinocyte nuclei (blue) of the different treatment groups.

Chapter 6: Discussion, Conclusions, and Future Work

6.1 Summary of Results

Using the mean nuclear p21 intensity results given in Chapter 5, several conclusions on sphingomyelin's effects on nuclear p21 expression in normal human epidermal keratinocytes, 24hrs post-UV treatment, were made (mean nuclear p21 intensity was directly correlated with p21 expression):

1. Nuclear p21 expression significantly increases in keratinocytes treated with 40mJ/cm^2 UVB radiation compared to non-UV-treated keratinocytes.
2. Exogenously added SM causes a significant decrease in nuclear p21 expression in UV-treated keratinocytes compared to no SM, UV-treated keratinocytes.
3. Nuclear p21 expression of SM-treated keratinocytes is about the same for both SM (+) groups, regardless of whether or not they were UV irradiated.
4. Exogenously added SM causes a significant increase in the baseline of nuclear p21 expression found in non-UV-treated keratinocytes compared to no SM treatment.

In explanation of the above conclusions, two hypotheses were formed. They are the following:

1. Exogenously added SM protects against UV-induced DNA damage in normal human epidermal keratinocytes, possibly through inhibition of ROS formation.

This hypothesis would explain why nuclear p21 expression was significantly lower in SM-treated keratinocytes compared to the non-SM treated groups, assuming that nuclear p21 expression 24hrs post-UV treatment is a positive marker for severe DNA damage. In response to high doses of UV irradiation ($\geq$ 40mJ/cm^2) that cause

overwhelming DNA damage, various cell types are known to inhibit DNA repair by blocking the degradation of nuclear p21 up to 24hrs post-UV (Bendjennat et al. 2003). Since high levels of nuclear p21, 24hrs post-UV irradiation, are known to inhibit the function of PCNA in DNA repair synthesis, blocking the degradation of p21 allows the cell to avoid the risk of carcinogenesis due to mutagenic DNA repair when DNA damage is severe (Hattinger et al. 2002). Therefore, instead of risking the possibility of mutagenesis, this pathway arrests the cell cycle and encourages programmed cell death (Hattinger et al. 2002). This may explain why UVB irradiation of normal human epidermal keratinocytes led to a significant increase in nuclear p21 expression 24hrs post-UV, by indicating the cells were undergoing apoptosis to avoid mutagenesis. Since SM treatment was shown to inhibit the increase of nuclear p21 (24hrs post-UV) in UV-treated keratinocytes, it is possible that the SM protected the cells against severe UV-induced DNA damage. In this case, it is possible that nuclear p21 was degraded by 24hrs post-UV irradiation in order for DNA repair and cell survival to occur. In the non-UV-treated keratinocytes, the observed increase in nuclear p21 expression caused by exogenous SM could be explained by the inherent toxic potential of any exogenous substance causing a cell stress response involving p21-induced cell cycle arrest and cellular senescence, which can lead to cell death.

While the mechanisms behind the protective effects of SM against UV photodamage remain unclear, one possible mechanism was considered based off the following arguments: that exogenous SM incorporates into cell membranes and disrupts well-formed lipid rafts when added to the media of keratinocytes under cultivation (Pillai et al. 1998), and that disruption of lipid rafts in keratinocyte membranes causes a

significant decrease in UV-induced ROS synthesis (Gniadecki et al. 2002). Thus, in explaining the mechanism behind the potential role of SM protecting human skin against UV photodamage, it is possible that exogenously added SM disrupts lipid raft structure in normal human epidermal keratinocytes, leading to decreased UV-induced ROS formation and decreased ROS-induced DNA damage. Decreased ROS-induced DNA damage could in turn be responsible for the observed decrease in keratinocyte nuclear p21 expression 24hrs post-UV irradiation, since degradation of p21 is required for DNA repair of non-severe and repairable DNA damage (Bendjennat et al. 2003).

Further research is needed to verify this first hypothesis. Future studies should first aim at evaluating the potential toxic effects of exogenous SM causing cell death or cell senescence, since such effects would undermine the safety of exogenous SM as a cancer preventative agent. If exogenous SM is found to cause any signs of cell toxicity, lower doses of SM should be investigated. Once exogenous SM is shown to cause no toxic effects in normal human epidermal keratinocytes, studies should begin focusing on directly quantifying DNA damage in UV-irradiated keratinocytes. By doing so, it would be possible to make definitive conclusions on whether or not SM protects keratinocytes against UV-induced DNA damage. If future studies are able to show a clear decrease in UV-induced DNA damage in SM-treated keratinocytes, then the next step should be to investigate the underlying mechanisms of UV photoprotection by the addition of exogenous SM in keratinocyte culture. Such investigations on the underlying mechanisms could start by exploring the relationship between exogenous SM and ROS formation in normal human epidermal keratinocytes. This can be accomplished through the application of commercially available ROS dyes to determine the presence of ROS in

UV-irradiated keratinocytes with and without SM treatment. If no relationship is found, other mechanisms should be considered to better understand the behavior of exogenously added SM in cell culture.

2. Exogenously added SM does not protect against UV-induced DNA damage in normal human epidermal keratinocytes, but instead, provokes cell signaling involved with decreasing nuclear p21 expression by 24hrs post-UV irradiation independent of DNA damage.

It is possible that, at 24hrs post-UV, the significantly lower levels of nuclear p21 protein observed in SM (+), UV (+) keratinocytes compared to SM (-), UV (+) keratinocytes were not due to SM protecting the cells from UV-induced DNA damage. Severe UV-induced DNA damage could have been present in the SM (+), UV (+) keratinocytes (24hrs post-UV) despite the significantly lowered nuclear p21 expression observed. For example, in mutated cells lacking p21, cell cycle arrest still occurs in response to UV-induced DNA damage, by a signaling pathway involving the degradation of Cdc25A (Bartek et al. 2001). Consequently, it is hypothesized that the significantly lowered levels of nuclear p21 in the SM (+), UV (+) keratinocytes were not due to low DNA damage, but were instead caused by exogenous SM provoking cell signaling pathways that involve a decrease in nuclear p21. Moreover, as reported by multiple studies (e.g. Lasserre et al. 2008 and Al-Makdissy et al. 2003), it is thought that the exogenous SM could have initiated such cell signaling pathways by incorporating into the cell membrane, disrupting normal lipid raft formations, and affecting lipid-raft-dependent cell membrane signaling cascades.

Currently, disruption of lipid rafts has been shown to stimulate both cell survival and cell death processes (thus, affecting p21 expression), depending on the experimental procedures used (George et al. 2012). For example, it was reported that exogenous SM added to the media of human epidermal keratinocytes activates keratinocyte proliferation, possibly by exogenous SM incorporating into the cell membrane and altering lipid raft formations important for proliferation (Pillai et al. 1999). Two pathways were considered that could explain how lipid raft disruption can lead to cell survival. The first pathway involves the recruitment and activation of the Akt survival protein. In simian kidney cells, SM-enriched lipid rafts are crucial for Akt activation (Lasserre et al. 2008). While artificially blocking the formation of lipid rafts inhibits Akt activation , exogenous SM added to the cell media is able to incorporate into the cell membrane, restore normal lipid raft formations, and induce cell proliferation signaling by recruiting the Akt protein to the cell membrane for activation (Lasserre et al. 2008). Once activated, Akt is capable of upregulating cell proliferation (Lasserre et al. 2008). Additionally, Akt is known to phosphorylate p21, which results in nuclear p21 being translocated to the cytoplasm for degradation (Child et al. 2006). Since nuclear p21 causes cell cycle arrest and inhibition of DNA repair (by blocking the function of PCNA), the degradation of nuclear p21 removes the p21-induced cell cycle arrest and enables DNA repair. Thus, in this thesis, exogenous SM could have altered the lipid rafts of normal human epidermal keratinocytes in such a way that cell survival (or a decrease in nuclear p21) via Akt was induced, even in cells containing UV-induced, mutagenic DNA damage.

The second pathway that was considered in explanation of cell survival following lipid raft disruption by exogenous SM involves the recruitment and activation of an

enzyme called Protein Kinase C ζ (PKCζ). In rat embryonic smooth muscle cells, exogenous ceramide (a SM breakdown product) incorporates into the cell membrane and forms ceramide-enriched lipid rafts (Fox et al. 2007). This, in turn, causes an increase in PKCζ activation, since PKCζ is a direct target for ceramide (Fox et al. 2007). In several mammalian cell types, overexpression of PKCζ causes the phosphorylation and degradation of nuclear p21 (Scott et al. 2002). Consequently, like Akt, PKCζ is likely capable of decreasing nuclear p21 levels to induce DNA repair and cell survival, despite the current state of the cell's DNA (Scott et al. 2002). In regard to this thesis, it is possible that the exogenously added SM was broken down into ceramide by membrane SMases, which could have caused ceramide-dependent activation of PKCζ as described above. Therefore, exogenous SM added to the media of normal human epidermal keratinocytes could have led to ceramide-induced disruption of lipid rafts and initiation of cell survival (or a decrease in nuclear p21) via PKCζ activation, despite the presence of UV-induced, mutagenic DNA damage. In addition, as stated in the first hypothesis, the observed increase in nuclear p21 expression in the non-UV-treated keratinocytes caused by SM treatment could be due to the inherent toxic potential of any exogenous substance causing a cell stress response involving p21-induced cell cycle arrest and cellular senescence.

In contrast to stimulating cell survival, lipid raft disruption is also capable of stimulating cell death processes in human keratinocytes (George et al. 2012), which is hypothesized to affect nuclear p21 expression. In human keratinocytes, the abundance of cell membrane cholesterol plays a central role in UVB-induced apoptosis (George et al. 2012). In fact, artificially depleting cholesterol concentrations in lipid rafts, using a

reagent called methyl-β-cyclodextrin (MβCD), reduces UVB-induced apoptosis, but increases non-apoptotic cell death (i.e. necrosis) in human keratinocytes, regardless of whether or not the cells were UVB irradiated (George et al. 2012). Additionally, exogenous SM is known to integrate into the cell membrane and increase the membrane SM/cholesterol ratio in lipid rafts (Al-Makdissy et al. 2003). Therefore, like the MβCD reagent mentioned above, it is possible that the exogenous SM used in this thesis decreased cholesterol concentrations in the lipid rafts of normal human epidermal keratinocytes, causing the corresponding increase in necrosis in both UV-treated and non-UV-treated keratinocytes. More importantly, it is possible that both SM-treated keratinocyte groups were undergoing SM-induced necrosis even before UV irradiation was performed. This could explain why no significant difference in nuclear p21expression was found between the two SM-treated keratinocyte groups. Although the molecular fate of p21 following the onset of necrosis is still not well understood, depletion of p21 expression has been positively correlated with the occurrence of necrosis in canine kidney cells (Nie et al. 2012); which could explain why SM (+), UV (+) keratinocytes had significantly lower nuclear p21 expression than that of SM (-), UV (+) keratinocytes (24hrs post-UV). While depletion of p21 has been associated with necrosis (Nie et al. 2012), some p21 induction is still necessary for necrosis to occur (Kwon et al. 2003).This could explain why nuclear p21 expression in non-UV-treated keratinocytes increased with SM treatment, since the signaling pathways involved with SM-induced necrosis could have caused the observed increase in nuclear p21.

It is recommended that future work aimed at investigating this second hypothesis should initially focus on ruling out the potential toxic effect of exogenous SM inducing

necrosis (or cell death) in normal human epidermal keratinocytes, since such an effect is highly undesirable for any cancer preventative agent. Other potential negative effects of exogenous SM should also be investigated, such as induction of cell senescence, or inhibition of cell growth and proliferation. A common technique that can be done to assess cell proliferation is the MTT assay, which is a colorimetric assay used to measure the cell proliferation rate and decreases in cell viability (ATCC, 2011). Additionally, cell proliferation and viability should be assessed at later time points than the 24hr post-UV incubation time point used in this thesis, since UV-induced apoptosis in human keratinocytes has been reported to occur between 24 to 48 hours following UV irradiation (Raj et al. 2006). If the exogenous SM is found to elicit toxic or other negative effects on normal human keratinocytes, then lower doses of exogenous SM should be assessed. On the other hand, if no toxic or other negative effects of exogenous SM on keratinocytes are found, then the next step would be to investigate the relationship between exogenous SM and UV-induced DNA damage. In particular, further studies are needed to obtain reliable evidence that proves whether or not exogenous SM protects against UV-induced DNA damage in human epidermal keratinocytes. If sufficient evidence is collected to support the argument that exogenous SM does not protect against UV-induced DNA damage, then subsequent studies would be necessary to better understand the effects of exogenous SM on normal cell signaling pathways and to explain the observed decrease in UV-induced nuclear p21 in SM-treated keratinocytes. Such studies should investigate the hypothesized occurrence of exogenous SM incorporating into keratinocyte lipid rafts, as well as any downstream effects of exogenous SM on cell signaling pathways (e.g. changes in cell proliferation signaling or differences in the expression of specific cell

cycle proteins such as p21). Lastly, while this thesis focused on exogenous SM as a skin cancer preventative, future studies could expand on this scope by evaluating exogenous SM as a skin cancer treatment. In fact, numerous reports have already indicated the potential use of exogenous sphingolipids, in conjunction with chemotherapy, to stimulate apoptosis of cancerous cells and minimize drug resistance (Modrak et al. 2006).

6.2 Challenges and Limitations

Due to the current understandings of p21 functions being highly controversial (see Chapter 2.4), interpreting experimental results involving p21 expression was a fundamental challenge throughout this thesis. For example, it was recently reported that the p21 protein inhibits DNA repair and has a pro-apoptotic function following UV-induced DNA damage (Mansilla et al. 2013). However, it was also reported that the p21 protein, in response to DNA damage, promotes DNA repair and has an anti-apoptotic function (Cazzalini et al. 2010 and Lei et al. 2010). Additionally, while it was initially intended for p21 to be a marker for cell cycle arrest and UV-induced DNA damage in human epidermal keratinocytes, it was later found that previous reports had shown cell cycle arrest to occur independently of p21 expression following UV irradiation of various cell types (Bendjennat et al. 2003). Thus, it was difficult to make definitive conclusions on the observed patterns of p21 expression.

Another issue that arose was the sample sizes of the preliminary experiments being too small for showing statistically significant differences between treatment groups. During the preliminary experiments (see Chapter 3), small sample sizes were favored due to feasibility and limited time. Also, obtaining statistically significant results by using large sample sizes was of low concern during the preliminary experiments, since

the main purpose of these experiments was simply to optimize the finalized protocol. As such, observing trends in the preliminary experimental results was, at the time, considered to be sufficient for selecting one procedural step over another. Nevertheless, using small sample sizes increased the risk of errors in the conclusions made for the preliminary experiments that showed no statistically significant results (i.e. Determination of Post-UV Incubation Period, Determination of Primary and Secondary Antibody Concentrations, and Comparison of Blocking Reagents). In these experiments, conclusions were based off of trends observed in the sample data. Because of the small sample sizes, the sample data trends may not have been good representations of the true characteristics of the population. Thus, future research is necessary to completely optimize the finalized protocol through statistically credible data. To avoid the issue of small sample size when designing an experiment, power analysis should be implemented to estimate the minimum sample size needed to show statistical differences.

6.2 Conclusions

Bovine milk sphingomyelin causes a statistically significant decrease in nuclear p21 expression of UV-irradiated keratinocytes, but causes a significant increase in nuclear p21 expression of non-UV-irradiated keratinocytes (24hrs post-UV). Since p21 is known to cause cell cycle arrest in response to cellular stress such as DNA damage, it is possible that exogenous sphingomyelin significantly decreased nuclear p21 levels by protecting the UV-irradiated keratinocytes against UV-induced DNA damage, but slightly increased nuclear p21 levels in non-UV-irradiated keratinocytes by acting as a cellular stressor. Although the molecular fate of exogenous sphingomyelin in normal human epidermal keratinocyte culture is still uncertain, it is strongly hypothesized that

exogenous sphingomyelin incorporates into the membrane lipid rafts of keratinocytes and alters intracellular signaling pathways that likely affect nuclear p21 expression. However, as the p21 protein is neither a definitive nor direct marker for DNA damage, subsequent studies are needed to determine whether exogenous sphingomyelin actually protects human epidermal keratinocytes against UV-induced DNA damage, and to possibly further reveal the potential of sphingomyelin as a preventative agent against non-melanoma skin cancer.

BIBLIOGRAPHY

Achay, Z. M. (2011). *Protective effects of milk phospholipids against UV photodamage in human skin equivalents.* Thesis, California Polytechnic State University, Biomedical Engineering, San Luis Obispo.

Afaq, F. (2011). Natural agents: Cellular and molecular mechanisms of photoprotection. *Archives of Biochemistry and Biophysics*, 144-151.

Ahmed, N., Ueda, M., & Ishihashi, M. (1999). Induced expression of p16 and p21 proteins in UVB-irradiated human epidermis and cultured keratinocytes. *Journal of Dermatological Science*, 175-181.

Al-Makdissy, N., Younsi, M., Pierre, S., Ziegler, O., & Donner, M. (2003). Sphingomyelin/cholesterol ratio: an important determinant of glucose transport mediated by GLUT-1 in 3T3-L1 preadipocytes. *Cellular Signalling*, 1019-1030.

American Cancer Society. (2013). *Cancer Facts & Figures 2013.* Atlanta: American Cancer Society.

ATCC. (2011). *MTT Cell Proliferation Assay-Instruction Guide.* Retrieved from atcc.org: http://www.atcc.org/~/media/DA5285A1F52C414E864C966FD78C9A79.ashx

ATCC. (2013). *Product Sheet: Primary Epidermal Keratinocytes; Normal, Human, Neonatal Foreskin.* Manassas, VA: ATCC.

Baliga, M. S., & Katiyar, S. K. (2006). Chemoprevention of photocarcinogenesis by selected dietary botanicals. *Photochemical & Photobiological Sciences*, 243-253.

Balk, S. J. (2011). Ultraviolet Radiation: A Hazard to Children and Adolescents. *Pediatrics*, e791-e817.

Ball, K. (1997). p21: structure and functions associated with cyclin-CDK binding. *Progress in Cell Cycle Research*, 125-134.

Baroni, A., Buommino, E., De Greggio, V., Ruocco, E., Ruocco, V., & Wolf, R. (2012). Structure and function of the epidermis related to barrier properties. *Clinics in Dermatology*, 257-262.

Bartek, J., & Lukas, J. (2001). Pathways governing G1/S transition and their response to DNA damage. *Federation of European Biochemical Societies*, 117-122.

Bendjennat, M., Boulaire, J., Jascur, T., Brickner, H., Barbier, V., Sarasin, A., et al. (2003). UV Irradiation Triggers Ubiquitin-Dependent Degradation of p21 to Promote DNA Repair. *Cell*, 599-610.

Bensouilah, J., & Buck, P. (2006). *Aromadermatology: Aromatherapy in the Treatment and Care of Common Skin Conditions.* Radcliffe Publishing.

Bianco, P., Robey, P. G., Pennesi, G., & Cancedda, R. (2008). Chapter 10: Cell Source. In C. van Blitterswijk (Ed.), *Tissue Engineering* (pp. 279-306). Elsevier.

Bissonnette, R. (2008). Update on Sunscreens. *Skin Therapy Letter*, 5-7.

Black, H., & Rhodes, L. (2006). The potential of omega-3 fatty acids in the prevention of non-melanoma skin cancer. *Cancer Detection and Prevention, 30*(3), 224-232.

Blundell, R. (2006). The Biology of p21. *American Journal of Biochemistry and Biotechnology*, 33-40.

Bolton, J., & Linden, K. (2003). Standardization of Methods for Fluence (UV Dose) Determination in Bench-Scale UV Experiements. *Journal of Environmental Engineering*, 209-215.

Boya, P., Gonzalez-Polo, R.-A., Casares, N., Perfettini, J.-L., Dessen, P., Larochette, N., et al. (2005). Inhibition of Macroautophagy Triggers Apoptosis. *Molecular and Cellular Biology*, 1025-1040.

Camp, W., & et al. (2011, March). New Agents for Prevention of Ultraviolet-Induced Nonmelanoma Skin Cancer. *Seminars in Cutaneous Medicine and Surgery*, 6-13.

Cataisson, C., Salcedo, R., Hakim, S., Moffitt, B. A., Wright, L., Yi, M., et al. (2012). IL-1R–MyD88 signaling in keratinocyte transformation and carcinogenisis. *Journal of Experimental Medicine*, 1689-1702.

Cazzalina, O., Scovassi, A. I., Savio, M., Stivala, L. A., & Prosperi, E. (2010). Multiple roles of the cell cycle inhibitor p21 in the DNA damage response. *Mutation Research*, 12-20.

Child, E., & Mann, D. (2006). The intricacies of p21 Phosphoylation. *Cell Cycle*, 1313-1319.

Contarini, G., & Povolo, M. (2013). Phospholipids in Milk Fat: Composition, Biological and Technological Significance, and Analytical Strategies. *International Journal of Molecular Sciences*, 2808-2831.

Costin, G., & Hearing, V. (2007). Human skin pigmentation: melanocytes modulate skin color in response to stress. *Federation of American Societies for Experimental Biology Journal*, 976-994.

Diffey, B. (2002). Sources and Measurement of Ultraviolet Radiation. *Methods*, 4-13.

Donaldson, M., & Coldiron, B. (2011). No End in Sight: The Skin Cancer Epidemic Continues. *Seminars in Cutaneous Medicine and Surgery*, 3-5.

Duff, C. W. (2011, June 6). *Basal Cell and Squamous Cell Skin Carcinomas.* Retrieved from Veterans Today: http://www.veteranstoday.com/?p=111453

Evers, J. (2004). The milkfat globule membrane-compositional and structural changes post secretion by the mammary secretory cell. *International Dairy Journal*, 661-674.

Fox, T., Houck, K., O'Neill, S., Nagarajan, M., Stover, T., Pomianowski, P., et al. (2007). Ceramide Recruits and Activates Protein Kinase C (zeta) within Strutured Membrane Microdomains. *Journal of Biological Chemistry*, 12450-12457.

Fransen, M., & et al. (2012, November 19). Non-melanoma skin cancer in Australia. *Medical Journal of Australia*, 565-568.

Fu, Q. (2003). Radiation (Solar). 1859-1863.

Gault, C., Obeid, L., & Hannun, Y. (2010). An Overview of Sphingolipid Metabolism: From Synthesis to Breakdown. In C. Chalfant (Ed.), *Sphingolipids as Signaling and Regulatory Molecules* (pp. 1-23). Springer.

George, K., & Wu, S. (2012). Lipid raft: A floating island of death or survival. *Toxicology and Applied Pharmacology*, 311-319.

George, K., Elyassaki, W., Wu, Q., & Wu, S. (2012). The Role of Cholesterol in Ultraviolet Light B-Induced Apoptosis. *Photochemical & Photobiological Sciences*, 1191-1197.

Giacomoni, P. U. (2007). *Biophysical and Physiological Effects of Solar Radiation on Human Skin.* Royal Society of Chemistry.

Gniadecki, R., Christoffersen, N., & Wulf, H. C. (2002). Cholesterol-Rich Plasma Membrane Domains (Lipid Rafts) in Keratinocytes: Importance in the Baseline and UVA-Induced Generation of Reactive Oxygen Species. *Journal of Investigative Dermatology*, 582-588.

Gulbis, J., Kelman, Z., Hurwitz, J., O'Donnell, M., & Kuriyan, J. (1996). Sturcture of the C-Terminal Region of p21 Complexed with Human PCNA. *Cell*, 297-306.

Haracska, L., Johnson, R., Unk, I., Phillips, B., Hurwitz, J., Parkash, L., et al. (2001). Physical and Functional Interactions of Human DNA Polymerase (eta) with PCNA. *Molecular and Cell Biology*, 7199-7206.

Hattinger, C., Jochemsen, A., Tanke, H., & Dirks, R. (2002). Induction of p21 mRNA Synthesis After Short-wavelength UV Light Visualized in Individual Cells by RNA FISH. *Journal of Histochemistry and Cytochemistry*, 81-89.

Hellgren, L. (2001). Occurrence of bioactive sphingolipids in meat and fish products. *European Journal of Lipid Science and Technology*, 661-667.

Holleran, W., Williams, M., Gao, W., & Elias, P. (1990). Serine-palmitoyl transferase activity in cultured human keratinocytes. *Journal of Lipid Research*, 1655-1661.

Inhibition of Skin Carcinomas but Not Papillomas by Sphingosine, N-Methylsphingosine, and N-Acetylsphingosine. (1998). *Nutrition and Cancer*, 119-126.

Jensen, P., & Bolund, L. (1991). Tissue culture of human epidermal keratinocytes: a differentiating model system for gene testing and somatic gene therapy. *Journal of Cell Science*, 255-259.

Jung, Y.-S., Qian, Y., & Chen, X. (2010). Examination of the expanding pathways for the regulation of p21 expression and activity. *Cellular Signalling*, 1003-1012.

Kanagasabai, R., Karthikeyan, K., Vedam, K., Qien, W., Zhu, Q., & Ilangovan, G. (2010). Hsp27 Protects Adenocarcinoma Cells from UV-Induced Apoptosis by Akt and p21-Dependent Pathways of Survival. *Molecular Cancer Research*.

Kudoh, T., Velkoff, M., & Wenger, D. (1983). Uptake and metabolism of radioactively labeled sphingomyelin in cultured skin fibroblasts from controls and patients with Niemann-Pick disease and other lysosomal storage diseases. *International Journal of Biochemistry and Biophysics*, 82-92.

Lasserre, R., Guo, X.-J., Conchonaud, F., Hamon, Y., Hawchar, O., Bernard, A.-M., et al. (2008). Raft nanadomains contribute to Akt/PKB plasma membrane recruitment and activation. *Nature Chemical Biololgy*, 538-547.

Lee, J. Y., Kim, H. S., Kim, J. Y., & Sohn, J. (2009). Nuclear translocatino of p21 protein prior to its cytosolic degradation by UV enhances DNA repair and survival. *Biochemical and Biophysical Research Communications*, 1361-1366.

Life Technologies. (2005). *Image-iT FX Signal Enhancer Datasheet.*

Life Technologies. (2013). *Useful Numbers for Cell Culture*.

Lodish, H., Berk, A., Kaiser, C. A., Kreiger, M., Bretcher, A., Ploegh, H., et al. (2013). *Molecular Cell Biology* (7th ed.). New York: W. H. Freeman and Company.

Lomas, A., & et al. (2012). A systematic review of worldwide incidence of nonmelanoma skin cancer. *British Journal of Dermatology*, 1069-1080.

Lopez-Contreras, A. J., & Fernandez-Capetillo, O. (2012). Signalling DNA Damage. In C. Huang (Ed.), *Protein Phosphorylation in Human Health.* Intech.

Machlin, S., Carper, K., & Kashihara, D. (2011, November). STATISTICAL BRIEF #345: Health Care Expenditures for Non-Melanoma Skin Cancer among Adults, 2005-2008 (Average Annual). *Medical Expenditure Panel Survey*. U.S. Department of Health and Human Services.

Mansilla, S., Soria, G., Vallerga, M. B., Habif, M., Martinez-Lopez, W., Prives, C., et al. (2013). UV-triggered p21 degradation facilities damaged-DNA replication and preserves genomic stability. *Nucleic Acids Research*.

Mascitelli, L., & et al. (2010). The epidemic of nonmelanoma skin cancer and the widespread use of statins. *Dermato-Endocrinology*, 37-38.

Maverakis, E., Miyamura, Y., Bowen, M., Correa, G., Ono, Y., & Goodarzi, H. (2010). Light, including ultraviolet. *Journal of Autoimmunity*, j247-j257.

Melnikova, V., & Ananthaswamy, H. (2005). Cellular and molecular events leading to the development of skin cancer. *Mutation Research*, 91-106.

Miller, D., & Weinstock, M. (1994, May). Nonmelanoma skin cancer in the United States: incidence. *Journal of the American Academy of Dermatology*, 774-778.

Modrak, D., Gold, D., & Goldenberg, D. (2006). Sphingolipid targets in cancer therapy. *Molecular Cancer Therapeutics*, 200-208.

Muira, S., Tanaka, M., Suzuki, A., & Sato, K. (2004). Application of phospholipids extracted from bovine milk to reconstitution of cream using butter oil. *Journal of the American Oil Chemists' Society*, 97-100.

Nagata, Y., Partridge, T., Matsuda, R., & Zammit, P. (2006). Entry of muscle satellite cells into the cell cycle requires sphingolipid signaling. *Journal of Cell Biology*, 245-253.

Nelson, D., Albert, L., & Cox, M. (2008). *Lehninger Principles of Biochemistry* (5th ed.). New York: W. H. Freeman.

Nestor, M., & et al. (2012). The Incidence of Nonmelanoma Skin Cancers and Actinic Keratoses in South Florida. *Journal of Clinical and Aesthetic Dermatology*, 20-24.

Nie, M., Balda, M., & Matter, K. (2011). Stress- and Rho-activated ZO-1–associated nucleic acid binding protein binding to p21 mRNA mediates stabilization, translation, and cell survival. *Proceedings of the National Academy of Sciences*.

Pilkington, S., Massey, K., Bennett, S., Al-Aasswad, N., Roshdy, K., Gibbs, N., et al. (2013). Randomized controlled trial of oral omega-3 PUFA in solar-simulated radiation-induced suppression of human cutaneous immune responses. *American Journal of Clinical Nutrition*, 646-652.

Pillai, S., Mahajan, M., & Carlomusto, M. (1999). Ceramide potentiates, but sphingomyelin inhibits, vitamin D-induced keratinocyte differentiation: comparison between keratinocytes and HL-60 cells. *Archive of Dermatology Research*, 284-289.

Price, R., Anthony, E., Myers, S., & Navsaria, H. (2008). Chapter 17: Tissue Engineering for Skin Transplantation. In C. van Blitterswijk (Ed.), *Tissue Engineering* (pp. 507-532). Elsevier.

Proksch, E., Brandner, J., & Jensen, J.-M. (2008). The skin: an indispensable barrier. *Experiemental Dermatology*, 1063-1072.

Pyne, N., Tonelli, F., Lim, K. G., Long, J., Edwards, J., & Pyne, S. (2012). Sphingosine 1-phosphate signalling in cancer. *Biochemical Society Transactions*, 94-100.

Raj, D., Brash, D., & Grossman, D. (2006). Keratinocyte Apoptosis in Epidermal Development and Disease. *Journal of Investigative Dermatology*, 243-257.

Ramos, J., Villa, J., Ruiz, A., Armstrong, R., & Matta, J. (2004). UV Dose Determines Key Characteristics of Nonmelanoma Skin Cancer. *Cancer Epidemiology, Biomarkers & Prevention*, 2006-2011.

Ravi, R., & Piva, T. J. (2013). The Role of Furin in the Development of Skin Cancer. In D. P. Vereecken (Ed.), *Highlights in Skin Cancer*. Intech.

Riboni, L., Prinetti, A., Bassi, R., & Tettamanti, G. (1994). Formation of bioactive sphingoid molecules from exogenous sphingomyelin in primary cultures of neurons and astrocytes. *Federation of European Biochemical Societies*, 323-326.

Rodgers, H., & et al. (2010, March). Incidence Estimate of Nonmelanoma Skin Cancer in the United States, 2006. *JAMA Dermatology, 146*, 283-287.

Rodriguez-Vilarrupla, A., Diaz, C., Canela, N., Rahn, H.-P., Bachs, O., & Agell, N. (2002). Identi¢cation of the nuclear localization signal of p21 and consequences of its mutation on cell proliferation. *Federation of European Biochemical Societies*, 319-323.

Rogan, J. (1977). Is the ANOVA F-Test Robust to Variance Heterogeneity When Sample Sizes are Equal?: An Investigation via a Coefficient of Variation. *American Educational Research Journal*, 493-498.

Rubin, H. (2003). Microenvironmental Regulation of the Initiated Cell. *Advances in Cancer Research*, 1-62.

Russell, A., Laubscher, A., Jimenez-Flores, R., & Laiho, L. (2010). Investigating the protective properties of milk phospholipids against ultraviolet light exposure in a skin equivalent model. *Proc. SPIE, 7569*.

Saladin, K. S. (2010). *Anatomy & Physiology: The unity of form and function* (5th ed.). McGraw-Hill.

Samarasinghe, V., & Madan, V. (2012). Nonmelanoma Skin Cancer. *Journal of Cutaneous and Aesthetic Surgery*, 3-10.

Sandilands, A., Sutherland, C., Irvine, A., & McLean, W. (2009). Filaggrin in the frontline: role in skin barrier function and disease. *Journal of Cell Science*, 1285-1294.

ScienCell Research Laboratories. (2009). *Human Epidermal Keratinocytes-fetal*.

Scott, M., Ingram, A., & Ball, K. (2002). PDK1-dependent activation of atypical PKC leads to degradation of the p21 tumour modifier protein. *European Molecular Biology Organization Journal*, 6771-6780.

Stacey, G. (2005). Primary Cell Cultures and Immortal Cell Lines. *Encyclopedia of Life Sciences*, 1-6.

Standring, S. (2009). *Gray's Anatomy, 40th Edition.* Churchill Livingstone.

Stover, E., Haas, C., Rakness, K., & Scheible, O. K. (1986). *Design Manual: Municipal Wastewater Disinfection.* U.S. Environmental Protection Agency.

Stulberg, D., Crandell, B., & Fawcett, R. (2004). Diagnosis and Treatment of Basal Cell and Squamous Cell Carcinomas. *American Family Physician*, 1481-1488.

Sturm, N. (2013). *Membranes*. Retrieved from http://www.nbs.csudh.edu/chemistry/faculty/nsturm/BSN335/17_Membranes.htm

Surdu, S., & et al. (2013, April). Occupational Exposure to Ultraviolet Radiation and Risk of Non-Melanoma Skin Cancer in a Multinational European Study. *PloS one, 8*(4).

Svobodova, A., Walterova, D., & Vostalova, J. (2006). Ultraviolet Light Induced Alteration to the Skin. *Biomed Pap Med Fac Univ Palacky Olomouc Czech Repub.*, 25-38.

Tanaka, T., Ogura, R., Hidaka, T., & Sugiyama, M. (1989). Changes of Electron Spin Resonance Membrane Fluidity in Hexadecanë-Induced Hyperproliferative Epidermis. *Journal of Investigative Dermatology*, 682-686.

Thermo Scientific. (2013). *Nunc Lab-Tek Chambered Coverglass*.

Tillhon, M., Cazzalini, O., Dutto, I., Stivala, L. A., & Prosperi, E. (2013). p21 and DNA Repair Systems: Recent Findings and Future Perspectives. In C. Chen (Ed.), *New Research Directions in DNA Repair.* Intech.

U.S. Food and Drug Administration. (2013, September 25). *Sunscreen*.

UVP LLC. (2013). *EL Series UV Lamps*. Retrieved from http://uvp.com/elseries.html

Vandenabeele, P., Galluzzi, L., Vanden Berghe, T., & Kroemer, G. (2010). Molecular Mechanisms of Necroptosis: an Ordered Cellular Explosion. *Nature Reviews*, 700-714.

Vesper, H., Schmelz, E.-M., Nikolova-Karakashian, M., Dillehay, D., Lynch, D., & Merrill, A. (1999). Sphingolipids in Food and the Emerging Importance of Sphingolipids to Nutrition. *Journal of Nutrition*, 1239-1250.

Vince, D. G., Tbakhi, A., Gaddipati, A., Cothren, R., Cornhill, J. F., & Tubbs, R. (1997). Quantitative comparison of immunohistochemical staining intensity in tissues fixed in formalin and Histochoice. *Analytic Cellular Pathology*, 119-129.

Warfel, N., & El-Deiry, W. (2013). p21 and tumorgenesis: 20 years after. *Current Opinion in Oncology*, 52-58.

Yuspa, S. H. (1994). The Pathogenesis of Squamous Cell Cancer: Lessons Learned from Studies of Skin Carcinogenesis. *Cancer Research*, 1178-1189.

Appendix A: PixelCount MATLAB Code

The following MATLAB codes were written by Bradley Schab and used in this thesis to calculate p21 expression ratios (number of nuclei with greater than 2% green pixels to total number of nuclei) for confocal images of normal human epidermal keratinocytes.

PixelCount Script

```
clear
close all
clc

% Image folder location
old=cd('Enter folder path here');
A=dir;
% Find all .tif image files
j=0;
for i=1:length(A)
    k=strfind(A(i).name,'.tif');
    if ~isempty(k)
        j=j+1;
        Out(j).name=A(i).name;
    end
end
% Open images
for j=1:length(Out)
    Out(j).I=imread(Out(j).name);
end
cd(old)
% Process images using the PixelCount function
minGreen=5;
for j=1:length(Out)
    j
    [Out(j).numBlue, Out(j).numGreen]=PixelCount(Out(j).I,minGreen);
    Out(j).Ratio=Out(j).numGreen/Out(j).numBlue;
end
% Write data to Excel spreadsheet
Temp{1,1}='Name';
Temp{1,2}='numBlue';
Temp{1,3}='numGreen';
Temp{1,4}='Ratio';
for j=1:length(Out)
    Temp{j+1,1}=Out(j).name;
    Temp{j+1,2}=Out(j).numBlue;
    Temp{j+1,3}=Out(j).numGreen;
    Temp{j+1,4}=Out(j).Ratio;
end
% Excel file location
xlswrite('Enter file path here',Temp)
```

PixelCount Function

```
function [cell_count area_count]=PixelCount(I,mingreenpix)

minPixel=200;

global I_green;
global blue;
global cc_blue;

% Split image into Green and Blue channels
I_green=I(:,:,2);
I_blue=I(:,:,3);

% Apply auto threshold to Green and Blue channels
thresh(2)=graythresh(I_green);
thresh(3)=graythresh(I_blue);

% Converts Blue image to B/W and finds and fills all connected areas of
% a minimum area
I_blue=imadjust(I_blue);
BW_blue=im2bw(I_blue,thresh(3));
BW_blue=bwareaopen(BW_blue,minPixel);
BW_blue=imfill(BW_blue,'holes');
cc_blue=bwconncomp(BW_blue,8);
blue.count=cc_blue.NumObjects;
blue.thresh=thresh(3);
blue.ImageSize=cc_blue.ImageSize;
blue.props=regionprops(cc_blue,'Area','Eccentricity','Perimeter');
blue.BW=BW_blue;

% Steps through all the blue areas and then converts all green within a
% blue area to B/W and finds the connected areas within that area
blue_area=zeros(1,blue.count);
green_count=zeros(1,blue.count);
Area=cell(blue.count);
for i=1:blue.count
    blue_area(i)=blue.props(i,1).Area;
    tempblue=false(blue.ImageSize);
    tempblue(cc_blue.PixelIdxList{i})=true;
    tempgreen=uint8(tempblue.*double(I_green));
    tempgreen=imadjust(tempgreen);

    BW_green=im2bw(tempgreen,0.05);
    BW_green=bwareaopen(BW_green,mingreenpix);
    BW_green=imfill(BW_green,'holes');

    cc_green=bwconncomp(BW_green,8);
    Area{i}=regionprops(cc_green,'Area');
    green_count(i)=cc_green.NumObjects;
end

for i=1:length(Area)
    green_area(i)=0;
    for j=1:length(Area{i})
        green_area(i)=green_area(i)+Area{i}(j).Area;
```

```
    end
end

% Computes global properties of the images
area_ratio=green_area./blue_area;
expression_count=length(find(green_count>1));
area_count=length(find(area_ratio>0.02));
cell_count=blue.count;
ratio=expression_count/cell_count;

end
```

Appendix B: IntenseCount MATLAB Code

The following MATLAB codes were written by Bradley Schab and used in this thesis to calculate mean nuclear p21 intensity values for confocal images of normal human epidermal keratinocytes.

IntenseCount Script

```
clear
close all
clc

% Image folder location
old=cd('Enter folder path here');
A=dir;
% Find all .tif image files
j=0;
for i=1:length(A)
    k=strfind(A(i).name,'.tif');
    if ~isempty(k)
        j=j+1;
        Out(j).name=A(i).name;
    end
end
% Open images
for j=1:length(Out)
    Out(j).I=imread(Out(j).name);
end
cd(old)
% Process images using the IntenseCount function
minGreen=0;
for j=1:length(Out)
    j
[Out(j).numBlue,Out(j).numGreen,Out(j).intenseGreen]=IntenseCount(Out(j
).I,mi nGreen);
    Out(j).Ratio=Out(j).numGreen/Out(j).numBlue;
end
% Write data to an Excel spreadsheet
Temp{1,1}='Name';
Temp{1,2}='numBlue';
Temp{1,3}='numGreen';
Temp{1,4}='Ratio';
Temp{1,5}='Intensity';
for j=1:length(Out)
    Temp{j+1,1}=Out(j).name;
    Temp{j+1,2}=Out(j).numBlue;
    Temp{j+1,3}=Out(j).numGreen;
    Temp{j+1,4}=Out(j).Ratio;
    Temp{j+1,5}=Out(j).intenseGreen;
end
% Excel file location
xlswrite('Enter file path here',Temp)
```

IntenseCount Function

```
function [numBlue,numGreen,intenseGreen]=IntenseCount(I,minGreen)

minPixel=200;
% Split image into Green and Blue channels
I_green=I(:,:,2);
I_blue=I(:,:,3);

% Apply auto threshold to Blue channel
thresh(3)=graythresh(I_blue);

% Compute connected blue pixels and fill holes
I_blue=imadjust(I_blue);
BW_blue=im2bw(I_blue,thresh(3));
BW_blue=bwareaopen(BW_blue,minPixel);
BW_blue=imfill(BW_blue,'holes');
cc_blue=bwconncomp(BW_blue,8);
numBlue=cc_blue.NumObjects;
blue.ImageSize=cc_blue.ImageSize;

% Trim green to each blue area and compute green intensity
green_count=zeros(1,numBlue);
parfor i=1:numBlue;
    tempblue=false(blue.ImageSize);
    tempblue(cc_blue.PixelIdxList{i})=true;

    tempgreen=uint8(tempblue.*double(I_green));
    if length(find(tempgreen~=0))>0
        greenintense(i)=mean(tempgreen(tempgreen~=0));
    else
        greenintense(i)=0;
    end
end
intenseGreen=mean(greenintense);
numGreen=length(find(greenintense>minGreen));
```